Delft University of Technology

Master Thesis

Identifying Windows of Opportunity for Mangrove Establishment on a Mud Coast

A case study for the BioManCo project in Demak, Indonesia

T.J.F. (Tim) van Domburg

September 26, 2018

TU Delft Delft University of Technology

Deltares Enabling Delta Life

Identifying Windows of Opportunity for Mangrove Establishment on a Mud Coast

A case study for the BioManCo project in Demak, Indonesia

by

T.J.F. (Tim) van Domburg

in partial fulfilment of the requirements for the degree of

Master of Science
in Civil Engineering

at the Delft University of Technology
to be defended publicly on Wednesday October 10, 2018 at 02:00 PM.
An electronic version of this thesis is available at `http://repository.tudelft.nl/`.

Student number:	4228529	
Project duration:	05-02-2018 until 10-10-2018	
Thesis committee:	Prof. dr. P.M.J. Herman,	TU Delft - Deltares
	Dr. Ir. B.C. van Prooijen,	TU Delft
	Dr. Ir. S. de Vries,	TU Delft
	Ir. A.G.M. Gijón Mancheño,	TU Delft
	Ir. B.P. Smits,	Deltares
	MSc. C.E.J. van Bijsterveldt,	NIOZ

Delft University of Technology
Faculty of Civil Engineering and Geosciences
Department of Hydraulic Engineering

TU Delft Delft University of Technology

Deltares Enabling Delta Life

Abstract

The coastline of Demak (Indonesia) has been retreating severely due to the large-scale removal of mangrove forests. In an attempt to restore the sediment balance and achieve mangrove re-establishment, permeable structures have been installed in front of the coast with promising, but inconsistent results in terms of mangrove recruitment. This research aims on improving the knowledge about the physical processes that limit mangrove colonisation at the coastal zone of Demak.

Two transects without permeable structures, one with mangrove recruitment and one with mangrove retreat, were analysed based on the Windows of Opportunity concept. A Window of Opportunity (WoO) is a sufficiently long disturbance-free period after seedling dispersal, that enables mangrove establishment. By means of a data analysis and one-dimensional XBeach modelling the transects were analysed for the physical disturbances from tidal inundation and wave forcing during the north-west monsoon period, in order to identify WoO.

Since the monthly averaged water level at the Demak coastal zone changes considerably throughout the year, WoO seem most likely to occur between February-April and August-September, when the average water level is relatively low. In order to resist disturbances from wave forcing, the importance of the local critical shear stress for sediment mobilisation ($\tau_{cr;ero}$) and the growth rate of the mangrove seedling strength (k) was emphasised. Based on the model results, the required value for k was estimated to lie between $5.3e^{-3}$ Pa/hour and $6.3e^{-3}$ Pa/hour. Additionally, the heterogeneity of grain sizes along the transects underscores the dependence of occurring WoO on local conditions, with higher possibilities for WoO at locations with higher $\tau_{cr;ero}$ values. Furthermore, model results showed that the presence of cheniers (i.e. bar-shaped sand deposits along the coast) is essential in order to achieve sufficiently small wave forcing along the transects to allow for WoO. The dynamic behaviour of cheniers indicates that the occurrence of WoO along the shoreline changes continuously.

Due to the importance of cheniers for achieving mangrove re-establishment, it is recommended to analyse the behaviour (i.e. development and propagation) of these mechanisms in more detail. Additionally, the high sensitivity of k on the occurring WoO points out that more insight into the growth properties of the pioneer mangrove species in the area is required in order to gain a better understanding about the hydrodynamic conditions that must be created in order to enhance mangrove colonisation at the coastal zone of Demak.

Preface

This thesis work concludes my Master of Science program 'Hydraulic Engineering' at the Delft University of Technology. The research is a part of the Building with Nature project *BioManCo* in Indonesia and was carried out at the TU Delft and Deltares.

I would like to express my gratitude to my thesis committee for their critical feedback and discussions during the research process. Special thanks goes out to my daily supervisors Alejandra and Bob from whom I frequently received helpful advice. The effort that you put in my research project is much appreciated. Additionally, thanks to the members of the *BioManCo* project team who provided me all the resources that were necessary to carry out this project. Also, thanks to Lodewijk de Vet for helping me out with the wave data analysis.

Furthermore, I am grateful that Deltares gave me the opportunity to work at a place that is flooded with hydraulic engineering expertise. I would also like to thank my fellow student Jeffrey Groot for motivating me to show up every morning at 9:00 AM sharp. Especially during the hot summer period.

Finally, thanks to my family, friends and girlfriend for the support during this final stage of my study.

Tim van Domburg
Delft, September 2018

Contents

1. Introduction

The topic of this research is introduced in this chapter. In Section 1.1, the erosion problems at the coastal zone of Demak are addressed and insight is given into rehabilitation strategies to restore the shoreline. Next, the problem statement of this research is described in Section 1.2 and the associated research questions are described in Section 1.3. Finally, the research approach is presented in Section 1.4.

1.1 Research introduction

Mangrove forests provide safety for a large number of tropical coastal areas around the world. These coastal ecosystems attenuate wave energy and reduce the impact of storm surges. Also, mangroves are able to increase bed elevation levels and therefore neutralise the effects of sea level rise over long periods (McIvor et al., 2013). Nevertheless, mangrove coasts have been retreating severely throughout the years, threatening the safety of millions of people. This research focuses on a vulnerable coastline in Demak, a province in the north of Central-Java, Indonesia.

The coastline of Demak used to be well protected by a wide stretch of mangrove forest. However, in the late 20^{th} century, large areas of mangrove forest were turned into aquaculture ponds which reduced both the room for the sea as the sediment supply from the hinterland to the mangrove areas. Consequently, the sediment balance at the coast got disturbed, resulting in coastal erosion due to which even more mangroves disappeared (Winterwerp et al., 2005; Winterwerp, 2014). Furthermore, subsidence due to groundwater extraction and sea level rise are causing a significant increase of the relative sea level which is an additional threat to the mangrove habitat and the coastal safety. The severe retreat of mangroves in the Demak province reaches from hundreds of meters to a few kilometres, as can be seen in Figure 1.1 (EcoShape, 2015).

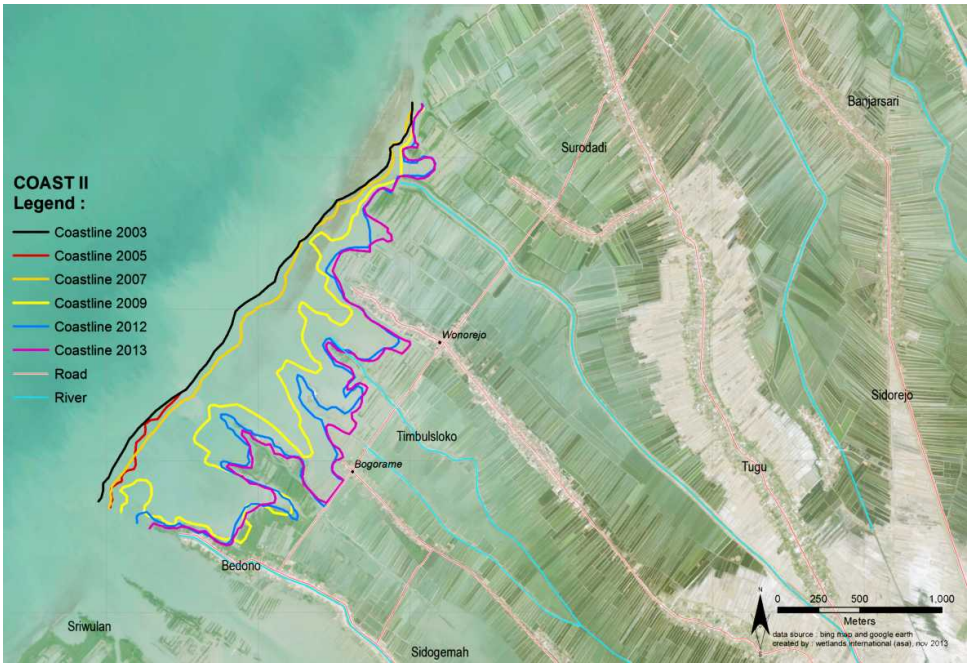

Figure 1.1: Shifting position of the Demak coastline from 2003 to 2013 (Smits, 2016)

Rehabilitation of the mangrove-mud coast should be achieved by restoring the fine sediment balance and creating a situation with net accretion (Winterwerp et al., 2005). This means that the amount of sediment that is deposited should exceed the amount that is washed away. According to Winterwerp et al. (2005), waves play an essential role in sedimentation and erosion phenomena that affect the fine

sediment balance. Wave action mobilises sediment that is then transported by the tide either in onshore or offshore direction. Since waves can influence the fine sediment balance both negatively, causing erosion, as well as positively, causing accretion, a sufficiently large offshore to nearshore gradient in wave energy should be achieved to enhance a net sediment supply.

In an attempt to restore the fine sediment balance, permeable structures have been installed in the intertidal area, based on a *Building with Nature* approach. The structures attenuate wave energy while letting through suspended sediments that deposit when entering the quiet zone behind the structures (Winterwerp et al., 2013). This way, the sediment budget is supplemented and the desired conditions for mangrove growth should be acquired. However, human intervention is not the only way to create a positive sediment balance. Along the Demak coastline, an accreting transect without permeable structures was selected. A chenier, i.e. a migrating lens of sand, is located in front of the coast and has an increasing effect on the offshore to nearshore gradient in wave energy and might be the reason that ideal conditions for mangrove establishment are created (EcoShape, 2015).

To investigate the threshold conditions for mangrove establishment further, it is important to understand the physical processes that limit pioneer mangrove colonisation. Balke et al. (2011) determined how seedling establishment is affected by a combination of increasing hydrodynamic forces and sediment dynamics, based on the Windows of Opportunity (WoO) concept. WoO are disturbance-free periods of a minimum critical duration that can induce a positive biogeomorphic feedback to allow for mangrove growth (Balke et al., 2014). Balke et al. (2011) defined a sequence of WoO, based on the root length of the mangrove seedlings. First, when seedlings are dispersed during a high water event, the stranded seedlings need a minimum inundation-free period to develop roots that are long enough to anchor in the soil and prevent them from floating. Next, the hydrodynamic forces from waves and currents should allow for a period of low bed shear stresses so that the seedlings can grow in strength without being dislodged. Finally, a substantial part of the roots needs to remain below the ground which means that a minimum disturbance from erosion around the seedlings is allowed. This sequence of thresholds must be passed in order to achieve mangrove establishment.

The focus of this research lies particularly on waves, as it can be stated that waves have an important influence on both the net sediment supply that is necessary for accretion as the Windows of Opportunity for mangrove establishment.

1.2 Problem statement

The permeable structures that have been installed in front of the coast of Demak have shown successful and promising results in terms of accreting coastlines. However, the results of this technique are not consistent for each rehabilitation project. This indicates that there is not enough knowledge about the exact hydrodynamic conditions that must be created in order to develop a healthy mangrove forest. More specifically, the Windows of Opportunity for mangrove establishment have not been identified in detail.

1.3 Objectives

This research aims on identifying Windows of Opportunity for mangrove establishment. It is desired to analyse the temporal variability of wave forcings on the intertidal flat in order to gain a better understanding about the threshold dynamics for mangrove growth.

An eroding and an accreting transect of a mangrove-mud coast without permeable structures are studied in order to relate their behaviour to the Windows of Opportunity concept.

The following research question has been formulated:

Can Windows of Opportunity for mangrove establishment be identified, looking at the effect of waves?

The research question is approached by answering the following sub-questions:

- How do waves transform along the transects?
  - What are the dominant energy dissipation mechanisms?
- What are the wave-induced bed shear stresses along both transects?
- How does the bed level change in the transects and how is this associated with the bed shear stresses that are present?
  - What are the critical shear stresses for bed erosion along the transects?
- How do both transects differ and what is the main cause of this difference?

1.4 Approach

The research starts with a literature study to learn about hydrodynamic coastal processes and sediment dynamics that are relevant in order to understand the morphodynamics of mangrove-mud coasts. Furthermore, favourable conditions for mangrove establishment are studied in terms of sediment dynamics and Windows of Opportunity. Additionally, a system analysis of the Demak coastal zone is carried out in order to gain a better understanding about the coastal system in the study area.

Next, a data analysis is carried out in order to gain insight into the dominant energy dissipation mechanisms that drive the wave transformation along the transects. Furthermore, the bed level changes at several locations along the transects are analysed and the coherence with the locally occurring hydrodynamics is assessed.

Then, the observed wave transformation along both transects is reproduced by means of the numerical model XBeach, one model for each transect, in order to calculate bed shear stresses. The models are validated by means of the data analysis. Several scenarios are implemented in the model set-up in order to identify Windows of Opportunity for various situations and qualitatively study the influence of a chenier and vegetation on the possibilities for WoO within the transects.

Subsequently, the results from the data analysis and modelling work are extensively discussed. Finally, the conclusions are presented and recommendations for further research are proposed. The complete research approach is summarised in Table 1.1 by means of six separate stages.

Table 1.1: Research stages

Stage	Description
1	Literature study & system analysis
2	Assess wave transformation and bed level changes with a data analysis
3	Set-up and validation of the XBeach model
4	Simulating model scenarios
5	Discussion on data analysis and modelling results
6	Conclusions and recommendations

2. Theoretical background

This chapter elaborates on the most important physical processes that determine erosion and accretion of mangrove-mud coasts, along with descriptions of restoration efforts and threshold conditions for mangrove establishment. First, the relevant hydrodynamic processes that are important for this research are described in Section 2.1. Section 2.2.1 describes fine sediment properties and erosion and sedimentation processes. The morphological processes on mangrove-mud coasts in specific are described in Section 2.3.1. In Section 2.4 the focus lies on mangrove restoration in terms of the fine sediment balance and Windows of Opportunity.

2.1 Hydrodynamic coastal processes

The tide and waves influence the behaviour of the coastal profile and are thus important in order to understand the physical processes that occur in the area of consideration. Background information about the basic principles of tides and waves can be found in Appendix G. This section focuses on relevant topics for this research, which are wave energy dissipation and wave-induced bed shear stresses. Most information in this section refers to the Coastal Dynamics lecture notes by Bosboom and Stive (2015).

2.1.1 Wave energy dissipation

Waves play an essential role in the coastal morphological development. As waves propagate towards the shore, they are transformed due to interactions with the seabed, induced by friction which starts to affect the wave when the water depth becomes less then half the wave length.

Friction does not only affect the physical appearance of waves, it also affects the energy balance. Neglecting the influence of currents, the energy balance represents the balance between the generation and dissipation of wave energy.

The dissipation of the total wave energy is represented by Equation 2.1.

$$D_f = -\frac{dP}{dx} = -\frac{d(c_g \cdot E)}{dx} \tag{2.1a}$$

$$E = \frac{1}{8}\rho g H_{rms}^2 \tag{2.1b}$$

The wave energy (E) propagates with the wave group velocity (c_g) and causes an energy flux (P) into the propagation direction (x) which is defined by the wave energy multiplied by the wave group velocity. Under the assumption of the energy conservation law, the wave conditions that are observed offshore can be translated in terms of nearshore wave conditions by means of the energy balance.

As can be seen in Equation 2.1, the wave height dominantly determines the amount of wave energy. Therefore, the most important energy dissipation mechanism is wave breaking. Especially over large areas with shallow water, such as tidal flats, bottom friction can be important as well. The effect of vegetation on wave energy dissipation is extensively described in Section 2.3.2 and will not be elaborated on here.

Wave breaking occurs when the horizontal particle velocity inside the wave crest exceeds the propagation velocity of the wave. When this happens, the wave becomes unstable and bends over after which it breaks. Wave breaking can be divided into steepness- and depth- induced breaking. Since this research focuses mainly on shallow water, only depth-induced breaking is considered.

Depth-induced breaking is described by the breaker index, γ, which presents the relation between the wave height and water depth. On very mild slopes, such as intertidal mud flats, the breaker index lies between $\gamma = 0.6 - 0.8$. On these mild slopes, waves gradually break, looking like a bore, over a distance of approximately 6-7 wavelengths, causing an enhanced bed shear stress along this stretch. This breaking

process starts at a relatively large distance from the shore (Bosboom and Stive, 2015). A more detailed description of wave breaking is given in Appendix G.2.1.

The effect of bottom friction on wave energy dissipation can be described by means of the wave friction coefficient, f_w. The calculation of f_w is presented by Equation 2.2 and the method of calculating the effect of f_w on the wave energy dissipation is described in Appendix G.2.2. In this research, the wave friction coefficient will be used to calculate the observed energy dissipation along a mud flat in terms of bottom friction only. According to Lacy and MacVean (2016) the value of f_w for mud flats lies between 0.02-0.1.

$$f_w = \exp\left[-5.977 + 5.213\left(\frac{\hat{\zeta_0}}{r}\right)^{-0.194}\right] \tag{2.2a}$$

$$\hat{\zeta_0} = \frac{\hat{u_0}}{\omega} \tag{2.2b}$$

$$\hat{u_0} = \frac{\omega a}{\sinh(kh)} \tag{2.2c}$$

In Equation 2.2, f_w is the wave friction coefficient, r is the bed roughness, $\hat{\zeta_0}$ is the particle excursion close to the bed and $\hat{u}_0$ is the orbital velocity amplitude (Jonsson, 1966).

2.1.2 Boundary layer and bed shear stresses

In the previous section, wave transformation and energy dissipation are expressed in terms of water surface elevation. In this section, the particle motion underneath the wave surface is elaborated on further.

The orbital particle movements are the result of oscillatory horizontal and vertical flow velocities induced by waves. In deep water the particles follow a circular path whereas in shallow water, the shape of the orbital motion under a propagating wave is elliptical. From the water surface down to the bottom, the size of the horizontal movements remains more or less equal whereas the vertical movements reduce to zero (see Figure 2.1).

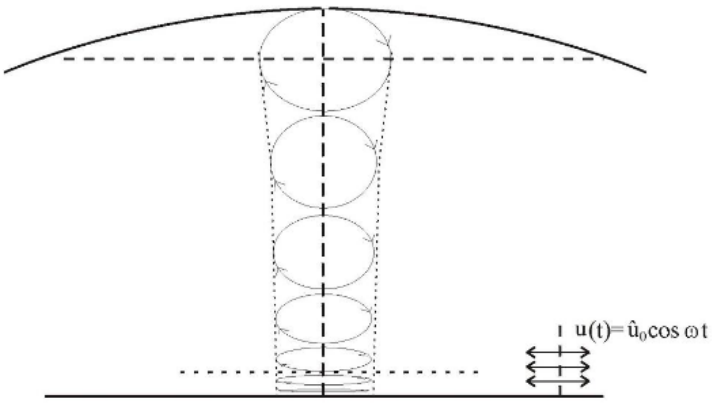

Figure 2.1: Orbital motions in intermediate to shallow water depth (Bosboom and Stive, 2015)

Close to the bed, wave action causes the formation of a thin boundary layer which is the transition zone between the bed and the undisturbed free-stream velocity of the wave particles. The bed roughness causes turbulent flow inside the boundary layer. Basically, the boundary layer is the flow area that is affected by the bed. With uniform flow, the flow has fully adapted to the frictional effects of the bottom and the boundary layer has now developed over the full depth. However, uniform flow only occurs in ideal situations which do not exist. Because of the continuously reversing wave-induced flow, the boundary

layer has little time to develop and remains thin. This causes that the perpendicular velocity gradients inside the boundary layer are relatively large, inducing large stresses. Consequently, energy is dissipated and sediments can be mobilised. These stresses are referred to as *bed shear stresses*. Since the thickness of the boundary layer is time-dependent, the wave period influences the magnitude of shear stresses that a wave can exert on the bed. Therefore, short waves a more capable of mobilising sediment than long waves.

For linear waves, the orbital free stream velocity can be defined by $u = \hat{u}_0 cos\omega t$. The maximum bed shear stress then follows from Equation 2.3.

$$\hat{\tau}_w = 0.5\rho f_w \hat{u}_0^2 \tag{2.3}$$

Furthermore, outside the breaker zone, a non-zero wave-averaged horizontal flow, streaming, was found inside the boundary layer (Longuet-Higgins, 1953). This streaming is potentially relevant for onshore sediment transport and therefore important to notice.

2.2 Sediment dynamics

From hydrodynamics to morphology. Mangrove coasts are characterised by a coastline consisting of (very) fine sediments. In order to understand the morphodynamic behaviour of mangrove-mud coasts, described in Section 2.3, this section elaborates on the basics of fine sediment dynamics. First, the properties of fine sediment are described after which processes of settling, consolidation and erosion are discussed. The content of this section is mainly based on Winterwerp (2011) and Winterwerp and Kesteren (2004).

2.2.1 Fine sediment properties

The reason of highlighting the word *fine* comes from the fact that the behaviour of fine sediment differs from coarse sediment which is the more regular sort of sediment that is often dealt with. The different behaviour is mainly based on the cohesive character of fine sediment which causes that the considered *cohesive sediment* consists of a mixture of fine sediment (clay and silt), organic material, water, and occasionally gas. Mud, as cohesive sediment is also called, is characterised by sediment sizes below 63 μm. In general, sediment can be transported in different modes. Distinction is made between sediment that interacts with the bed and sediment that does not interact with the bed. The latter is referred to as 'washload', indicating that the sediment remains in the water column, and is kept out of consideration here. Bed material, sediment that interacts with the bed, is transported either as bed load or as suspended load. Bed load moves near the bed while suspended load moves higher in the water column. Suspended load is kept in suspension due to turbulent mixing.

The cohesive character largely influences the behaviour of fine sediment in the water column. Most interest goes out to the erosion and settling properties of the particles since this is of main importance for the morphological behaviour of mangrove-mud coasts.

Within the water column, suspended fine sediment particles collide due to turbulent motions. These collisions cause aggregation due to which flocs are formed by means of Van der Waals forces. The size of the flocs mainly depends on the amount of turbulent energy and the sediment concentration. A higher concentration means more particles in the water column and consequently more collisions. On the other hand, if the turbulent induced forces get too high, the flocs break up again which decreases the floc size, which can be seen in Figure 2.2. The process of aggregation and break-up is called flocculation and is essential to understand in order to analyse the settling behaviour of fine particles.

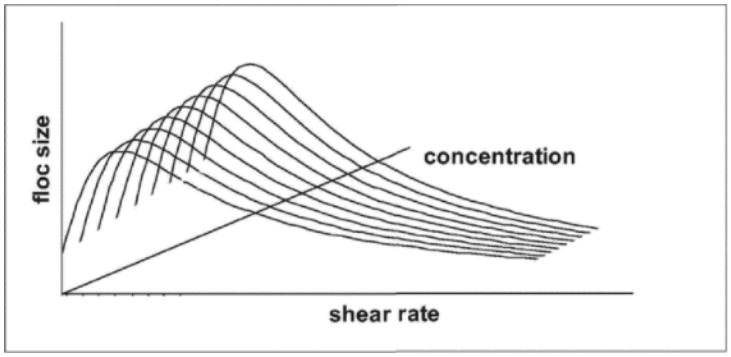

Figure 2.2: Flocculation diagram. Influence of concentration and turbulence shear on floc size (Winterwerp and Kesteren, 2004)

Additionally, mud flocs tend to have very open structures due to a large water content which is typically between 80-95%. This indicates that mud has a low bearing capacity. Furthermore, the permeability of mud mixtures is low due to the small particle sizes. The combination of a large water content with low permeability can result in liquefaction. This happens when the pressure inside the soil increases because the water cannot escape from the pores. As a result the soil looses its strength and starts to behave like a liquid. These properties cause that 'hard' coastal protection interventions such as breakwaters are not feasible to implement in muddy coastal systems.

2.2.2 Settling and consolidation

As mentioned in Section 2.2.1, suspended sediment interacts with the bed. This interaction is described by the turbulent mixing which brings sediment in suspension and the settling of the fine sediment particles which results in deposition. Due to flocculation, the settling velocities of mud flocs are higher than that of individual mud particles. The single particle velocity of mud is 0.001 to 1 mm/s while the observed floc velocity lies between 0.1 and 10 mm/s.

The settling velocity of spherical, Euclidean particles can be described by Stokes' law (see Equation 2.4). This law implies that the settling velocity is a result of an equilibrium between hydraulic drag forces and gravity and largely depends on the grain size diameter.

$$W_s = \frac{(\rho_s - \rho_w) g D^2}{18\mu} \tag{2.4}$$

Since flocs have open structures and are thus not massive like granular materials, Stokes' law does not hold. During the settling process, floc sizes grow due to aggregation which indicates higher settling velocities. With increasing sediment concentrations towards the bed, the falling flocs start to hinder each other and the settling velocity decreases. This is called *hindered settling*. The settling process of flocs is thus characterised by an initial increase of the settling velocity due to enhanced flocculation after which the velocity decreases as a result of hindered settling. Consequently, the settling velocity of mud flocs varies in time.

When fast deposition occurs, the concentration of suspended sediment near the bed becomes so high that a space-filling network is formed. The concentration at which this happens is called the *gelling concentration*. The sediment structure is now a mixture of water and mud and is referred to as *fluid mud*. Fluid mud is in a dynamic state, which means that it is not yet stable (see Section 2.2.4 for more fluid mud characteristics). Assuming that no external energy is supplied due to waves or currents, the consolidation process starts as the stresses inside the structure start to build up as a result of the weight of the flocs (see Figure 2.3). The stress inside the bed is referred to as the effective stress which is the difference between the total stress and the pore water pressure. As the vertical stresses increase, the water is squeezed out from the pores so that the size of the flocs shrink and vertical deformations occur. Inside the soil, the effective stress increases which strengthens the soil.

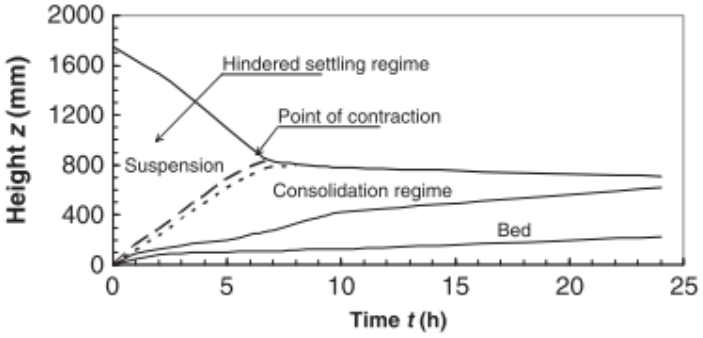

Figure 2.3: Schematisation of the settling process of flocs. The gelling concentration is reached at the contraction point. (Winterwerp, 2011)

2.2.3 Bed properties and erosion

The interaction processes between water and bed are well explained by a combination of the erosion formula of Partheniades and the deposition formula of Krone, presented by Equations 2.5 and 2.6, respectively (Partheniades, 1965; Krone, 1962).

$$E = M\frac{\tau_b - \tau_e}{\tau_e} \tag{2.5}$$

$$-D = -W_s c_b \left(1 - \frac{\tau_b}{\tau_d}\right) \tag{2.6}$$

The erosion rate is simply described by a threshold for incipient motion whereas the deposition rate is determined by the suspended sediment concentration (c_b) and the settling velocity (W_s). When there is a limited amount of fines available, for instance due to consolidation processes, these zero-order formulas are not desired. When consolidation plays a part, the amount of erodible fines must be taken into account because the sediment compaction strongly changes over the vertical. Distinction is therefore made between an upper and a lower layer of the soil. The upper layer actively responds to the flow-induced bed shear stresses whereas the responses of the lower body require larger bed shear stresses. This is further explained hereafter.

Whether a sediment deposition can be characterised as a liquid or as a soil depends on the Atterberg limits which distinguish between plastic and liquid limits. To be a soil, the water-sediment mixture must have a water content such that it reaches beyond the plastic limit. The Atterberg limits relate to the undrained shear strength of the material. Whether the response of a soil is drained or undrained depends on the flow of pore water. When deformations occur, pore water pressure gradients are induced. With a high enough permeability, the flow through the pores can compensate these pressures. Because of a low permeability, cohesive sediment shows an undrained behaviour and the soil strength is thus related to the water content. This supports the fact that consolidation strengthens the soil and decreases the erodibility (see Section 2.2.2).

When the mud-mixture behaves like a liquid (fluid mud), entrainment can occur. This is the re-suspension of sediment particles through turbulent mixing with the water body above. In the case of more plastic soil behaviour, Mehta et al. (1989) defined three other modes of erosion: floc erosion, surface erosion and mass erosion.

Floc erosion refers to the erosion of individual flocs from the bed. This occurs when the flow induced bed shear stresses exceed the strength of the unconsolidated flocs. When the flow velocity increases further, the bed shear stresses may induce liquefaction on the top of the bed. Surface erosion now occurs which affects the state of consolidation of the soil. This is a drained failure process since water replaces the place of sediment particles in the soil. In the case of mass erosion, highly consolidated mud deposits from the lower layer are removed from the soil. This type of erosion can be induced by the large stresses that are generated by waves.

The effect of waves on the erosion of cohesive sediment is thus considerably large. As mentioned earlier, the boundary layer has little time to develop due to which the bed shear stresses that are generated by orbital motions often exceed the flow-induced bed shear stresses from (tidal) currents. Furthermore, waves induce normal stresses inside the soil which can cause liquefaction which destabilises the soil.

The critical shear stress that is required for incipient motion depends on the sediment properties. The cohesiveness of a soil is therefore essential in order to determine the critical bed shear stress. For pure mud, consisting of grain sizes smaller than 32 μm, Van Rijn (1993) found critical bed shear stress values for surface erosion varying between 0.05-0.4 N/m^2. In the coastal area of Demak, mixing of sand and mud regularly occurs which affects the sediment properties. A laboratory experiment of BioManCo et al. (2018) showed that mud in this area has a dry bulk density of 585 kg/m^3 which can be characterised as light sandy mud with a critical bed shear stress for erosion varying between 0.15-0.25 N/m^2 (Mitchener and Torfs, 1996). A sand sample from the same area has a dry bulk density of 1080 kg/m^3, which results in a critical bed shear stress between 0.4-1.5 N/m^2. These values will be used in this research as a reference. The Demak area is further explored in Chapter 3.1.

2.2.4 Fluid mud characteristics

In Sections 2.2.2 and 2.2.3, the formation of fluid mud was discussed. Fluid mud is a mixture of water and sediments and thus behaves different than rigid soils. In a muddy coastal system as Demak, it is important to take the possibility of the presence of fluid mud into consideration. This section elaborates on characteristics of fluid mud, regarding wave dissipation, drag forces and shear stresses, that can be important to take into account during this research.

In Section 2.1, it was described how irregularities on the bed exert a friction on hydrodynamics due to which wave energy dissipation occurs. This is, assuming a *rigid* seafloor. In case of a *non-rigid* seafloor such as fluid mud, the pressure variations of the waves can initiate motions in the bed and generate a mudwave. To initiate these motions, work is done which requires an amount of energy, so wave energy is dissipated (Rogers and Holland, 2009). The amount of energy that is being dissipated depends on sediment properties, mud-layer thickness, wave period and local water depth. Elgar and Raubenheimer (2008) found that the maximum dissipation rate mainly occurs for the lowest frequencies.

Furthermore, Winterwerp and Kesteren (2004) elaborated on several studies regarding the effect of fluid mud on the hydrodynamic drag. Various Chézy values on coastal shelfs with fluid mud appearances have been found which vary between C $\approx$ 90 m$^{1/2}$/s and C $\approx$ 160 m$^{1/2}$/s. This range of values can be used as a reference for bed friction coefficients in a numerical model.

2.3 Morphodynamics of mangrove-mud coasts

Mangroves are trees that live in the intertidal coastal zone at tropical and subtropical latitudes. The intertidal zone is an area which is flooded during high tide and exposed to the atmosphere during low tide. The root system of a mangrove is developed in such a way that the aerial roots absorb enough oxygen from the air during low tide to be able to live under anaerobic circumstances. Muddy coastal systems are normally characterised by a slope around 1:1000 - 1:1500, at which mangroves are found to start colonising around Mean Sea Level (MSL) (Watson, 1928). At recruiting forests, the first zone consists of a mudflat with seedlings, then young trees with small pneumatophores, i.e. roots of pioneer mangrove species, and after that the mature mangrove forest with full grown pneumatophores. Retreating forests are characterised by a sudden transition between the mud flat and mature mangroves. In general, these areas do not contain mangrove seedlings.

Mangrove forests offer protection as they stabilise the coastline, reducing erosion from (tidal) currents, waves, and storm surges. Furthermore, mangroves represent an important ecosystem regarding climate change because of their high values of carbon storage and ability of adapting to sea level rise (McIvor et al., 2013). This section elaborates on how the interactions between hydrodynamics with both sediment and vegetation control the morphological development of the mangrove-mud coast.

2.3.1 Morphology

In Sections 2.2.2 and 2.2.3 it is described how fine sediment settles and how it is mobilised, respectively. In order to achieve a net accretion on a mangrove-mud coast, it is important to understand how the mobilised fine sediment is transported along the intertidal flat before it settles down. Most interest here goes out to the input of sediment on the intertidal flat. This section gives insight into physical processes that affect the sediment transport and therefore the physical appearance of mangrove-mud coasts. The presented information is largely based upon Winterwerp and Kesteren (2004) and Bosboom and Stive (2015).

In Section 2.1, it was explained that waves have a large influence on the mobilisation of sediment. Since waves transform when they approach the shore, the effect on sediment mobilisation and transport changes as well. Distinction is made between non-breaking and breaking waves.

Waves stir up sediment by exerting a shear stress on the bed resulting in erosion or re-suspension of the sediment particles. As mentioned in Section 2.2.3, suspension occurs through turbulent mixing with the water body. Under non-breaking waves, the turbulent boundary layer is very thin indicating that turbulent mixing hardly occurs. Therefore, the sediment is not mixed over the water column. More energy is required to bring the sediment into suspension. This energy becomes available when waves break. When waves break, vertical mixing is enhanced so that the sediment particles are brought in suspension. After mobilisation, the sediment is transported by means of wave- and flow-induced currents. Under non-breaking waves, Longuet-Higgins streaming causes onshore sediment transport. However, Longuet-Higgins streaming is an order of magnitude smaller than tidal currents, so that sediment transport is dominated by tidal flow. The dominant direction of sediment transport is influenced by tidal asymmetry, which determines if either ebb-currents or flood-currents are strongest. A larger peak velocity of the tidal current results in larger shear stresses and thus larger sediment concentrations that can be transported. Furthermore, the slack duration is especially important for fine sediment since fine sediment reacts slower on variations in local velocity than coarse sediment. When the slack duration is relatively high, more fine sediments can settle and will not be transported with the ebb current that follows. A flood-dominant tidal signal is therefore favourable in terms of net sediment transport towards the tidal flat.

The gross effects of sedimentation and erosion determine the state of the sediment balance and are thus important for the morphology of the coast. Due to the continuously changing hydrodynamic conditions combined with the fine sediment properties, mangrove-mud coasts are highly dynamic, accreting and retreating cyclically (Winterwerp et al., 2013).

Whether the coast has an accreting or an eroding character can be deduced from the cross-sectional profile, since waves are the dominant process behind coastal erosion. Figure 2.4 shows the difference between accreting and eroding mangrove-mud coasts. Equilibrium and accreting mangrove mud coasts have a *convex-up* shape whereas erosive coasts have a *concave-up* shape. This difference is also clearly visible in the profiles of the eroding and the accreting transect that are investigated in this research (see

Figure 5.2). When the profile of a mangrove-mud coast starts to become concave-up, wave action will start to dominate sedimentation processes which will erode the coast even further. A positive feedback can be induced causing severe retreat of the coastline (Winterwerp et al., 2013; Friedrichs, 2011). A concave profile is thus undesired.

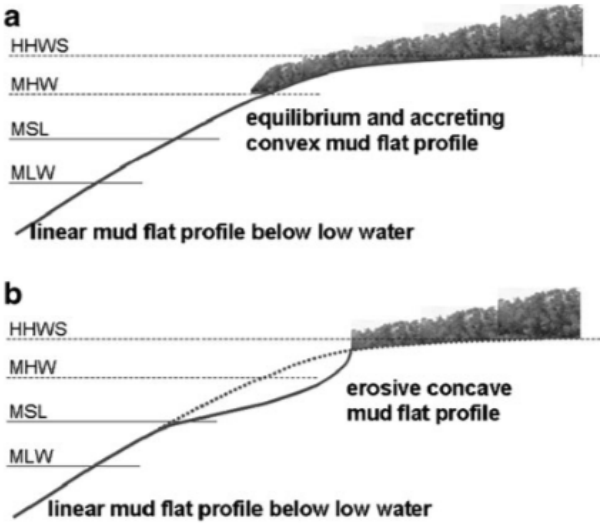

Figure 2.4: Diagram summarising properties of tidal flat profiles (Winterwerp et al., 2013)

2.3.2 Interaction between mangroves and hydrodynamics

Since mangroves grow on the intertidal area, the interaction between mangroves and local hydrodynamics is of high importance. Mullarney et al. (2017) states that the protective ability of mangroves can be owed to the drag on hydrodynamic forces that is enhanced by the presence of pneumatophores and tree trunks. Since wave transformation along a mangrove-mud coast is a main topic of this research, this section elaborates on the influence of mangroves on wave energy dissipation.

The conservation of wave energy in a mangrove forest is described by Equation 2.7.

$$\frac{\partial E c_g}{\partial x} = -\epsilon_v \tag{2.7}$$

The wave energy (E) and group velocity (c_g) are balanced by the energy dissipation induced by vegetation (ϵ_v).

Figure 2.5 presents the important properties of a mangrove coastline that influence the amount of wave energy dissipation and were summarised by McIvor et al. (2012). The forms of wave dissipation will be explained hereafter.

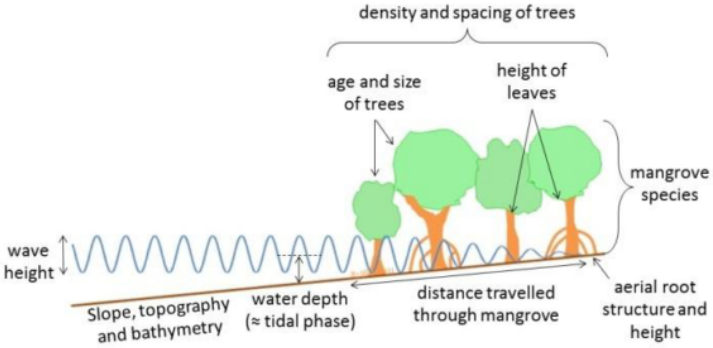

Figure 2.5: Characteristics of mangroves that affect the reduction of the incoming wave height (McIvor et al., 2012)

The wave force that is exerted on the surface of cylindrical objects was investigated by Morison et al. (1950) who discussed that the total force is a summation of drag- and inertia forces:

$$F = F_D + F_I = \frac{1}{2}\rho C_D d h_v U_w |U_w| + \frac{1}{4}\rho C_M \pi h_v d^2 \frac{\delta U_w}{\delta t} \tag{2.8}$$

where d is the diameter of the cylinder, h_v is the length of the submerged (vegetation) stem, U_w is the characteristic oscillatory flow velocity, C_D is the drag coefficient and C_M is the inertia coefficient.

A drag force is a resistance force caused by the motion of a body through a fluid. In the case of vegetation, the hydrodynamics induce the relative motion of the vegetation body through the fluid and the drag force is thus determined by the work done by the hydrodynamic energy (Suzuki et al., 2012). The surface perpendicular to the direction of motion is thus an important parameter to determine the drag force. With equal flow velocities, a larger surface indicates a larger drag force.

Since the drag force includes the diameter and height, and thus the density of the vegetation, it is assumed that the drag force represents the physical processes within the vegetation best. With little vegetation, for instance on the lower mudflat, the wave energy dissipation is relatively small and is only caused by bottom friction, whereas the dissipation is significantly higher inside the mangrove vegetation (Mazda et al., 1997; Horstman et al., 2014).

Apart from drag forces, oscillatory flow also induces inertial forces, as presented in Equation 2.8 by Morison et al. (1950). This is a result of the constantly changing flow direction along the stems of the vegetation. These changes in flow direction initiate local accelerations in the flow velocity and thus exert inertial forces on the stem surface. Despite the effect of inertial forces on wave dissipation, Horstman et al. (2014) states that friction and drag forces are the most dominant dissipation factors in mangrove vegetation.

Mendez and Losada (2004) introduced a measure for the wave propagation along an aquatic vegetation field consisting of seaweed. With the Keulegan-Carpenter number, $K = u_c T_p / b_v$, the drag coefficient can be related to wave parameters. The parameter u_c is the characteristic velocity that acts on the vegetation and is defined with H_{rms} and T_p. The plant area per unit height is given by b_v. Mendez and Losada (2004) found that the relation between K and C_D also depends on the relative height of the plants, α, so that the relation between C_D and K can be presented like Equation 2.9.

$$\tilde{C}_D = \frac{\exp(-0.0138Q)}{Q^{0.3}} \quad 7 \leq Q \leq 172 \tag{2.9}$$

in which $Q = K/\alpha^{0.76}$.

With this formulation for C_D, Mendez and Losada (2004) determined the dissipation due to vegetation with Equation 2.10.

$$\epsilon_v = \frac{1}{2\sqrt{\pi}}\rho\tilde{C}_D b_v N \left(\frac{kg}{2\omega}\right)^3 \cdot \frac{\sinh^3 k\alpha h + 3\sinh k\alpha h}{3k\cosh^3 kh} \cdot H_{rms}^3 \tag{2.10}$$

in which k is the wave number and N is the number of vegetation units per unit horizontal area. Equation 2.10 is implemented in the numerical model XBeach, which is used for this research. Note that since mangroves consist of various vertical sections with different properties (root system, stem and canopy), the effect of these parts needs to be configured separately.

The correlation between wave attenuation and vegetation properties has thus been studied extensively. Mullarney et al. (2017) studied the variation of drag forces along different environments within the mangrove-mud coast. Distinction was made between the non-vegetated mudflat, the mangrove fringe and the mangrove forest. In the fringe, densely populated with pneumatophores, drag forces were larger than in the sparsely populated mangrove forest. This supports the findings of Mazda et al. (1997) that showed that sparse vegetation acquired much smaller attenuation values than dense vegetation. This indicates that the vegetation density is an important factor for the amount of exerted drag forces. That can be explained by the fact that vegetation in the front provides sheltering for the vegetation in the back due to wake generation. Inside this wake the turbulence intensity increases, but since the wake is generated on a small stem scale, the turbulent length scale reduces, causing sheltering of the stems behind (Nepf, 1999). In her study, Nepf (1999) found that the drag coefficient reduces for increasing vegetation densities because of smaller values for the mean flow velocity.

Horstman et al. (2014) also studied the relation between wave attenuation and vegetation densities and found that, due to their quadratic relation, wave energy decreased more than the wave height in the vegetation, even though wave breaking did not occur. With larger wave heights, the relative amount of dissipated wave energy even increased compared to the total wave energy. Furthermore, since short waves are more sensitive to energy dissipation than swell waves, an increase of the mean wave period towards the shore was observed which might affect nearshore bed shear stresses.

The large effect of vegetation on wave attenuation makes mangrove-mud coasts vulnerable for feedback mechanisms as was stated by Winterwerp et al. (2013). When mangroves disappear, waves are less attenuated and erosion rates are likely to increase.

2.4 Mangrove restoration

This section elaborates on restoring the coastal zone of Demak (Indonesia) in terms of sediment dynamics and ecology. In Section 2.4.1 the focus lies on restoring the fine sediment balance and in Section 2.4.2 the threshold conditions for mangrove establishment are described.

2.4.1 Restoring the fine sediment balance

The location of the coastline is determined by the sediment balance and can be formulated with Equation 2.11 (Winterwerp et al., 2005). Degrading mangrove-mud coasts have a negative sediment balance, indicating that the erosion rates exceed that sedimentation rates.

$$\frac{dcl}{dt} = \text{sedimentation rate - erosion rate} \tag{2.11}$$

in which dcl/dt represents the coastline development.

When it comes to the rehabilitation of mangrove coasts, the fine sediment balance should be restored (Winterwerp et al., 2013). Looking at Equation 2.11, the sediment balance can be restored either by reducing erosion rates or enhancing sedimentation rates. Preferably, both. In any case, the incoming sediment should exceed the amount of sediment that is flushing away.

In Section 2.3.1, the influence of waves on sediment transport was described in detail. Since the sediment at muddy coasts is easy erodible, it is important to note that the presence of only small waves enhances erosion, whereas large waves both erode and supply sediment (Winterwerp et al., 2005). Therefore, in order to enhance shoreline accretion, a sufficiently large gradient in wave energy must be created that allows large waves to mobilise sediment for onshore transportation while only small waves reach the

shoreline to minimise coastal erosion. Simultaneously, onshore sediment transport should not be blocked by, for instance, hard structures.

The large effects of waves on the stability of mangrove-mud coasts can be supported by the presence of cheniers, i.e. a lens of sand that migrates by means of cross-shore and alongshore transport by waves. Cheniers are present in front of the Demak coastline and are believed to have a positive effect on the coastline stability (EcoShape, 2015). Due to its profile, a chenier ensures a sufficiently large gradient in wave energy, while allowing for onshore sediment transport. This way, accretion is enhanced at the sheltered shoreline and mangroves are able to establish. A visualisation of the impact of a chenier on the coastal morphology is presented in Section 3.3.3.

Based on a rehabilitation strategy formulated by Winterwerp et al. (2013), the concept of 'hybrid engineering', i.e. enhancing the trapping of fine sediments in a natural way, has been applied at the Demak coast by means of installing permeable structures. These wooden structures attenuate wave energy while letting through suspended sediment, as can be seen in Figure 2.6. In the quiet zone behind the structures, the fine sediments settle and surface elevation is created in a natural way (EcoShape, 2015).

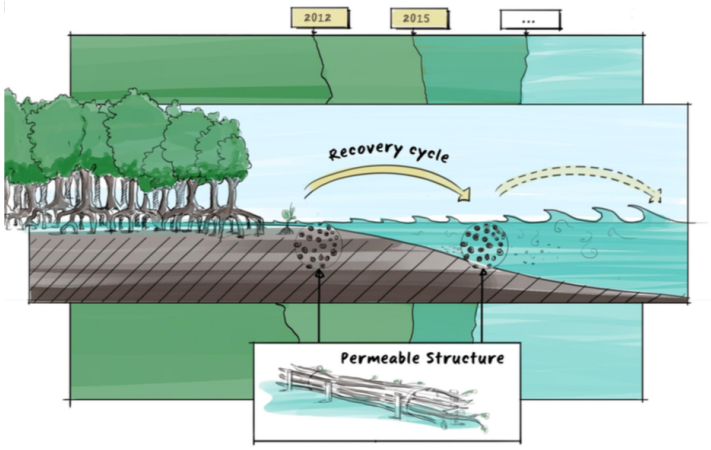

Figure 2.6: Recovery of the intertidal area with permeable structures made of wood (Winterwerp, 2014)

2.4.2 Windows of Opportunity

Whereas Section 2.4.1 focused on the rehabilitation strategies based on sediment processes, this section elaborates on the ecological part of the mangrove rehabilitation process. This mainly comprises the effect of hydrodynamics and sediment dynamics on mangrove *growth*.

Balke et al. (2014) discussed that quantifying the effects of stochastic external forcings on critical transitions in ecosystems is essential in order to achieve restoration efforts. Aim is on the *Windows of Opportunity* (WoO) for vegetation establishment. A positive biogeomorphic feedback for vegetation growth can be induced by disturbance-free periods of a minimum critical duration. By analysing time series for variability in external forcings, threshold dynamics can be identified and potential events for inducing this feedback can be discovered. The Windows of Opportunity for mangrove colonisation were described by Balke et al. (2011). It is important to stress that these WoO only hold when an initial condition is met: seed availability. In practice, the periods in which seeds are available differ per species. However, in this research it is assumed that seeds are available at any time.

A simple schematisation of the WoO for mangrove establishment is presented in Figure 2.7. The numbers 1 to 4 represent the conditions that should be met in chronological order to allow for mangrove establishment. In the case that seed dispersal has occurred and seeds are available to settle, mangrove establishment can be achieved if the thresholds defined by Balke et al. (2011) are met. A minimum inundation-free period must take place in order to allow the seedlings to anchor their roots into the soil to prevent them from floating. Then, during inundation periods, the wave- and current induced bed shear stresses should remain sufficiently low for a certain period to prevent dislodgement. Furthermore, the disturbances from erosion around the seedlings may not expose the root system which would exacerbate the possibility of dislodgement. During the periods in which certain threshold conditions may not be

exceeded, the roots of the seedlings have to grow large enough in order to pass through to the following step.

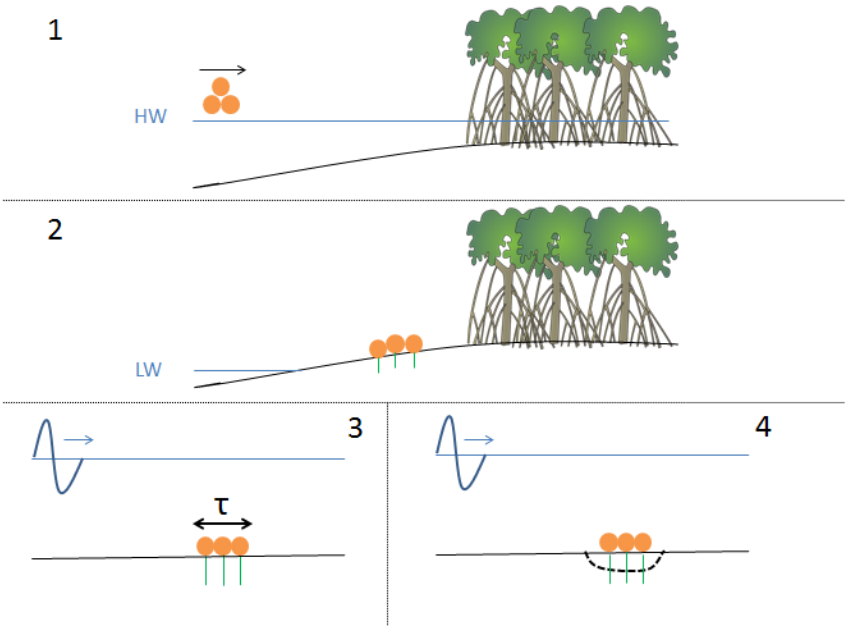

Figure 2.7: Simplified schematisation of the thresholds that need to be achieved for establishment of an *Avicennia alba* seedling. 1) Seedling dispersal to the mangrove fringe during a HW event, 2) a minimum inundation-free period to allow the seedlings to anchor in the soil, 3) a minimum period of low bed shear stresses to prevent dislodgement and 4) minimum disturbances from erosion around the roots of the seedlings.

In this research the focus lies on stages 2 and 3 from Figure 2.7. Hu et al. (2015a) schematised these stages in terms of bed shear stresses as can be seen in Figure 2.8, where stages 2 and 3 are characterised as *WoO1* and *WoO2*, respectively. WoO1 represents the inundation-free period during which the bed shear stresses are zero. According to Balke et al. (2011), this inundation-free period has a duration of around five days for *Avicennia alba* seedlings. When the first stage has been completed, the maximum bed shear stress is determined by Equation 2.12 (Hu et al., 2015a):

$$\tau_v = k(t - t_{WoO1}) + \tau_{cr;ero} \tag{2.12}$$

in which τ_v is the critical shear stress for seedling dislodgement, $\tau_{cr;ero}$ is the critical shear stress for sediment mobilisation, k is the growth rate of τ_v in Pa/h, and t is the time after seedling dispersal. The value of k has been estimated at $3.3e^{-3}$ Pa/h by Balke et al. (2011). It should be noted though that, since k depends on the growth rate of the seedlings and on the strength in Pascal per unit root length, and thus on vegetation properties and local environmental conditions, a large uncertainty lies in this value. Based on the measurements, a minimum k value of $1.2e^{-3}$ Pa/h and a maximum of $6.3e^{-3}$ Pa/h could be found.

The presence of $\tau_{cr;ero}$ in Equation 2.12 shows that the soil characteristics are also essential for seedling establishment and largely determine the required length of the Windows of Opportunity. Balke et al. (2011) found that when seedlings were prevented from floating, they could resist shear stresses of 0.17 $N/m^2/$, indicating that $\tau_{cr;ero} = 0.17$ N/m^2. It is important to understand that this value is variable and dependent on the site specific soil properties.

Although the main focus of this research lies on discovering WoO for mangrove growth, it is also important to realise that WoO do not only reflect development of vegetation. Conversely, a stable ecosystem also remains responsive to external forcing (Balke et al., 2014). Take for instance a healthy mangrove forest that is subject to erosion. When the external forcings, e.g. waves, surpass certain thresholds in terms of shear stress and duration, equilibrium state systems are able to change state.

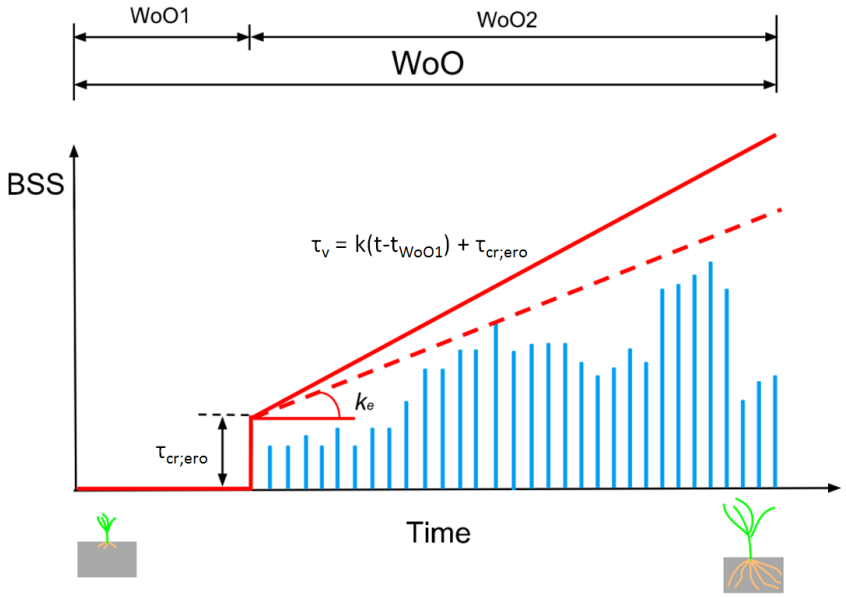

Figure 2.8: Schematisation of an inundation-free period (WoO1) followed by a period of low bed shear stresses (WoO2) determined by a vegetation strength development curve. The red dashed line presents the maximum slope of the bed shear stress time series (Hu et al., 2015a).

3. System analysis of Demak coastal zone

This research is a case study of the BioManCo project which is carried out by a team of PhD students: Celine van Bijsterveldt, Silke Tas and Alejandra Gijón. The BioManCo project is a part of the Building with Nature project in Demak (Indonesia) which aims on restoring sections of land along 20 km of shoreline and introduces more productive and sustainable land-use in Demak district (EcoShape, 2015). In order to become familiar with the area of interest, this chapter presents a geographical overview and describes the meteorological and physical characteristics that influence the physical processes that are reviewed in order to understand the morphological behaviour of the Demak coastline. A part of the system analysis is based on observations during field trips of the BioManCo team. Hereafter, the participants of this team are referred to as: BioManCo (2018).

3.1 Area of interest

The area of interest is presented in Figure 3.1. On the left side, the situation of the Demak province is presented. Demak is located in the centre of North-Java and faces the Java Sea. The coastline of Demak is suffering from a severe coastline retreat of hundred's of metres to kilometres which is presented on the right side of the figure. The transects that are selected for this research are located inside the red rectangular in the right figure. Section 3.3 further elaborates on these transects.

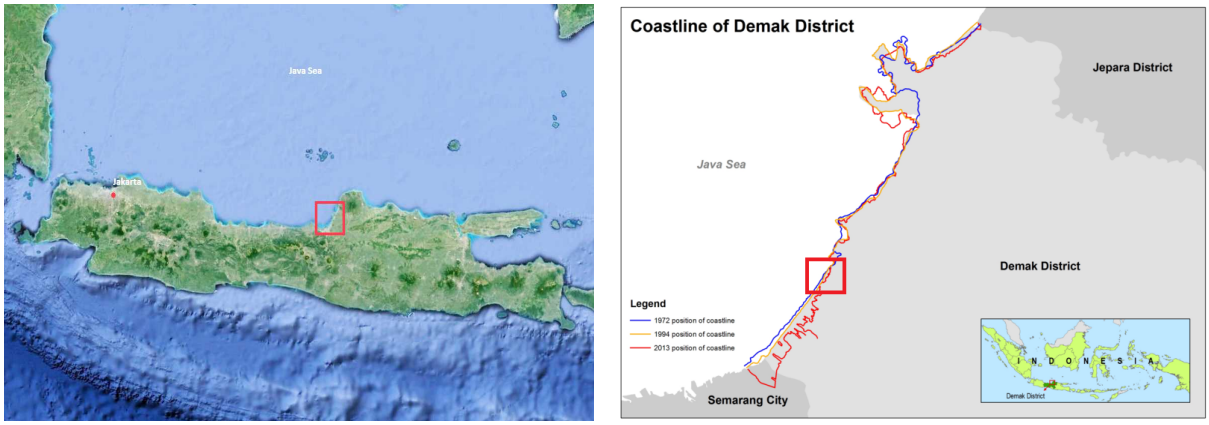

Figure 3.1: Left: Location of Demak (in red) on the island Java (Indonesia) with the Java Sea at the north side (source: Google Earth). Right: Demak coastline development between 1972 (blue line) and 2013 (red line). The red rectangular covers the location of the transects.

3.2 Meteorological and physical characteristics

This section describes the meteorological and physical characteristics of the Demak coast. This comprises an explanation of the occurrence of monsoons, the present hydrodynamics and the morphology of the coastline.

3.2.1 Monsoons

The meteorological characteristics play an important role in the seasonal variability of the coastline morphology and are therefore essential to understand. The meteorology of South-East Asia is largely influenced by the presence of monsoons. The reason of occurrence of monsoons was extensively described by Wyrtki (1961).

Unequal heating across the Earth's surface causes atmospheric pressure differences around the globe. Low pressures are associated with high winds, low air and atmospheric lifting, and result in heavy cloud formation and rainfall. The low equatorial pressure trough, i.e. a consistently low pressure zone, moves according to the position of the sun, crossing the equator twice a year. Between the low and high pressure

zones, monsoons develop.

Two types of monsoons are distinguished. The north-west monsoon occurs between October and April with dominant westerly winds across the Java Sea and is also associated with the wet season. The strongest winds are observed from December to February and these are also the wettest months. In April, the equatorial trough starts to move quickly to the north, inducing prevailing southerly winds in May. Due to these changing conditions the south-east monsoon starts to blow over the Java Sea and announces the dry season, accompanied by calm weather conditions. In July and August, the south-east monsoon is fully developed. Reversal occurs again when the equatorial trough begins to move southwards in October where the north-west monsoon commences.

3.2.2 Physical characteristics

The hydrodynamics and morphology of the investigated coastline are described here. The coastline of Demak is an intertidal area situated along the Java Sea and is subject to the dynamics of tides, waves and currents of which the dominant magnitudes and directions will be discussed here.

3.2.2.1 Tide

The tidal constituents that are present at the Demak coast are given in Table D.1. From the tidal constituents it can be deduced that the tide in Demak has a mixed character with dominant diurnal characteristics and small semi-diurnal components. The variation in tidal water levels, as presented in Figure D.1, is highly irregular and daily inequalities are clearly present. Also, the tidal signal shows the monthly variations of the spring-neap cycle. The tidal range varies between 40-60 centimetres and can be characterised as a micro-tidal regime (Bosboom and Stive, 2015). When semi-diurnal and diurnal components synchronise, the tidal range can be slightly larger (Winterwerp et al., 2014). Because of the relatively small variations in water level, the tidal currents are also small. Maximum tidal currents are around 15 cm/s and expected to be directed perpendicular to the Demak coastline (EcoShape, 2015). For muddy coastal systems, this magnitude of current velocity results in bed shear stresses around 0.03 Nm^{-2}, which has a negligible effect on the morphology (see Appendix D.1).

Additionally, it should be noted that the average water level at the Demak coast varies throughout the year, apart from the tidal signal. A simplified analysis of the absolute water levels measured at the tidal station of Semarang (described in Appendix D.1.2) showed that the average water level is relatively low from February up to and including April and in August and September. From October up to and including January and in the months May, June and July, the water level is relatively high. The difference between a yearly low and high average water level can increase up to 30 centimetres. This affects the situation of the coastline bathymetry compared to MSL and thus influences the maximum inundation-free period of a location at the coastline which determines the possibility for mangrove re-establishment.

3.2.2.2 Waves

Over a period of fourteen years, the wave climate was measured at a station near Semarang. In this period, a mean wave height of 0.46 m was observed with maximum offshore wave heights between 2.6-3.0 m and periods of about 5.5 s (EcoShape, 2015).

For the Demak coastline, the relevant waves come from the north and north-west, while mainly from the north. At a distance of 3.5 km from the coastline, wave heights of 1.8 m have been observed with maximum significant wave heights of 1.5 m and periods of 5.5 s (Winterwerp et al., 2014). The relevant waves occur during the north-west monsoon and approach the Demak coastline almost constantly perpendicularly. During the south-east monsoon, the wind is directed offshore, resulting in hardly any nearshore waves.

3.2.2.3 Currents

The atmospheric pressure distribution in the monsoons is very stationary, indicating that the winds are highly constant. This high constancy together with the regular appearance of monsoons causes that the ocean currents show the same characteristics as the winds (Wyrtki, 1961). This seasonal shift of residual ocean currents affects the sediment transport along the north coast of Java. During the north-west monsoon the currents are directed towards the East and thus towards the shoreline. In the north-west monsoon these currents are accompanied by a large fresh water discharge because of the extensive rainfall. Consequently, a gravitational circulation is induced which keeps fine sediments close

to the shore (EcoShape, 2015). During the south-east monsoon, the direction of residual ocean currents shift towards the west, into the Java Sea, so that no large scale sediment transport occurs near the coast.

3.2.2.4 Morphology

The Demak coastal zone is very shallow, with slopes of about 1:1000 that extend for about 1 km, after which the slope increases to approximately 1:500. Due to the mild slope, the waves approach the shoreline approximately perpendicularly since the effect of refraction is negligible. The seabed and sub-bottom are extremely muddy, though the sediment composition along the shoreline varies spatially. During field observations by BioManCo (2018), locations of fluid mud were observed, indicating that knowledge of fluid mud characteristics is desired. BioManCo et al. (2018) are currently conducting laboratory experiments (August 2018) in order to analyse the soil properties in Demak. By means Malvern tests, the grain size distributions of mud samples have been determined. These results show that on average 80% of the sediment mass is distributed over grain sizes smaller than 63μm, representing cohesive particles. Approximately 20-30% consists of non-cohesive fine sand. With a dry density of 585 kg/m^3, the mud can be characterised as light sandy mud (Mitchener and Torfs, 1996). More information about the laboratory experiment can be found in Appendix D.2.

The spatially varying sediment composition can be found in the presence of cheniers along the Demak coastline, as was discussed in Section 2.4. The cheniers are sandy and thus have a different sediment composition than the regular muddy areas on the tidal flats. Because of their large influence on the coastal morphology the migrating character of the cheniers is essential for the local coastline development. However, little is yet known about the dynamics of cheniers, i.e. chenier formation, propagation direction and sediment sources. A more detailed description of the local morphology in the area of interest is described in the remaining of this chapter.

3.3 Description of transects

This section zooms in on the transects that were analysed for this research. First, the most recent situation of the transects is sketched after which the historical development of this piece of coastline is described. For the analysis of the historical development, satellite images are used (source: Google Earth). It is important to notice that the satellite images are not taken during the same part of the tidal cycle which complicates defining the coastline position. However, the images are used for a first impression and will not be relied on heavily.

3.3.1 Situation sketch

Two cross-shore transects along the Demak coastline have been selected and are presented in Figure 3.2. In the summer of 2017, one location with mangrove retreat and another with mangrove colonisation were chosen. The locations will be referred to as 'eroding transect' and 'accreting transect', respectively. At these situations there are no permeable structures along the coast. Nevertheless, mangrove colonisation is occurring in the accreting transect, which is the main reason that these transects are interesting to analyse. By understanding the natural physical processes that affect the coastline morphology, more insight can be gained about the hydrodynamic conditions that must be created at vulnerable mangrove-mud coastlines in order to restore the mangrove population.

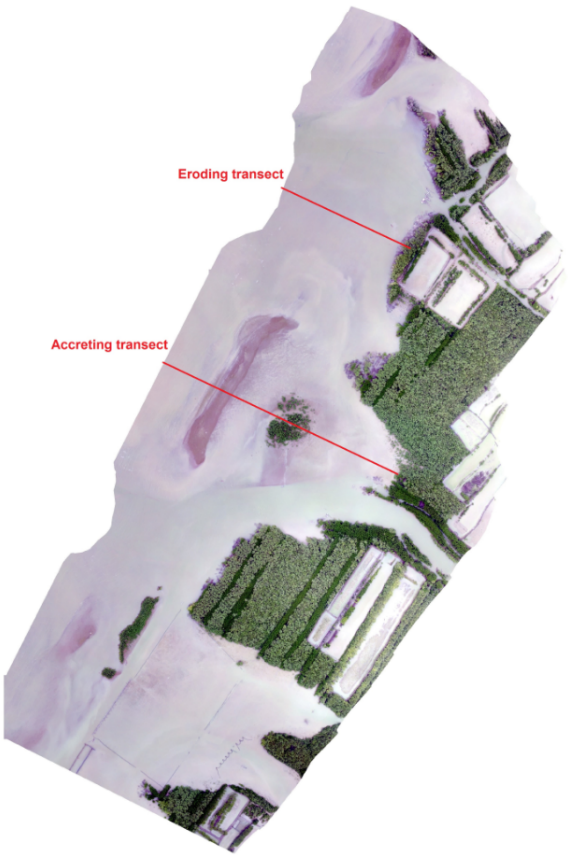

Figure 3.2: Overview of cross-shore transects. Both transects are directed towards the north-west in offshore direction (BioManCo, 2018)

The morphology of both transects differs, as can be seen in Figure 3.2. The measurements of the bathymetry can be found in Appendix D.3 and schematisations are presented in Chapter 5. The accreting transect is characterised by a chenier (the dark bar in the figure) and a small vegetation patch in between the chenier and the coastline. The grain sizes along both transects are shown in Table D.2 and the locations mentioned in this table are visualised in Figure 4.1. Looking at the grain sizes (excluding SED 181 at the chenier), it can be seen that the eroding transect contains coarser sediment ($D_{50} \approx 24\mu m$) than the accreting transect ($D_{50} \approx 12\mu m$). This is also supported by the field observations from BioManCo (2018), during which walking along the eroding transect was experienced to be much easier due to the relatively rigid bed. This changed towards the shore, where the bed became more muddy.

Along the accreting transect, the soil is much softer overall and gets also more muddy towards the shore. The latter is supported by the smaller grain sizes towards the shore which deviate between 5-10 μm. The smallest grain sizes are found inside the mangrove forest. Overall it can be stated that the sediment is rather silty, containing both sand and clay, and therefore the cohesion of grain particles can expected to be low. The chenier in the accreting transect is characterised by a rather sandy sediment composition ($\approx$ 145 μm). The sandy structure of cheniers is an already known feature (EcoShape, 2015). The vegetation patch in the middle of the accreting transect is also relatively sandy compared to other parts in the structure. This vegetation patch is an old chenier which has been colonised by mangroves (BioManCo, 2018).

Just south of the accreting transect, an outlet of a small channel, or tidal creek, is present. Little is known about the hydrodynamic and morphological properties of this channel. Since the grain sizes are small, only small hydrodynamic forces are needed to mobilise sediment. Therefore it is likely that this channel has some influence on the sediment balance of the accreting transect. For instance, supply of sediment during ebb tidal forces. However, regarding the lack of knowledge about this part, the channel

will be neglected in this research.

As mentioned earlier, the Demak coastline is characterised by its dynamic morphology. In Section 3.3.3, focus lies on these dynamics and mainly on the movement of cheniers along the coastline. This is an important aspect of this research because of the large influence of cheniers on the coastline morphology.

3.3.2 Mangrove colonisation

In the Demak area, five different mangrove species have been found of which the *Avicennia marina* and *Rhizophora mucronata* are the most dominant (EcoShape, 2015). The *Avicennia marina* is a pioneer specie of which natural recruitment has been observed in the accreting transect, as mentioned in Section 3.3.1. In front of the mangrove forest, young mangroves have been establishing and also on the inner side of the chenier, some mangrove colonisation was found. Cheniers appear to offer good conditions for mangrove establishment. The vegetation patch in the accreting transect is an old chenier and also in front of the coast of Timbul Sloko, just south the project area, mangrove seedlings have been found on a chenier that has developed during the winter period of 2017-2018 (personal communication with Celine van Bijsterveldt). The fruiting season differs per mangrove specie. Kitamura (1997) investigated mangrove species at Bali (Indonesia) and found that the fruiting season of the *Avicennia marina* is generally between December and February. However, BioManCo (2018) found that *Avicennia marina* mainly establishes during the south-east monsoon period, between April and August. This indicates the uncertainty about the actual fruiting season of mangrove species. The other pioneer mangrove specie, *Avicennia alba*, has been found the establish mainly during the north-west monsoon period (BioManCo, 2018).

3.3.3 Historical coastline development

In the introduction of this section it was already mentioned that a detailed analysis of the historical coastline development based on satellite images is complicated because of the intertidal character of the area of interest. The interpretations in this section must therefore be understood as an initial impression about the behaviour of the morphology in the area.

In the summer of 2017, the transects were characterised as 'eroding' and 'accreting'. However, during the winter of 2017-2018, the chenier in the accreting transect disappeared, and a chenier appeared in the eroding transect. This implies the dynamic character of the transects. Therefore, it is interesting to analyse the historical evolution of both transects. In Figures 3.3 and 3.4, the transects are represented by the red lines. By changing the time of the image, insight can be gained about the morphological development around the transects. The focus hereby lies on the dark areas on the land which represent vegetation. An increase of vegetation during the past few years is visible at the accreting transect, whereas a slight retreat can be observed in the eroding transect.

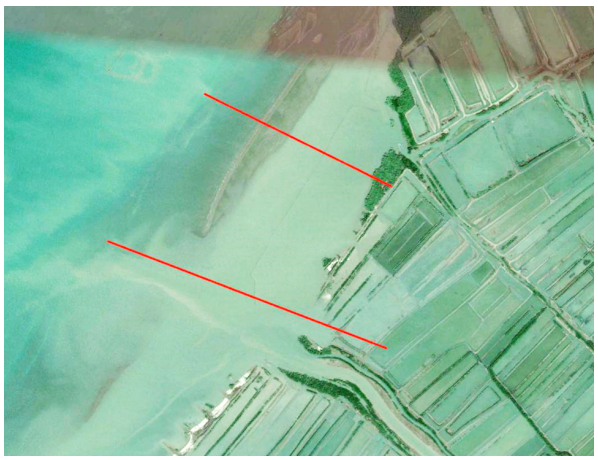

Figure 3.3: Situation February 2010 (source: Google Earth)

Figure 3.4: Situation September 2017 (source: Google Earth)

The chenier in front of the coast is of major importance for the state of the underlying coastline. The chenier shelters the coastline by attenuating waves and thus possibly supports accretion (EcoShape, 2015). It is therefore hypothesised that mangroves are colonising in the accreting transect due to the presence of this chenier. In Figure 3.4 it can be observed that the eroding coastline is currently not sheltered while this was the case in Figure 3.3. The photographs thus support the hypothesis of the influence of the chenier.

Due to the importance of the chenier, it is desired to understand the behaviour of these sandy structures. How the cheniers exactly move is yet unknown. From the most recent field trip, it was noticed that the chenier in the accreting transect (see Figure 3.4) had disappeared from the initial location in the accreting transect (BioManCo, 2018). In the eroding transect, a chenier has appeared instead. The question arises whether the chenier has moved in alongshore direction from the accreting transect towards the eroding transect, or that a new chenier has developed as a result of cross-shore bar propagation.

In Figures 3.5 and 3.6, two other historical moments are selected. These images, together with the figures presented above, give an idea of the dynamic character of the coastline. The locations of shallow areas change relatively fast, resulting in an unstable bathymetry along the transects. In Figure 3.6, two narrow bars tend to enter the transects. These narrow bars could be an indication that the cheniers are fed from the offshore direction. Also, by comparing Figures 3.5 and 3.6, it seems like the shoreline is situated more in seaward direction in 2015 than in 2012. Possibly, accretion has occurred during this period. Figures 3.5 and 3.6 show that the chenier is widely spread in alongshore direction. This can not be observed from the most recent satellite image (see Figure 3.4), but it can support the sandy bed composition in the eroding transect. It might be an indication that the chenier is much larger than can be seen in Figure 3.4, and that the height of the chenier varies significantly in alongshore direction.

Nevertheless, due to the limited knowledge, the formation of cheniers will not be elaborated on further in this research. It is however important to notice that the bathymetry of both transects changes constantly which must be taken into account during the analysis of the wave data collection. Since the bathymetry was not measured in detail before the data collection period, assumptions regarding the bathymetry profile must be taken with care.

Figure 3.5: Situation September 2012 (source: Google Earth)

Figure 3.6: Situation October 2015 (source: Google Earth)

4. Methodology

Two main research methods have been applied: a data analysis and the use of the numerical model XBeach. In this chapter, these research methods are described in more detail. It is important to notice that the collection of data was carried out by the PhD students of the BioManCo project (BioManCo, 2018) and is not a part of this research. Nevertheless, the experimental settings are extensively described in order to understand the methods that are used during the data analysis. The experimental set-up, data processing and the data analysis methods are described in Section 4.1. Section 4.2 elaborates on the XBeach model set-up. Furthermore, the methods for identifying WoO and the modelled scenarios are described here.

4.1 Data analysis

The goal of the data analysis is to gain insight into the transformation of waves along the transects and to correlate the wave forcing to bed level variations. During a summer and a winter period, data from two transects along the Demak coastline was collected, an eroding and an accreting transect. The geographical situation of these transects was described in detail in Section 3.3. The summer data represents the calm southeast monsoon, whereas the winter data is collected during the northwest monsoon with more severe weather conditions. Since this research is focused on the winter period, the experimental set-up of the summer period is neglected here and can be found in Appendix B.1. In this section, the experimental set-up of the winter period is presented and the methods are described that are used to analyse the collected data.

4.1.1 Experimental set-up

Figures 4.1(a) and 4.1(b) present schematisations of the winter set-up of the eroding and accreting transect, respectively.

OSSI Wave Gauges (hereafter called Wave Loggers (WL)) and SED sensors were deployed along the transects. Both instruments collect pressure data whereas the SED sensors also measure the local bed level elevation by means of light sensors. Furthermore, one offshore wave buoy is deployed, at a distance of 12 kilometres from the coastline (6.826495° S; 110.416680° E), at a water depth of 12 metres. This wave buoy measures wave height, wave period and the wave direction. Detailed descriptions of the instruments can be found in Appendix B.2. For a clearer overview during the analysis, the instruments have been renamed compared to their original names during deployment. The new names associated to the old instrument names are presented in Table 4.1.

Table 4.1: Names of the instruments as used during this research compared to the original instrument names.

Eroding transect		**Accreting transect**	
New	Original	New	Original
E1	WL 43	A1	WL 45
E2	WL 44	A2	SED 180
E3	WL 41	A3	SED 181
E4	WL 27	A4	SED 179
E5	SED 176	A5	WL 42
E6	SED 124	A6	SED 178
		A7	SED 174
		A8	SED 177
		A9	SED 175

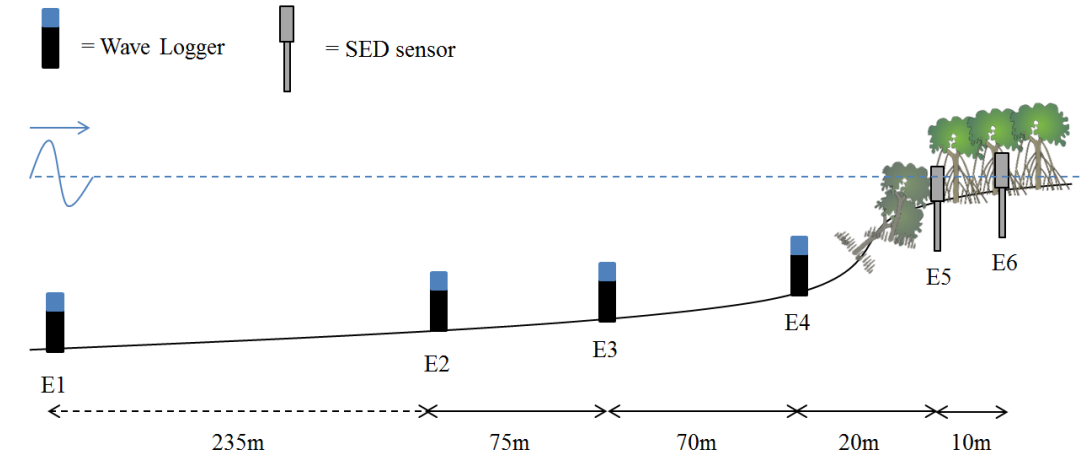

(a) Eroding transect

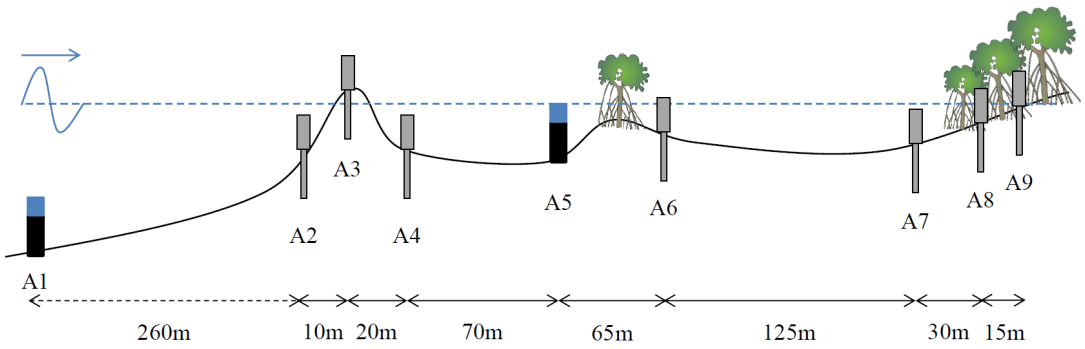

(b) Accreting transect

Figure 4.1: Schematisations of the experimental set-up during winter measurements. Note that the schematisations are not on scale and only give a simplified impression of the actual bathymetries.

4.1.2 Data processing

Although data has been collected from end November 2017 until March 2018, the measurement period over which the wave data will be analysed is: **25 November - 5 December 2017**. This is based on a calibration analysis that has been carried out because several wave loggers appeared to be overgrown with barnacles, which affected the sensor sensitivity (see Appendix B.4). In order to associate the wave data with the bed level changes, the analysed measurement period of the SED sensors is therefore reduced to the same length. Additionally, complications arose with the SED sensors that were deployed around the chenier (A2, A3 and A4). These complications happened to affect the measurements after the considered measurement period of 25 November - 5 December 2017 and are described in Appendix B.5.1 and B.5.2.

The processing of raw pressure data from the wave loggers and SED sensors is done by means of a series of *MatLab* and *R* scripts of which the settings are extensively described in Appendix B.3.

4.1.2.1 Bathymetry

Local bathymetry data was available, based on depth measurements at the locations of the deployed instruments (see Appendix D.3). A depth profile relative to mean sea level (MSL) was obtained by correcting the measured water depths with the corresponding water level based on the stage of the tidal cycle during which the depth was measured. It is important to note that the MSL was defined based on the average water level around the period of the depth measurements. As mentioned in Section 3.2.2, the average water level varies throughout the year with the average water level being around 10 cm higher during the northwest monsoon compared to the southeast monsoon (BioManCo, 2018). During this research, MSL refers to the average water level during the winter period, i.e. the northwest monsoon. Moreover, it should be noted that for the section in between consecutive measurement instruments a depth profile was assumed based on the system analysis in Chapter 3.1.

4.1.2.2 Wave analysis

By means of a wave analysis, the relevant dissipation processes that drive the wave transformation along the transects are explored.

The raw pressure signal is converted into spectral wave parameters, which is explained in Appendix G.2.3. This results in time series of spectral significant wave heights (H_{m0}) and peak periods (T_p) which will be used mainly during the wave analysis. Sometimes, the root-mean-square wave height (H_{rms}) has to be used which is an average wave parameter based on a wave-by-wave analysis and emphasizes on the largest waves from the wave series. In these cases, the relation $H_{rms} = 0.7H_{m0}$ is used for conversion. It should be noted that this conversion lacks accuracy, since the largest waves (which are the focus of H_{rms}) are already averaged out during the determination of H_{m0}.

By dividing the transects into sections, i.e. a distance between two consecutive measurement instruments, the energy dissipation along each section is calculated by means of the wave friction coefficient (f_w). This coefficient determines the amount of wave energy that is dissipated by means of *bottom friction* only. By comparing the calculated values for f_w with f_w values that correspond to intertidal mud flats according to Lacy and MacVean (2016), it can be examined whether bottom friction is the only dissipation process or whether other processes are likely to occur. It is important to notice that the wave friction coefficients are determined for situations when all the wave instruments are submerged in order to prevent that extremely large friction coefficients are acquired as a result of the absence of waves at a certain location. A detailed description of this calculation is attached in Appendix G.2.2.

4.1.2.3 Bed level analysis

The bed level changes that have been measured by the SED sensors are analysed by correlating the observations to corresponding bed shear stresses that occur at the same locations. The bed shear stresses are calculated by means of $\tau_b = c_f \rho u_b^2$, in which u_b is the near-bed orbital velocity that is calculated by means of H_{m0} and T_p. For irregular waves, H_{rms} should be used. However, since the raw data is processed into time series of H_{m0}, the large waves have already been averaged out and converting H_{m0} would underestimate the occurring wave heights considerably. Since the number of measurements for T_p significantly decreased towards the shore, T_p is assumed to be constant along the transects by using only the T_p values determined by the most offshore wave logger, E1 for the eroding transect and A1 for the accreting transect.

Based on the bed level analysis, the critical shear stress for bed erosion ($\tau_{cr;ero}$) on the locations of the SED sensors is determined. This is an important parameter in order to be able to identify Windows of Opportunity along the transect, as can be seen in Equation 2.12. The bed level analysis also gives insight into suitable locations for mangrove establishment, which are the locations that have a stable, or accreting bed level.

4.2 Modelling

A numerical model is used to calculate the hydrodynamics along a one-dimensional profile and is validated by means of the observed wave propagation along the transects. In this section, the model that has been used is described in detail. Section 4.2.1 describes which model has been selected based on the requirements for this research. Then, Section 4.2.2 and Section 4.2.2.4 elaborate on the model set-up and the boundary conditions, respectively. Furthermore, the results of the sensitivity analysis and model

validation are described in Section 4.2.3 and 4.2.4.

4.2.1 Model selection

Based on the model requirements, the numerical model XBeach is selected for the purpose of this research. The selection procedure is described in Appendix A. In order to keep the possibility for future morphological computations open, a modified version of XBeach has been chosen. Bendoni (2015) developed a *sand-mud module* for XBeach during his PhD research which accounts for processes that are characteristic for cohesive sediments which is not included in the original XBeach environment. The model is described in detail in Appendix A.4 and tests with the *sand-mud module* are presented in Appendix E.

Bendoni's version of XBeach is based on the 'surfbeat' mode. In this mode, the short wave variations on the wave group scale and the associated long waves are resolved (phase-averaging) (Deltares, 2015).

4.2.2 Model set-up

This section describes the model set-up of the accreting and the eroding transect. Note that these are two separate models between which the bathymetry and the application of physical processes differs. The models are one-dimensional (depth-averaged) and calculate hydrodynamics only.

4.2.2.1 Computational grid

A one-dimensional cross-shore grid is used which consists of a single gridline and ignores longshore gradients. Directional spreading is neglected, resulting in perpendicular waves. This is chosen since the slope is very mild (1:500-1:1000) and it is likely that the waves have already refracted towards the shoreline before they enter the modelled domain. Furthermore, the dominant wave direction is perpendicular to the coast as well, as can be seen in Figure B.20. Therefore, refraction inside the domain can be ignored by using a single directional bin instead of directional spreading.

The accreting and eroding transect are modelled over distances of 2235 m and 1935 m, respectively. The grid size is 10 m.

4.2.2.2 Bathymetry

The modelled bathymetries of the accreting and eroding transects are presented in Figure 4.2. As mentioned in Section 4.1.2.1, the bathymetry was measured only at the locations of the deployed instruments. Therefore, an uncertainty lies in the depth profiles in between consecutive instruments. Based on the model sensitivity analysis (described in Section 4.2.3), the modelled bathymetries have been adjusted slightly compared to the depth measurements. In the eroding transect, presented in the lower plot of Figure 4.2 a chenier is implemented, following from the data results in Section 5.2.3 and the sensitivity analysis in Section 4.2.3. Furthermore, the shore-edge of the eroding transect is adjusted slightly, as well. In the accreting transect, presented in the upper plot of Figure 4.2, the appearance of the chenier is adapted to achieve a good calibration.

The accreting transect contains vegetation at the locations of the vegetation patch (x = 1950 m - x = 1980 m) and inside the mangrove forest (x = 2130 m - x = 2235 m). It should be noted that the vegetation is not reproduced based on the real physical properties in the field, but configured for calibration purposes. The implemented vegetation is described in Appendix C.1.2.

Note that both bathymetries have their offshore boundary at x=0 m, at a depth of -4 m +MSL. This depth is chosen in order to minimise the effect of bottom friction at the boundary. The distance at which the transects are located from the boundary differs based on the geographical situation.

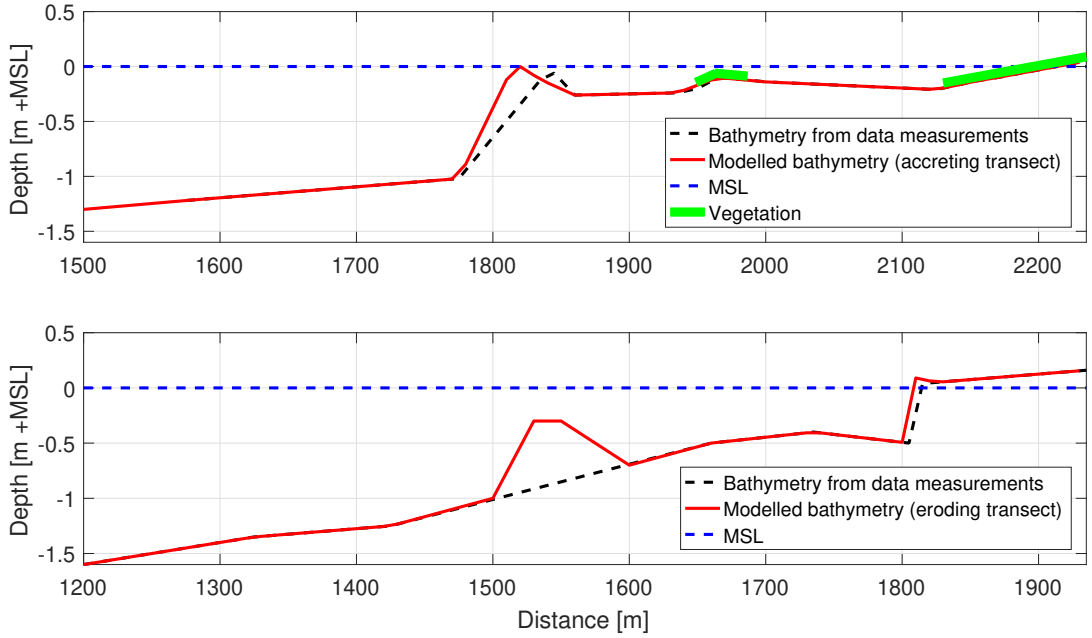

Figure 4.2: Modelled bathymetries of the accreting transect (upper plot) and the eroding transect (lower plot). Note that the distance is measured from the origin at a depth of -4m +MSL.

4.2.2.3 Physical processes

In the model, the physical processes of depth-induced wave breaking, bottom friction and vegetation are included. The short wave dissipation due to bottom friction is calculated by means of f_w. The value for f_w is determined based on the calibration tests that were carried out in order to reproduce the data results from Section 5.2.3. For the accreting transect, $f_w = 0.02$, for the eroding transect, $f_w = 0.05$. For bottom roughness, a Manning coefficient of 0.012 $s/m^{1/3}$ is used based on the numerical model of Demak's coastal zone by Smits (2016). Furthermore, the water density is set at 1025 kg/m^3, a standardised value for sea water.

4.2.2.4 Boundary conditions

The wave boundary condition is a time series of the spectral wave parameters H_{m0} and T_p that have been measured by the offshore wave buoy during the winter period (see Figure C.1). The tide boundary condition is a water level time series as measured at the tidal station of Semarang and is presented in the lower plot of Figure C.1 (JRC, 2018).

The flow boundary conditions at the lateral boundaries are Neumann conditions, indicating no gradients in surface elevation and velocity in the alongshore direction. Furthermore, the offshore flow boundary is weakly reflective and at the land a 'no flux' boundary is imposed.

4.2.3 Sensitivity analysis

A sensitivity analysis was carried out while calibrating the model with the wave data analysis results from Section 5.2. Besides f_w, which is the most sensitive calibration parameter to induce short wave dissipation, the bathymetry appeared to be a useful calibration parameter as well, certainly because of the uncertainties in the measured bathymetry along the transects (see Section 4.2.2.2).

The focus lied on severe dissipation events (between 26 November and 1 December) that were observed in the eroding transect between E1 and E2, of which an example is presented in Figure 4.3. It appeared that increasing the value for f_w did not suffice to achieve the observed dissipation rate, as can be seen in the left figure. The large dissipation rate could only be achieved by implementing a chenier, which can be seen in the right figure. Other shapes of obstacles between E1 and E2 must also be taken into account. For instance a combination between a lower obstacle and a higher wave friction coefficient (due to the larger grain sizes between E1 and E2). This option is presented in Section F.2.

The uncertainties in the bathymetry measurements have been taken advantage of during the calibration of the model, as can be seen at the slight adjustments in modelled bathymetry profiles (see Figure 4.2). The sensitivity analysis is described in more detail in Appendix F.

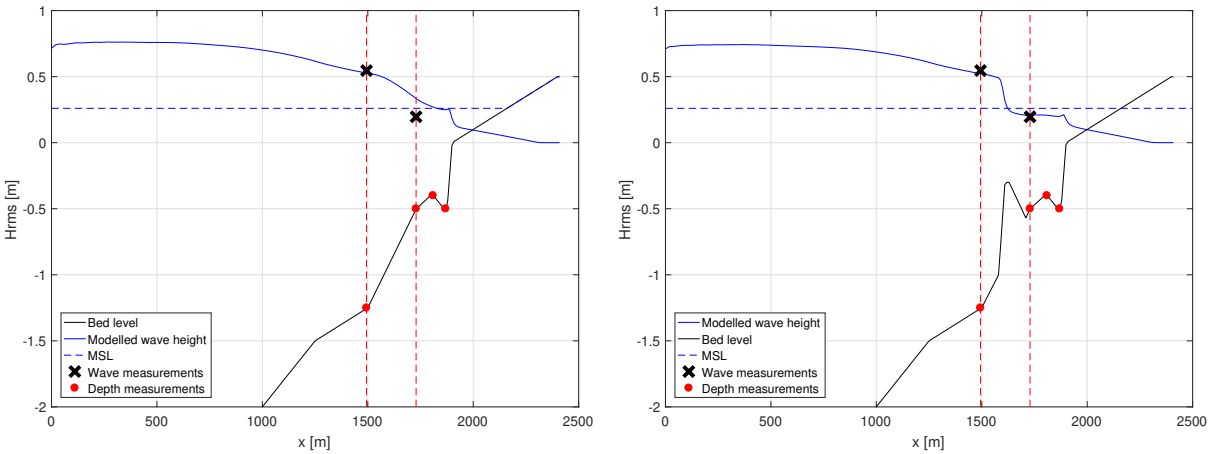

Figure 4.3: Comparison between the modelled and observed wave heights at E1 (left red-dotted line) and E2 (right red-dotted line), in the eroding transect. Left: a linearised profile between E1 and E2. Right: a chenier between E1 and E2.

4.2.4 Model validation

The models of the accreting and eroding transect have been validated by means of the wave data analysis from Section 5.2. During the modelling research, specific locations at each transect are analysed in detail. The model must be validated, at least at those locations. Since the Demak coastline is very dynamic, morphological changes occur relatively fast, but are excluded from the model. Therefore, it is important that the model is validated on a short term (a few days) in order to correctly reproduce the hydrodynamics along the initial bathymetry.

For the accreting transect, two locations are selected, A6 (behind the vegetation patch) and A7 (in front of the mangrove forest), because the possibility for WoO is expected to be largest here. The model reproduces the field observations accurately at both locations, as can be seen in Figure 4.4. Only the data peak in the shear stress plots (lower subplots) at 2 December is not modelled correctly. At this moment, a very low water depth was observed simultaneously with a relatively large water depth.

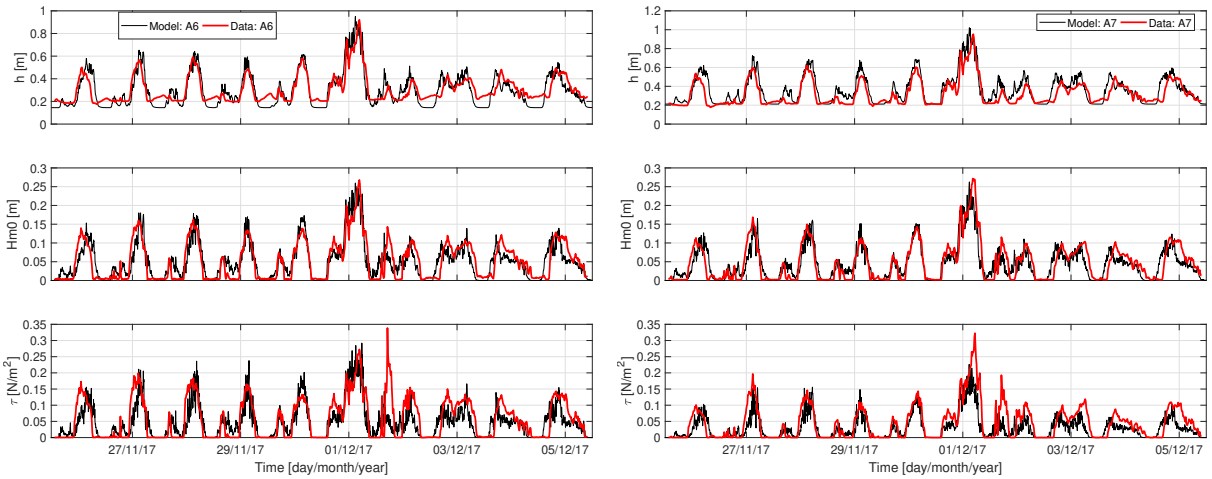

Figure 4.4: Model validation of the accreting transect. Left: A6 (behind vegetation patch). Right: A7 (in front of forest). The plots are structured as follows: Upper) water depth, middle) wave height, lower) bed shear stress.

In the eroding transect, the location in front of the steep shore edge (E4) and inside the forest (E5) are validated, as can be seen in Figure 4.5. The model computations at E4 are accurate, whereas at E5, the model overestimates the hydrodynamic activity after the 1 December storm event. An explanation for this could be that the water depths then hardly exceed 20 cm. Since the pressure sensors is located 20 cm above the bed, the instruments do then hardly measure wave pressure whereas the model does not have this limitation.

A more extensive description of the model validation can be found in Appendix C.2.

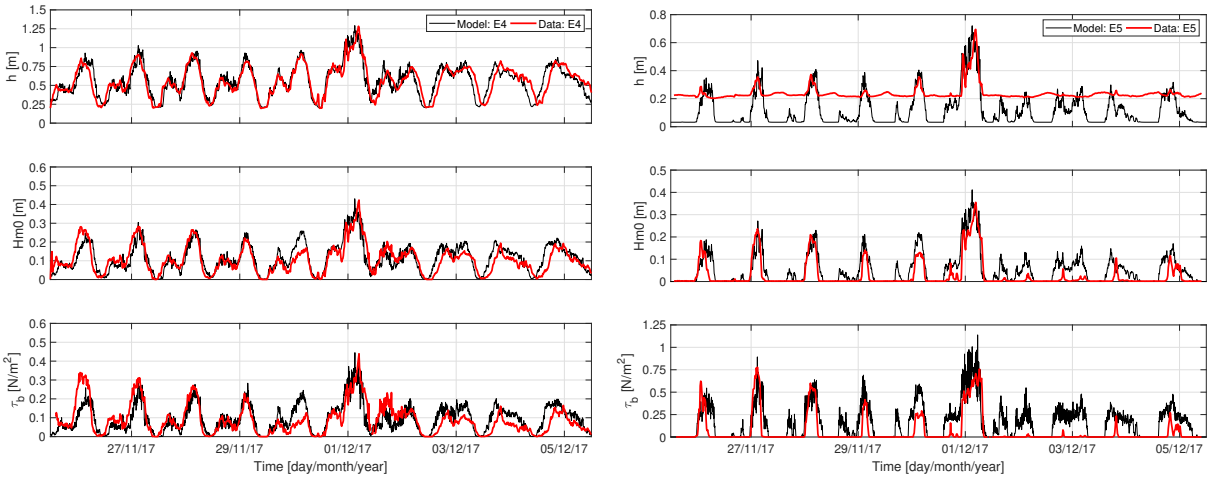

Figure 4.5: Model validation of the eroding transect. Left: E4 (in front of forest edge). Right: E5 (forest edge).

4.2.5 Identifying Windows of Opportunity

The validated models are used to identify Windows of Opportunity. The focus here lies on the accreting transect, where seedling establishment has been found to occur (BioManCo, 2018). Based on the bed level analysis in Section 5.2.6, the locations of A6 (behind the vegetation patch) and A7 (mangrove forest edge), which are (relatively) stable in terms of bed level, are selected. At these locations, time series of occurring bed shear stresses during the modelled time period are computed. Then, based on the threshold conditions defined by Balke et al. (2011) and Equation 2.12, the possibilities for mangrove establishment are examined. Initially, identifying WoO is done for the period 19 November-31 December 2017 (original case), in order to reproduce the events that occurred during this winter period. Furthermore, various

scenarios are implemented in the model set-up in order to analyse the effect of the chenier and the vegetation patch on the possibilities for WoO along the transect (see Section 4.2.6).

4.2.6 Scenarios

This section describes the scenarios that have been carried out with the model. For each scenario it is described how the scenario deviates from the original case and what the purpose of the scenario is. It should be noted that the different scenarios only deviate in terms of bathymetry and vegetation presence. Other physical processes remain unchanged.

4.2.6.1 Accreting transect

For the accreting transect, it is desired to qualitatively analyse the effect of the chenier and the vegetation patch on the observed hydrodynamics and the associated bed shear stresses along the transect. Apart from the original case, with the validated bathymetry, two scenarios are defined: 1) no vegetation patch, and 2) no chenier (see Figure 4.6). In scenario 1, the vegetation between x = 1900m and x=2000m is removed. For scenario 2, the chenier is replaced by a linear slope.

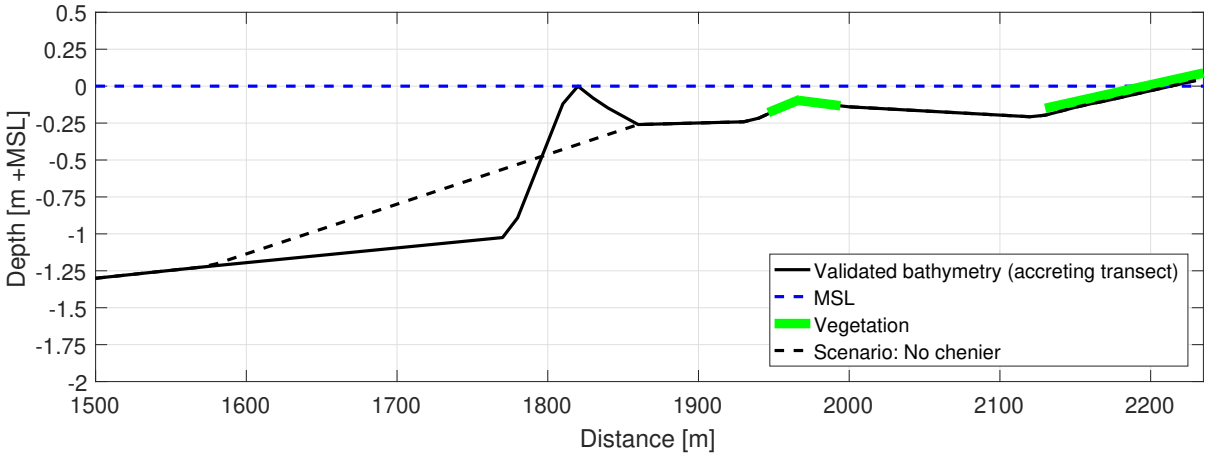

Figure 4.6: Modelling scenarios for the accreting transect.

4.2.6.2 Eroding transect

The purpose of modelling the eroding transect is to study the effect of the developing chenier in front of the shoreline, as was observed by BioManCo (2018) and also by the findings from the data analysis in Section 5.2. First, the effect of the chenier height on possibilities for shoreline accretion is studied by means of the scenarios: 1) chenier at -0.15m +MSL, and 2) chenier at 0m +MSL (see Figure 4.7). The observed bed shear stresses at two locations at the shoreline (E4 and E5) are therefore analysed for the different scenarios.

Furthermore, observations by BioManCo (2018) showed that seedling establishment occurred at a chenier in front of Timbul Sloko that had developed during the winter period of 2017-2018. By means of the eroding transect model, the shear stresses on the inner side of the largest chenier (chenier at 0m +MSL) are analysed in order to find an indication for the vegetation growth properties that are required to establish during the winter period.

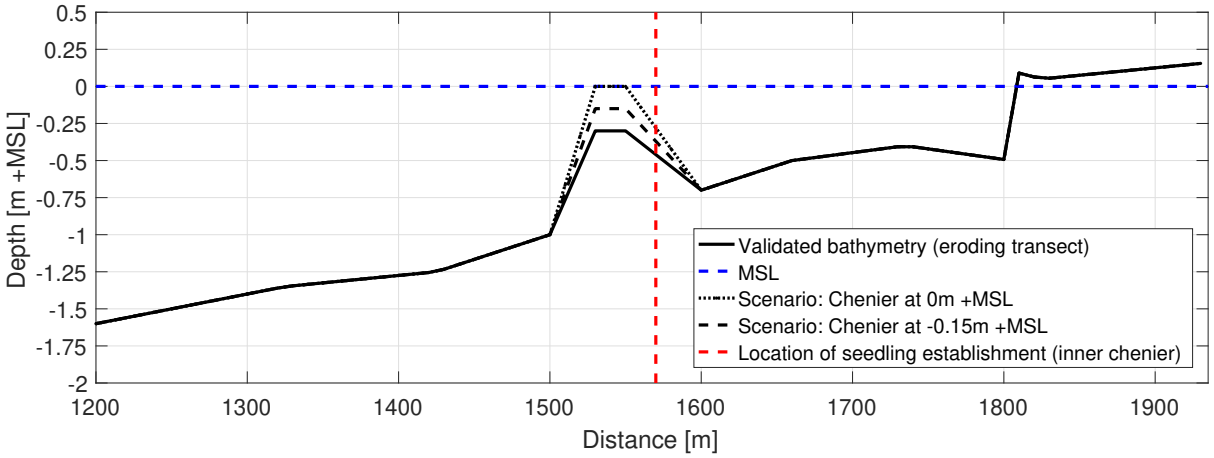

Figure 4.7: Modelling scenarios for the eroding transect.

5. Results

The results of the data analysis and modelling work are presented in this chapter. This chapter is structured as follows. First the results of the data analysis are presented, divided into a summer and winter measurement period, in Section 5.1 and Section 5.2, respectively. The modelling results are described in Section 5.3.

5.1 Data analysis: summer period

The summer data collection lasted from the 31^{st} of July 2017 until the 10^{th} of August 2017. During the summer monsoon, the wind was almost constantly directed offshore, resulting in hardly any nearshore waves.

The experimental setup of the summer measurement period is presented in Figure B.1. Due to the small height of the waves, only the wave parameters along the eroding transect were processed. This is done mainly in order to substantiate that the summer measurement period is not useful to perform a thorough wave analysis on. The resulting plots of this analysis are presented in Figure 5.1.

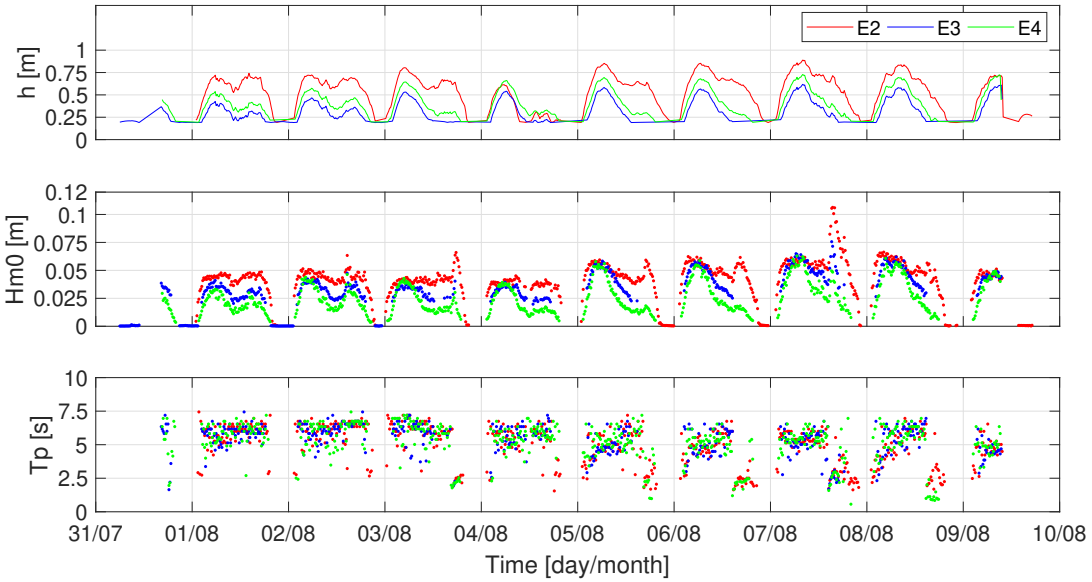

Figure 5.1: Time series of the wave parameters along the eroding transect during the summer measurement period (31 July-10 August). From offshore to nearshore: E2, E3, E4. Upper: water depths. Middle: spectral significant wave heights. Lower: peak wave periods. Note that the water depth was not measured below 20 cm because of the sensor height.

Figure 5.1 shows the development of h, H_{m0} and T_p along the eroding transect in time. From the time series it can be observed that the spectral significant wave heights (H_{m0}) are on average about 5 centimetres during high water for each location along the transect. Furthermore, the variations in wave height between the locations are minimal. This indicates that the wave energy is hardly dissipated by bottom friction along the transect, mainly because of the low wave heights.

Since the measurements of the peak wave periods (T_p) are noisy and irregular, wave periods above 10 seconds have been filtered out, explaining the white gaps in the time series. The average wave period lies around 5 seconds. The wave periods do not show a pattern from which information about wave propagation towards the shore can be deduced.

As expected, the measured bed level changes inside and in front of the forest (included in Appendix B.7) showed minimum erosion rates. The bed level is even accreting significantly, up to 1.5 cm within ten days. Based on Winterwerp et al. (2013) accretion would require a large offshore to nearshore gradient

in wave energy. During quiet conditions, this is likely not the case. Therefore, the accretion rates might be tidally driven, or the result of instrument sinking into the soft soil.

The present work will not elaborate further on the summer field data.

5.2 Data analysis: winter period

In this section, the data analysis results of the winter period are presented. For each transect, an analysis is carried out regarding the propagation of the wave height and the occurring bed level changes. The focus lies on comparing the hydrodynamic situations in both transects. First the bathymetries of both transects are presented. Then, the time series of spectral wave parameters along the transects are shown. The wave height attenuation along the transect is then analysed by calculating the wave friction coefficient that is necessary to achieve the energy dissipation. Next, the propagation of wave frequencies is discussed by means of a spectral wave analysis.

Finally, the observed bed level changes along the transects are presented and analysed by correlating these observations to the hydrodynamic environment.

5.2.1 Bathymetry and data locations

In Chapter 4, the positioning of measurement instruments along the transects is visualised. Unfortunately, the wave data of E6 (SED 124) was lacking and the pressure data of A3 (SED 181) and A4 (SED 179) seemed to be affected and is therefore unreliable (see Appendix B.5.1). In this section schematisations of the experimental set-up are presented for each transect, including markers for specific instruments and profile sections that will be referred to during the wave analysis.

Figure 5.2 presents the schematisations of the instruments along the eroding and accreting transects. These profiles are based on the bathymetry that was measured (see Appendix D.3). The bathymetry was *only* measured at the locations of the deployed instruments, indicated by the coloured crosses and dots where the dots represent the instruments that are not included in the wave analysis. The same colors for specific instruments will be used during the whole data analysis. The sections between the coloured crosses are marked with letters *A*-*E* and the corresponding dimensions are shown in Table 5.1. Note that the accreting transect is located closer to the Mean Sea Level (MSL) line and thus has a smaller overall depth profile.

Along the profile sections, a certain profile is assumed, based on field observations (see Section 3.3.3). In the eroding transect, the unknown sections are assumed to be linear since no irregularities in the bed profile were observed (BioManCo, 2018). In the accreting transect, a chenier and a vegetation patch are present, so that the profile is adapted non-linearly in these sections. The flat foreshore is based on EcoShape (2015) that describes that the intertidal flats extend to around 1 kilometre offshore with a slope of 1:1000. The steep chenier slope in section *A* is based on a depth profile from the summer measurements by BioManCo (2018), similarly as for the vegetation patch in section *C*. It should be noted that the assumed bathymetries along profile sections are highly uncertain.

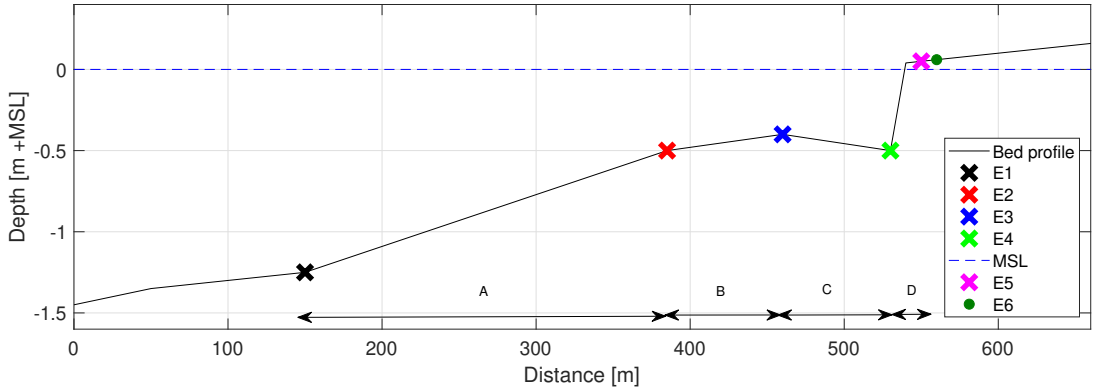

(a) Eroding transect

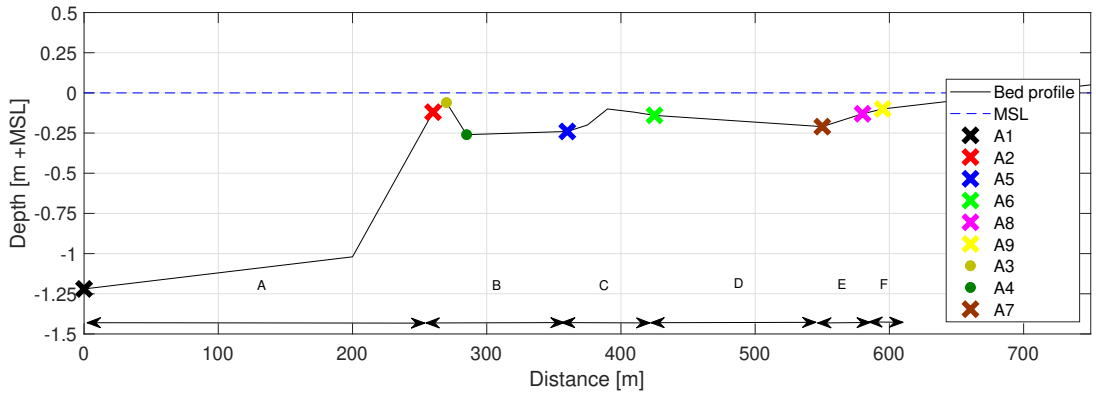

(b) Accreting transect

Figure 5.2: Schematisations of the measurement instruments that are used during the wave analysis. The bed profile represents the bathymetry as measured in the field with an increasing distance towards the shore. Note that the depths are only measured at the locations of the colored crosses and dots. The dots represent instruments that are excluded from the wave analysis. The letters represent a section between two consecutive instruments.

Table 5.1: Length of sections in between two consecutive measurement instruments

	Eroding	**Accreting**
Section	Length [m]	Length [m]
A	230	260
B	75	100
C	70	65
D	20	125
E		30
F		15

5.2.2 Spectral wave parameters

The time series of the water depths and spectral wave parameters along the eroding and accreting transects are plotted in Figure 5.3(a) and 5.3(b), respectively. In this section, each parameter is treated separately.

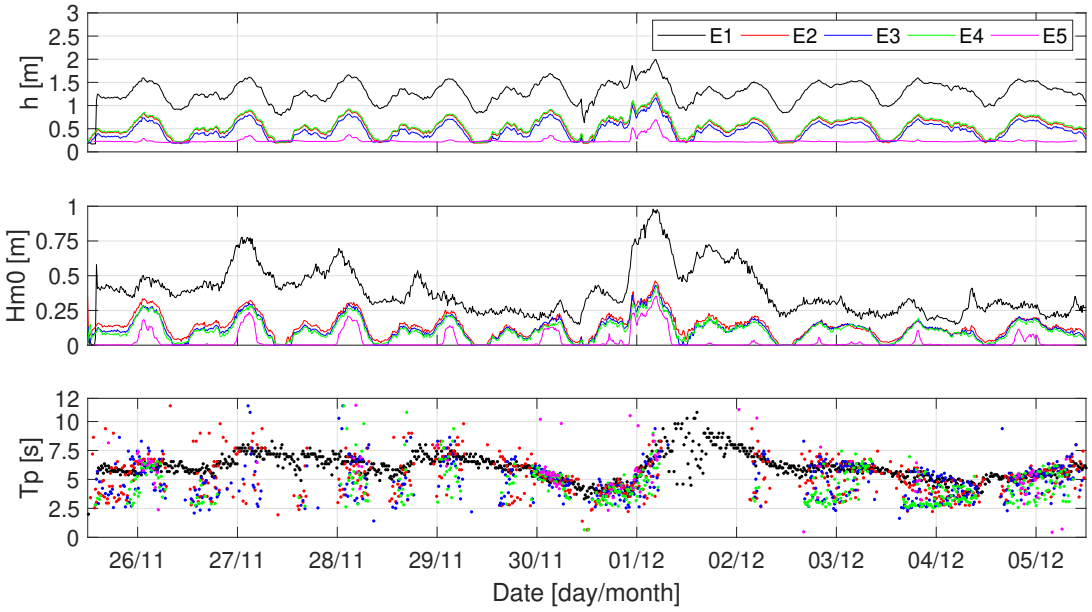

(a) Eroding transect

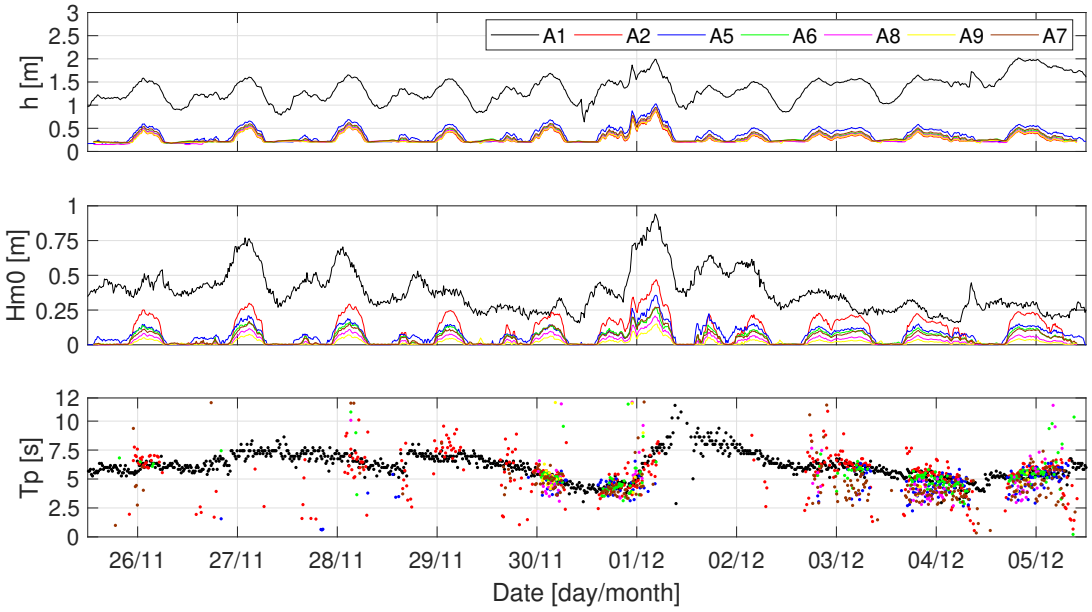

(b) Accreting transect

Figure 5.3: Times series of water depths and spectral wave paramaters for the eroding and accreting transect. Upper: water depth. Middle: spectral significant wave height. Lower: peak wave period. Note that the water depth was not measured below 20 cm because of the sensor height.

The upper graph shows the water depths for the various instruments along the transect. These water depths correspond to the bathymetries that were measured (see Figure 5.2) and show a significant difference between the most offshore instrument (black line) and the nearshore located wave instruments, for both transects.

Looking at the eroding transect, it can be seen that the large difference in water depth between E1 and

the rest of the instruments can also be deduced from the spectral significant wave heights, presented in the middle plot. The wave heights at E1 are relatively large and follow a similar pattern as the offshore wave data, presented in Figure B.20. Along section A, most of the wave height attenuation seems to occur. In sections B and C, the wave heights lie close together and the pattern is similar. Finally, in section D the waves break on the steep shoreline, which can be concluded from the water depths and wave heights at E5. The large amount of wave height reduction in section A is not odd, since this section is more than three times longer than the other sections. However, given the bathymetry from Figure 5.2(a), it was not expected that such large differences in wave transformation occur since the bed profile in all sections is assumed linear and only losses due to bed friction were expected to occur.

In the accreting transect, most of the wave transformation also occurs in section A. However, for this transect, this can be well explained due to the presence of the chenier which is located around the red cross in Figure 5.2(b). A sudden change in the bathymetry causes that the waves suddenly enter a shallow area, which may cause depth-induced wave breaking (see Section 2.1). In contrast to the eroding transect, the wave heights keep changing significantly along the remaining of the accreting transect. Now it should be noted that the accreting transect is around 100 metres longer than the eroding transect, but it also contains more irregularities in the bathymetry profile. In section C, a small vegetation patch is present and section E and F lie inside the mangrove forest. The effect of vegetation on the hydrodynamics was already discussed in Section 2.3.2, and is applicable in this case. Furthermore, the water depth along the accreting transect is significantly lower than in the eroding transect, causing that bottom friction is more dominantly present and might explain the larger dissipation rates.

Various dissipation mechanisms might be occurring along the transects and therefore the transformation of wave heights is more thoroughly analysed in Sections 5.2.3 and 5.2.5.

In the lower sub-plots of Figure 5.3, the time series of the peak wave periods are presented. These graphs contain the measurements after filtering out the outliers, i.e. measurements with unrealistically high values. This makes a significant difference with the raw results of the observed wave periods, which are extremely noisy including wave periods of about 200 seconds (see Appendix B.8). These outliers are probably the result of measurements collected during low water levels when some instruments fall dry. Therefore the amount of outliers increase for instruments located closer to the shore, on higher ground.

For both the eroding and the accreting transect, it can be seen that the black dots, representing the wave peak periods at the most offshore wave instruments, show a clear trend line corresponding to the wave events that are shown in the middle graphs (higher waves come with longer wave periods). The peak period of incoming wave heights deviates around 6 seconds. For instruments closer to the shore, the amount of realistic measurement points decreases and the deviation increases. Therefore, from the graph, it can not be deduced accurately how the wave periods develop. During the calculations in the remaining of this chapter, mean values for the peak wave periods of the nearshore instruments (all colors instead the black) are used. Based on the mean values it can be seen that the wave period decreases towards the shore in both transects from around 6 seconds to around 4 seconds. It stands out that along the accreting transect the wave periods tend to increase in the vegetation sections C and E. This will be discussed further on.

5.2.3 Wave friction coefficient

The wave friction coefficient (f_w) (defined in Section 2.1) was calculated in order to analyse the dominant dissipation processes at both transects. The wave friction coefficient represents the amount of wave energy dissipation due to *bottom friction*.

By calculating the wave friction coefficient and comparing with values from the literature, it can be determined whether the observed energy dissipation is the result of bottom friction only, or whether additional dissipation processes are likely to occur such as wave breaking or interaction with vegetation. The calculations of the wave friction coefficient are described in Appendix G.2.2.

The wave friction coefficient was determined in sections located between two consecutive instruments, A to C in the eroding transect, and A to F in the accreting profile (see Figure 5.2). Five wave events were selected and used to calculate the friction factor at the sections, presented in Table 5.2. The events for which the wave friction coefficient is calculated are all occurring during high water (HW). It is important that all the wave instruments are submerged in order to prevent extremely large friction values. As mentioned in the last paragraph of Section 5.2.2, the wave periods for the most offshore wave logger were

relatively accurate. For the rest of the instruments, the peak wave period is estimated by calculating the mean values. The strong deviation is neglected by filtering out all the wave periods that exceed the wave period of the most offshore wave logger. It is thus assumed that the wave periods along the transect are *always* smaller than the wave period of the most offshore wave logger.

Table 5.2: Water depths and spectral wave parameters per wave instrument along the transects for various selected wave events: 1) 26/11/2017 01:07AM, 2) 27/11/2017 01:07AM, 3) 28/11/2017 00:22AM, 4) 29/11/2017 02:31AM, and 5) 01/12/2017 04:24AM.

	Eroding				**Accreting**			
Wave event	#	h [m]	H_{m0} [m]	T_p [s]	#	h [m]	H_{m0} [m]	T_p [s]
1	E1	1.59	0.497	5.8	A1	1.58	0.474	6.4
	E2	0.82	0.334	4.5	A2	0.45	0.248	5.5
	E3	0.73	0.280	4.2	A5	0.59	0.147	4.6
	E4	0.81	0.279	4	A6	0.49	0.14	5.1
	E5	0.28	0.174	4	A8	0.48	0.070	4.6
					A9	0.44	0.047	4.9
2	E1	1.51	0.778	7.7	A1	1.51	0.722	7.4
	E2	0.79	0.284	4.5	A2	0.42	0.260	5.5
	E3	0.7	0.248	4.2	A5	0.57	0.173	4.6
	E4	0.82	0.250	4	A6	0.48	0.142	5.1
	E5	0.27	0.165	4	A8	0.46	0.098	4.6
					A9	0.43	0.064	4.9
3	E1	1.49	0.696	7.2	A1	1.48	0.662	7.2
	E2	0.76	0.236	4.5	A2	0.38	0.215	5.5
	E3	0.67	0.213	4.2	A5	0.54	0.150	4.6
	E4	0.78	0.175	4	A6	0.42	0.118	5.1
	E5	0.24	0.08	4	A8	0.41	0.070	4.6
					A9	0.37	0.040	4.9
4	E1	1.57	0.286	6.4	A1	1.56	0.393	6.5
	E2	0.79	0.240	4.5	A2	0.42	0.237	5.5
	E3	0.7	0.206	4.2	A5	0.58	0.145	4.6
	E4	0.8	0.207	4	A6	0.47	0.133	5.1
	E5	0.25	0.130	4	A8	0.45	0.070	4.6
					A9	0.42	0.040	4.9
5	E1	1.99	0.970	6.7	A1	1.99	0.941	6.5
	E2	1.24	0.460	4.5	A2	0.86	0.456	5.5
	E3	1.16	0.430	4.2	A5	1.02	0.355	4.6
	E4	1.25	0.400	4	A6	0.91	0.261	5.1
	E5	0.69	0.345	4	A8	0.89	0.208	4.6
					A9	0.86	0.146	4.9

According to Lacy and MacVean (2016), the wave friction coefficients for mud flats lie between 0.02 and 0.1. So, here it is assumed that higher values than 0.1 indicate the presence of additional energy dissipation processes rather than bottom friction only.

The wave friction coefficients along the various transect sections for the selected wave events are presented in Table 5.3. The results are discussed in ascending order from section A to F.

For wave events 2, 3 and 5, a relatively large change in wave height occurs in Section A, which can be seen in Table 5.2. For events 1 and 4, this change is much less and can be related to the smaller incoming wave height. This can be found back in the wave friction coefficients as well. For the eroding transect, the wave friction coefficient in section A is around 0.16 during wave events 1 and 4. During events 2,3 and 5, f_w has increased to around 0.3. In the accreting transect, f_w for section A constantly lies around 0.3, indicating a difference in wave transformation between the transects. An f_w of 0.3 lies far beyond the maximum bottom friction value of 0.1 which means that bottom friction can not be the only energy dissipation mechanism. Looking at the relation between incoming wave height and amount of wave height attenuation, depth-induced wave breaking can be an occurring dissipation mechanism.

This can also be supported by the fact that the wave friction coefficient in section A of the shallower accreting transect lies constantly around 0.3, regardless of the incoming wave height. This is in contrast with the eroding transect, where the severe dissipation only seems to occur for an incoming wave height larger than a certain value. So, for large wave events, the wave friction coefficient for the eroding and accreting transect is equal for section A. Based on the bathymetry (the accreting transect has a chenier in section A while the eroding transect has not) this is not expected. This might indicate that section A of the eroding transect contains the lower part of the chenier, as was discussed in Section 3.3.3. The possibility of wave breaking in section A of the eroding transect is further investigated in Sections 5.2.4 and 5.2.5.

Table 5.3: Wave friction coefficients for sections between consecutive instruments during the selected wave events from Table 5.2

	Eroding		**Accreting**	
Wave event	Section	f_w	Section	f_w
1	A	**0.16**	A	**0.30**
	B	0.08	B	0.09
	C	0	C	0.04
	D	0.92	D	0.06
			E	0.64
			F	1.17
2	A	**0.29**	A	**0.28**
	B	0.07	B	0.05
	C	0	C	0.09
	D	0.92	D	0.01
			E	0.28
			F	1.00
3	A	**0.31**	A	**0.34**
	B	0.06	B	0.05
	C	0.1	C	**0.11**
	D	2.13	D	0.03
			E	0.39
			F	1.50
4	A	**0.16**	A	**0.30**
	B	0.09	B	0.08
	C	0	C	0.06
	D	1.18	D	0.06
			E	0.48
			F	1.80
5	A	**0.27**	A	**0.25**
	B	0.06	B	0.07
	C	0.05	C	**0.22**
	D	0.55	D	0
			E	0.47
			F	1.50

In section B, f_w lies for both transects between 0.05-0.09. It can be expected that no obstacles such as a chenier or vegetation are present in section B of the eroding transect, looking at the bathymetry. This seems to suggest that the wave energy dissipation in this section is only due to bottom friction. It must be noted though that this part of the eroding transect is rather sandy and therefore the friction coefficient approaches the upper threshold for muddy beds which lies at 0.1. In the accreting transect, section B lies between A2 and A5, where A2 is located at the seaward side of the chenier. Nevertheless, from the wave heights at this location, it seems like the chenier already initiated wave breaking before A2, indicating that the chenier might be extending more seaward. Despite this, it is clear that the first part of section B contains a large part of the chenier, which has a sandy texture and thus probably higher friction factors than mud. The wave friction coefficient in section B therefore lies between 0.05-0.09, similar to the eroding transect, where section B has a higher sand content. These friction coefficients

for sandy beds indicate that in this area, the friction coefficients for mud probably lie below 0.05.

In section C of the eroding transect, a sudden increase in water depth is visible which could correspond to the concave-up profile of eroding mangrove-mud coasts (see Section 2.3.1). Another possibility for this increased water depth is the presence of a channel. This possibility is clarified by Figure 3.6 in which it can be seen that the channel in the southeast bifurcates into two branches, one of which crosses both transects just in front of the shore. An increase in water depth means that the effect of bottom friction decreases. Therefore, hardly any dissipation occurs in this section resulting in wave friction coefficients that are lying close to zero.

Section C in the accreting transect comprises the vegetation patch, which is clearly visible in Figure 3.2. The wave friction coefficient in this section deviates a lot between various wave events. For large wave events, the friction coefficient is significantly larger than for lower wave events which coincides with the findings of Horstman et al. (2014). Since mangroves are more dense around the canopy, this part causes more friction and is probably only reached during high wave events. This is in contrast with the sections without vegetation. For these sections, large wave events are associated with lower wave friction coefficients.

During the low wave events 1 and 4, the value of f_w decreases to around 0.05. According to Lacy and MacVean (2016) this would mean that waves are only affected by bottom friction, while it is known that vegetation is present. Horstman et al. (2014) also found that for short waves, the interaction with vegetation causes an increase of the mean wave period. From Table 5.2 it can be seen that along the vegetation sections (C and E) the wave period indeed increases while it decreases in the other sections. This again supports the presence of vegetation in section C. Furthermore, it indicates once more that the wave friction coefficient for mud only lies below 0.05.

The wave friction coefficient along section D varies between 0-0.06 and is therefore the section along which the least amount of friction occurs. The largest friction values occur during the calm wave conditions of events 1 and 4, whereas during high wave energy events (2, 3 and 5) the friction coefficients are significantly smaller. The section is free from vegetation and the sediment grain size significantly decreases from 27 μm (A6) to 7 μm (A7). According to field observations this section is extremely muddy and relatively fluid towards the shore (BioManCo, 2018).

Section E and section F both contain vegetation, where section E is located at the edge of the forest and section F inside the forest. This difference can be seen looking the the wave friction coefficients along both sections.

At section E the waves are already affected by the young mangrove vegetation, resulting in friction coefficients between 0.30-0.65. Inside the forest, the friction increases and values between 1.0-1.8 are found. Although these sections are significantly shorter compared to the other section along the transect, the wave friction coefficients are much larger. Hydrodynamic drag from vegetation is the most dominant dissipation mechanism here. The large friction values indicate the severe influence of the mangrove vegetation on wave energy dissipation.

Most of the calculated wave friction coefficients in this section could be explained based on the system analysis from Chapter 3.1. Except for section A of the eroding transect where large dissipation rates are found which could not be explained based on either the system analysis nor the bathymetry profile. Therefore, the focus now lies on investigating the probability of depth-induced wave breaking in that particular section. For the accreting transect, the severe dissipation is expected to be the result of the chenier which induces wave breaking and therefore it is expected that a similar physical occurrence is present in the eroding transect, between E1 and E2.

5.2.4 Spectral wave analysis

In order to understand the large difference in dissipation rates for various incoming wave heights that were observed in section A of the eroding transect (between E1 and E2), a spectral analysis was carried out. To determine the probability that wave breaking occurs in section A, wave density spectra were plotted for two conditions, presented in Figures 5.4 and 5.5. The two conditions regarding the incoming wave height in the transect at E1, are: 1) $H_{m0} = 0.2 - 0.4$ m and 2) $H_{m0} > 0.4$ m. All the bursts for which the specific conditions are met are included in the spectrum.

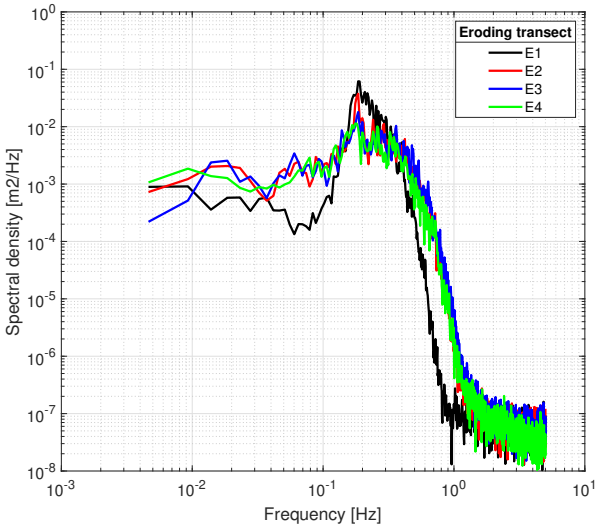

Figure 5.4: Spectral density for 0.2m < Hm0 < 0.4m at E1 in the eroding transect.

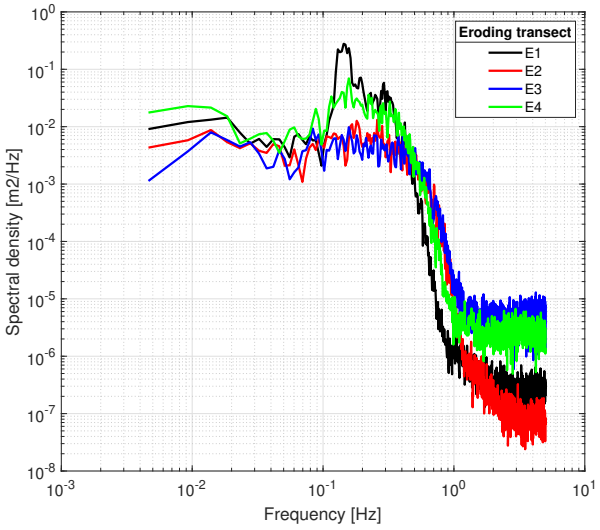

Figure 5.5: Spectral density for Hm0 > 0.4m at E1 in the eroding transect.

Figure 5.4 and Figure 5.5 show the energy distributions along various frequencies. In both cases the energy in low frequency waves dissipates towards the shore, whereas the energy in high frequency waves increases. This means that the energy that is transported by long waves distributes along short waves with a higher frequency.

It must be noted though, that the wave spectra are relatively inaccurate due to the noise in the observed wave periods. This is the reason that is seems like the low frequencies increase again after passing E3, as can be seen in Figure 5.5. This peak in the green line of E4 can thus be ignored.

By comparing both spectral density plots, the hypothesis of the occurrence of wave breaking in section A is strengthened. For H_{m0} lower than 0.4 m, the peaks in low frequency waves at the consecutive instruments lie close together, indicating a minimum amount of dissipation. For H_{m0} larger than 0.4 m, the low frequency peak at E1 significantly decreases towards E2, indicating a strong dissipation process. It is therefore likely that depth-induced wave breaking occurs between E1 and E2 for incoming wave heights of 0.4 m and higher.

5.2.5 Wave breaking

Theoretically, the occurrence of wave breaking should coincide with exceeding the wave breaking criteria, as defined by Miche (1944). An extensive description of these criteria is described in Appendix G.2.1. For very mild slopes, such as mud flats, the wave height over water depth ratio for which wave breaking is initiated (breaker index) lies around 0.6. The breaker index in de eroding transect reduces from 0.55 to 0.45 between E1 and E2, as can be seen in Figure 5.6. A breaker index of 0.55 seems to coincide with the expected value for a mild slope, i.e. $\gamma \approx 0.6$. Assuming that $\gamma = 0.55$ is the representative breaker index for this slope, it can be stated that the breaker index at E2 is too low.

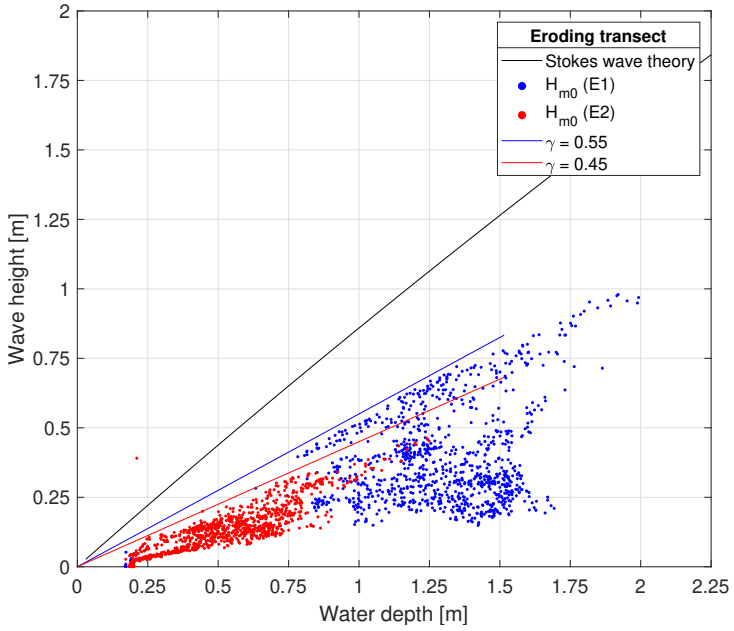

Figure 5.6: Wave breaking criteria according to Miche (1944) for incoming wave with a wave period of 6 seconds. Stokes wave theory reduces to $\gamma = 0.6 - 0.8$ for spilling breakers in shallow water. The waves measured by E1 show a threshold line for breaking around $\gamma = 0.55$. At E2 the breaking index has reduced to 0.45.

According to Equation G.2 and $\gamma = 0.55$, the wave heights found at E2 correspond to a water depth that is 10-20 cm lower than the water depth measured at E2. This indicates that between E1 and E2 a shallow area is present with a bed level around -0.4 m +MSL and -0.3 m +MSL, neglecting the effects of bottom friction and shoaling along this section.

The hypothesis of wave breaking in section A of the eroding transect might therefore imply that the bathymetry along this section is *not* linear in contrast to what has been assumed earlier. This is further explored in Section 5.3.

5.2.6 Bed level development

The results of the bed level measurements collected by the SED sensors are discussed in this section. The focus lies on relating the observed bed level changes to the wave-induced stresses that are exerted on that specific location. Based on the sediment composition in the area, it is expected that around the chenier (fine sand) a critical shear stress of 0.4-1.5 N/m^2 will be observed, while at the other locations (light sandy mud) this value lies between 0.15-0.25 N/m^2 (see Section 2.2.3). It should be noted that the observed bed levels are relative values based which depend on the location of sensors on the column of the SED instrument (see Appendix B.2). The shear stresses are calculated based on the data analysis results, which are average wave parameters over 15 minute intervals. The maximum shear stresses are therefore not considered here. Furthermore, at the locations that are covered with vegetation (E5, E6, A8, A9) the calculated shear stresses are likely overestimated since the hydraulic drag of the vegetation on the near bed flow velocity is excluded.

The red dots in the graphs represent the actual bed level measurements of the SED instrument. The quantity of measurement points depends, amongst others, on the measurement interval, emergence of the sensors (the SED only measures when the instrument is emerged) and light availability (no measurement during the night). This is further explained in Appendix B.2. A linear interpolation is applied in between the red dots.

The focus in this section lies on the measurement period of 25 November - 5 December 2017. The results of the long term bed level development are attached in Appendix B.8.1. The data processing is further explained in Appendix B.3.

The SED sensors in the eroding transect are deployed inside the mangrove forest, as can be seen in Figure

5.2(a) and 4.1(a). In this transect, the shoreline is characterised by a steep edge of dead brushwood (BioManCo, 2018). Since the wave heights at E5 (inside forest) are large compared to the water depth, high shear stresses can be expected.. The lower plot of Figure 5.7 shows that the shear stresses vary between 0.4-0.8 N/m^2 during HW. Due to this, the bed at E6 and E5 is gradually eroding up to 1.5 cm as can be seen in the upper plots of Figure 5.7. Right after the storm on 1 December, a sudden sedimentation peak occurs at E5 which tends to shelter this location from hydrodynamic forces afterwards, as can be seen from the shear stress that reduces to zero for HW events. Although E5 shows erosion on average, the bed level seems to be stable between 29 November and 1 December, where the shear stresses have decreased below 0.4 N/m^2. The bed even slightly accretes between 30 November and 1 December during shear stresses around 0.2 N/m^2. These observations seem to suggest that the threshold shear stress for erosion lies around 0.4 N/m^2. It should be noted that this location is situated inside the mangrove forest, in which the bed shear stresses can be expected to be much lower. Therefore, this critical shear stress is probably not representative for the soil at this location.

During the field campaign, it was observed that a chenier has developed inside the eroding transect, which was mentioned in Section 3.3.3. This would mean that during the winter period, the shoreline got more sheltered from wave energy. This can be seen in Figure B.27 which presents the long term bed level development at the shore edge, at E5. The bed is eroding significantly up to 24 December 2017, after which the bed suddenly increases slightly and then remains stable up to the end of January 2018. The sudden shift from erosion towards accretion seems to suggest that chenier development happens rather quickly. This will be discussed further on in this section. Additionally, Figure B.27 seems to show a correlation between offshore wave heights and bed level development that indicates that higher erosion rates occur during small waves, compared to large waves. This is in line with the theory of Winterwerp et al. (2013), stating that a large gradient in wave height is necessary for onshore sediment transport.

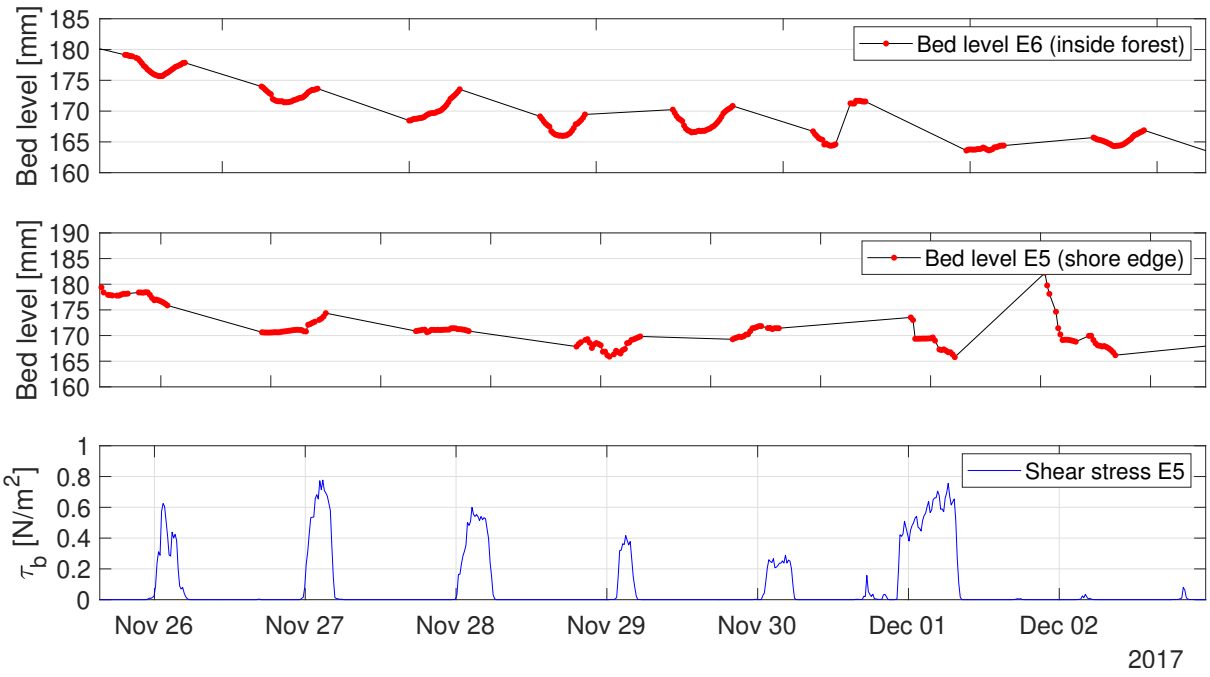

Figure 5.7: Bed level development in the eroding transect. Upper: E6 (inside forest), lower: E5 (forest edge). Note that the shear stresses are calculated for location E5 only.

Inside the mangrove forest in the accreting transect, at A9, an increase in bed level of around 3 cm is observed, which can be seen in Figure 5.8. Even on a slightly longer time scale, this location keeps accreting, despite the high energy wave events offshore, as can be seen in Figure B.26. This location is well sheltered by the vegetation inside the forest, resulting in wave heights around 5 cm during HW, which can be seen in Figure 5.3(b). As a result, the bed shear stresses remain on average well below 0.05 N/m^2, resulting in net accretion. During the 1 December storm, the shear stresses reach up to 0.1 N/m^2 due to which the bed slightly eroded. This indicates that the threshold shear stress for erosion lies between 0.05-0.1 N/m^2.

At the edge of the forest, at A8, the shear stresses are already significantly larger than at A9. On average, the bed shear stress varies between 0.05-0.1 N/m^2 due to which the bed level still seems to be stable, as can be seen at the period of 26 November - 30 November in Figure 5.9. During the 1 December storm event, the shear stresses exceed 0.15 N/m^2 and the bed erodes up to 2 cm. Beyond the storm, the shear stresses decrease to a maximum of 0.05 N/m^2 resulting in accretion again. This suggests that this location is less protected by vegetation than at A9 and therefore reacts actively to the offshore wave climate, as can be seen at the long term bed level development which exactly follows the trend of the offshore wave climate (see Figure B.28). During large wave events the bed level erodes, whereas during low wave events accretion occurs. Similar as at A9, the critical shear stress for erosion tends to lie between 0.05-0.1 N/m^2.

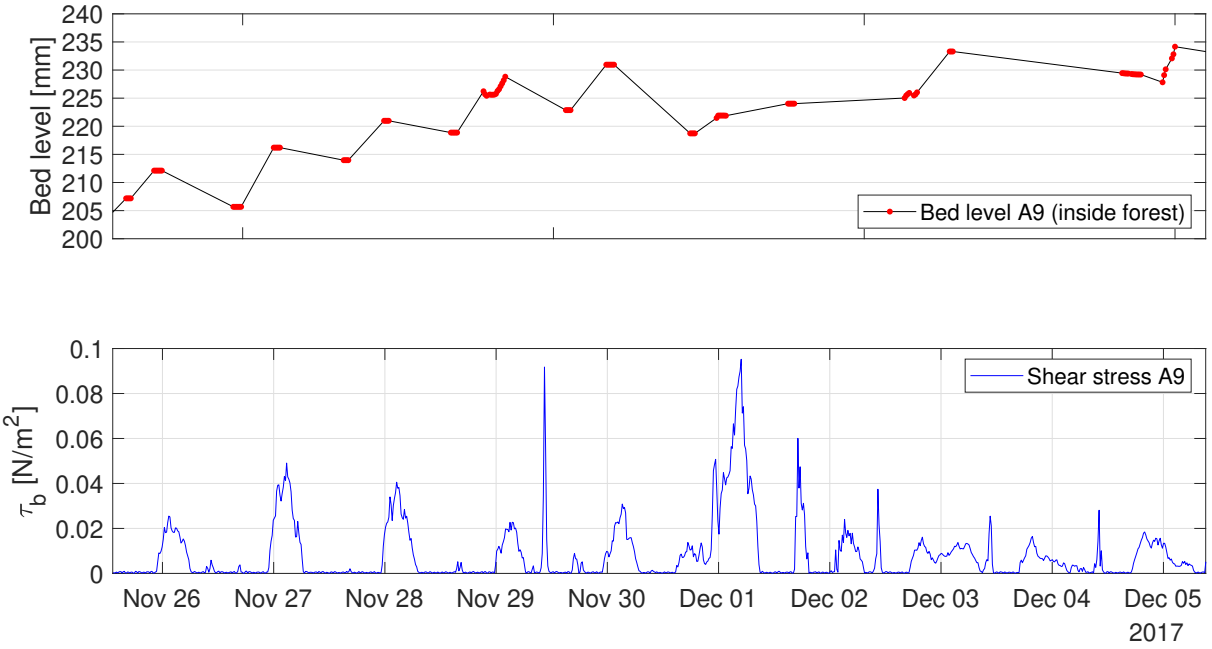

Figure 5.8: Bed level development and shear stresses in the accreting at A9 (inside forest).

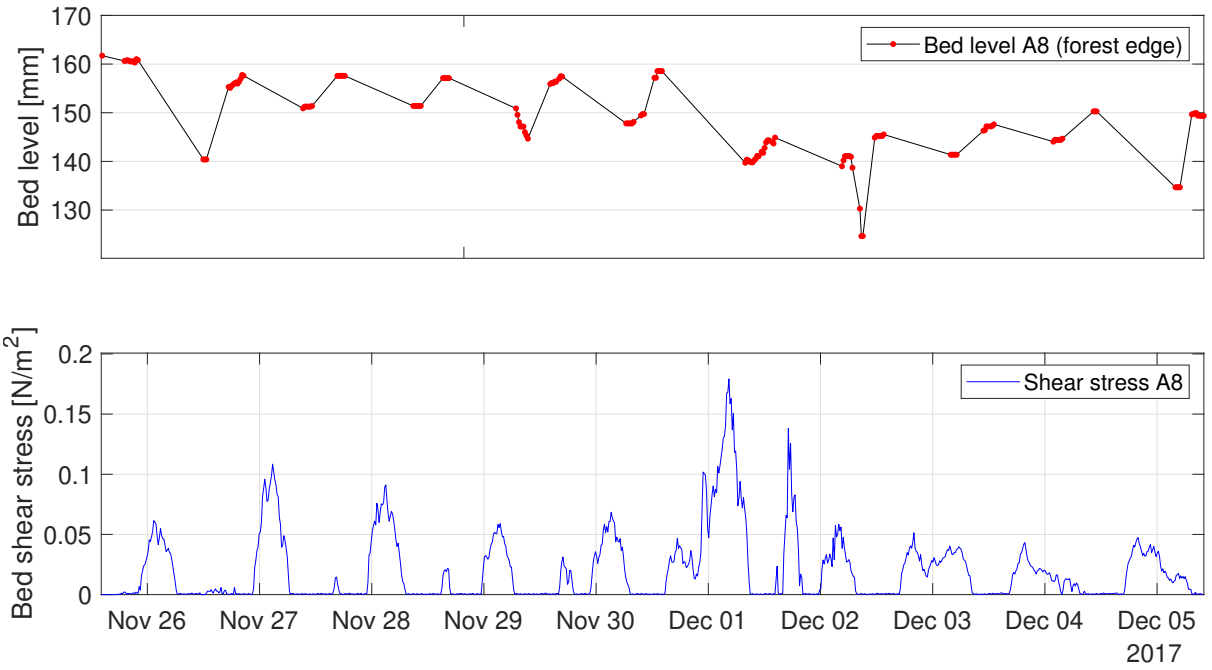

Figure 5.9: Bed level development and shear stresses in the accreting at A8 (forest edge).

The bed at A7 shows a highly dynamic behaviour as can be seen in Figure 5.10. On average, the shear stresses exceed 0.1 N/m^2, due to which dominantly erosion would be expected. However, between 27-29 November, the bed level increases with around 5 cm although the shear stresses exceed 0.15 N/m^2 at that period. Apparently, the shear stresses at A7 are low enough to allow mobilised sediment to settle which indicates that these are probably larger grain sizes. These larger grain sizes could be originated from locations around the vegetation patch, which is more sandy. During the storm event, this amount of sediment is eroded again, which can be related to the high shear stresses up to 0.3 N/m^2. After the storm event, the bed level decreases gradually (see Figure B.25). Due to the dynamic behaviour of this location, the critical shear stress for erosion is highly uncertain. Based on the measured grain size that is similar to the locations inside the forest the critical shear stress would be expected between 0.05-0.1 N/m^2. However, since the bed level is quite stable for average shear stresses around 0.1 N/m^2 it can be roughly assumed that the range lies between 0.05-0.15 N/m^2.

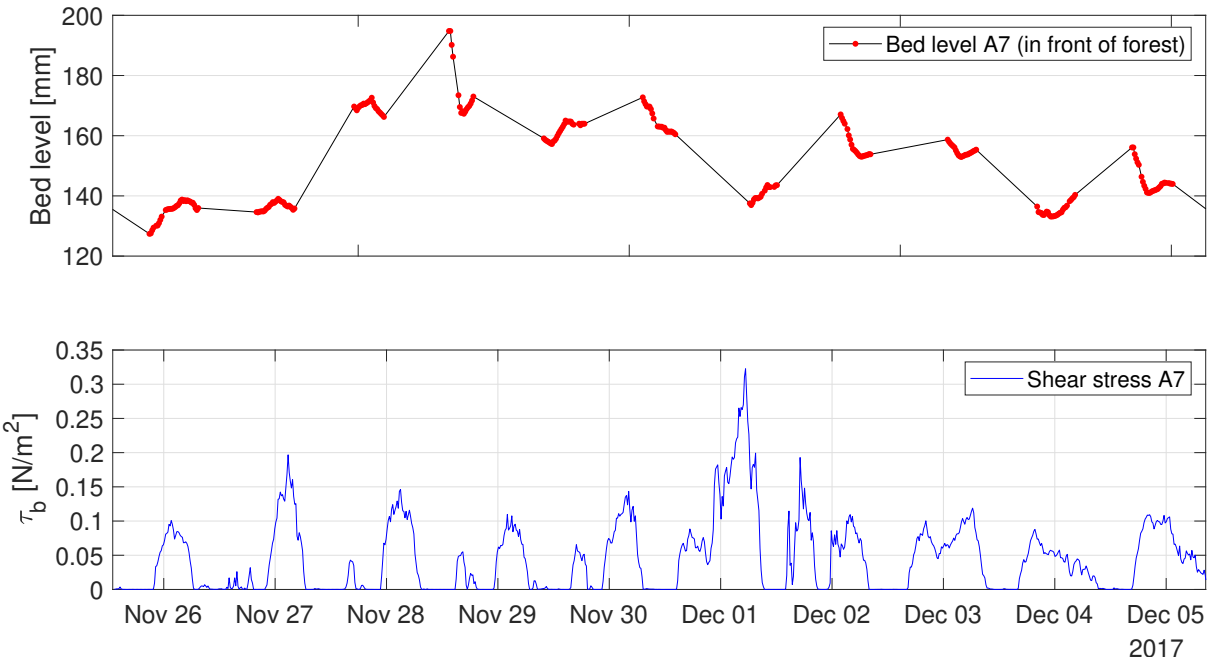

Figure 5.10: Bed level development and shear stresses in the accreting at A7 (forest edge).

During the first 5 days of deployment the bed shear stresses at A6 (behind the vegetation patch) deviate around 0.15 N/m^2 and therefore exceed the threshold for erosion significantly, as can be seen in Figure 5.11. The upper plot of Figure 5.11 shows that these shear stresses result in a considerable amount of erosion.

During the 1 December storm event, the bed level suddenly increased with 2 cm. Similar as at the locations of E5 (inside the forest in the eroding transect) and A7 (in front of the forest in the accreting transect), this occurred during a large wave energy event. A large gradient in shear stresses from offshore to nearshore could be the cause of this, as was discussed in Section 2.4. Since A6 is located right behind the vegetation patch, which is an old chenier, it is likely that sediment was mobilised at this chenier and deposited right behind it at A6. The shear stress gradient between A5 (in front of the vegetation patch) and A6 increases considerably during this large wave event, as can be seen in Figure 5.12. Already in Section 5.2.3 it was found that vegetation has a stronger influence on large waves than on small waves which in this case tends to result in sediment transport in nearshore direction. After 5 December 2017, the bed level at A6 remains constant throughout the whole month December, as can be seen in Figure B.29. The critical shear stress for bed erosion at this location is estimated between 0.1-0.15 N/m^2.

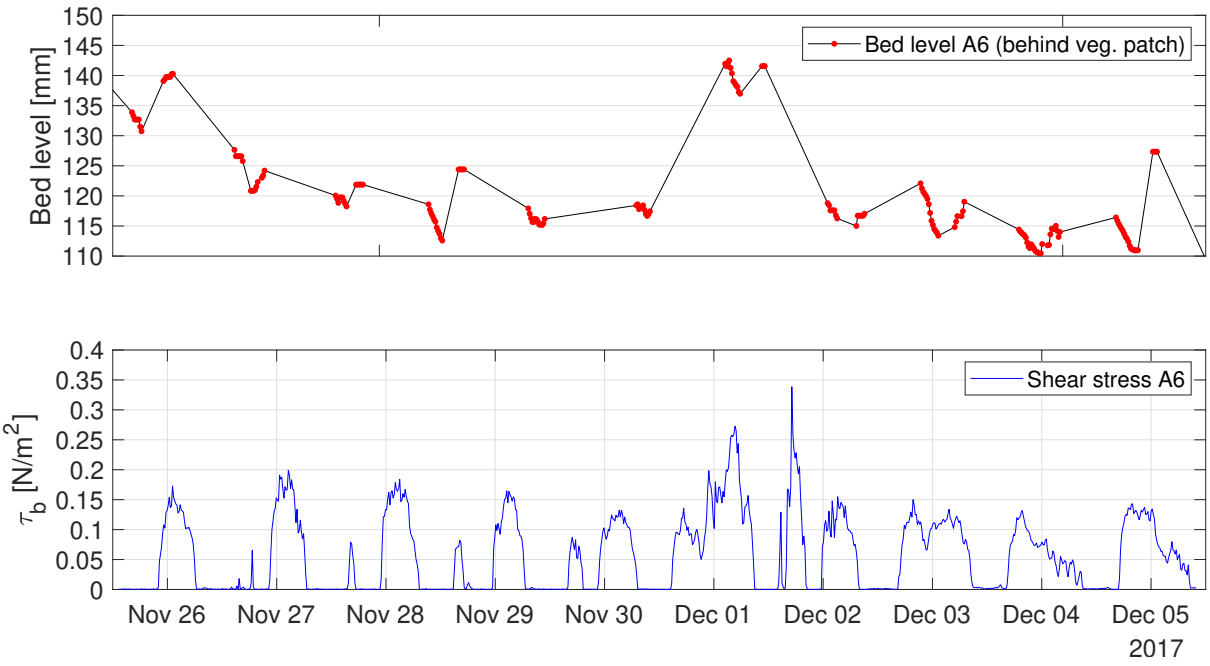

Figure 5.11: Bed level development and shear stresses in the accreting at A6 (behind vegetation patch).

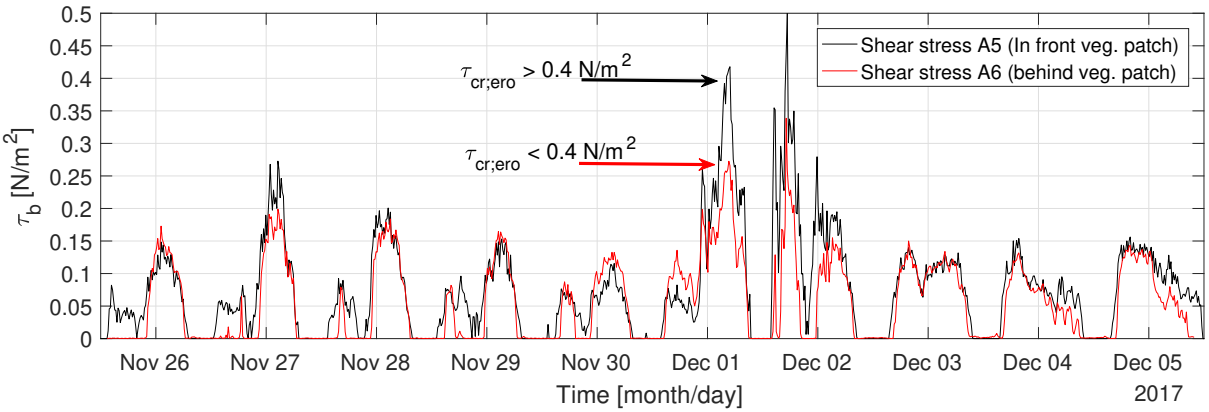

Figure 5.12: Comparison of bed shear stresses in front (A5) and behind (A6) the vegetation patch. Note the large gradient during the storm of 1 December.

Around the chenier, large variations occur during the *whole* winter period, as was observed by BioManCo (2018). Since the behaviour of cheniers is important to understand in this area, these locations are studied in more detail and only the long term plots are presented here, in Figure 5.13. The locations around the chenier are SED sensors 180, 181, and 179 (i.e. A2, A3, and A4 from offshore to nearshore, see Figure 5.2(b)). Upon retrieval these three instruments seemed to have suffered from complications which arose during the measurement period.

After a reliability analysis it was concluded that the bed level data of A4 and A2 is reliable until half December and for A3 it is not certain whether it was moved or not during the measurement period. The reliability analysis is described extensively in Appendix B.5.1 and B.5.2.

A2 was deployed at the seaward side of the chenier. The bed level change at this location is presented in the upper plot of Figure 5.13. A significant amount of erosion (+/- 15 cm) can be observed from the moment of deployment until around 15 December. The same amount of erosion is detected on top of the chenier, at A3. At the landward side of the chenier, at A4, a significant amount of sedimentation occurs during the same period, as can be seen in the third plot of Figure 5.13. This suggest that sediment is eroded from the front and top of the chenier and deposited in the sheltered area behind it. This is supported by the bed shear stresses that are exerted on the three locations around the chenier which

are presented in Figure 5.14. During HW, the exerted bed shear stresses in front of the chenier (A2) have values between 1.00-1.25 N/m^2 which is far above the erosion threshold for the fine sand at the chenier that lies around 0.4 N/m^2 (see Section 2.2.3). On top of the chenier (A3) the shear stresses are already considerably lower, deviating between 0.50-0.75 N/m^2, due to which still erosion can be expected. Beyond the chenier (at A4) the shear stresses decrease drastically towards around 0.25 N/m^2, allowing for deposition of the sand particles.

Around 15 December, the bed level at A2 and A3 seems to increase suddenly, similarly as the sedimentation pattern at A4 at the end of November. At A2, this is not a bed level change but a result of physical complications as was concluded from an analysis of raw voltage measurements (see Appendix B.5.2. However, at A3, the observations do point to a severe sedimentation event although it is yet uncertain whether A3 was moved during this period or not. Assuming that A3 was not moved yet, the similarity with the sedimentation event of A4 shows that such fast sedimentation rates are likely to occur and seem to suggest cross-shore movement.

Looking at the offshore wave climate, presented in the lower plot of Figure 5.13, the sedimentation event at A3 seems to coincide with the start of a series of high wave energy events, indicating the positive correlation between chenier movement (or chenier development) and wave energy.

The observations around the chenier indicate that for relatively normal wave heights there is erosion on the outer side of the chenier and accretion on the inner side, which might point to cross-shore movement of the chenier. Sufficiently large wave events tend to make to whole chenier grow by transporting sediment from offshore. However, the storm of 1 December did not induce accretion on the chenier which might indicate that a storm needs a certain duration. Another suggestion for this could be that there is a threshold wave height beyond which the shear stresses are too high to allow for deposition.

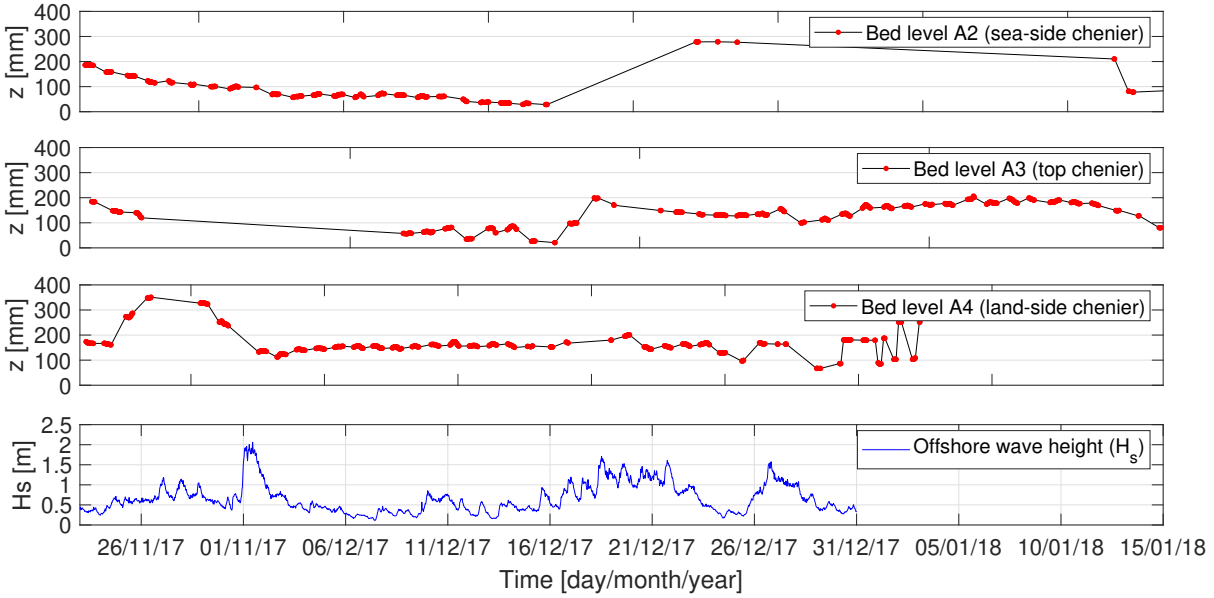

Figure 5.13: Bed level development around the chenier in the accreting transect. From up to down: A2 (sea-side chenier), A3 (top of chenier), A4 (land-side chenier). The lower plot presents the spectral significant wave heights collected by the offshore wave buoy. Note that the measuring duration of all instruments differs. For completeness, the x-scale is adapted to the longest measurement period.

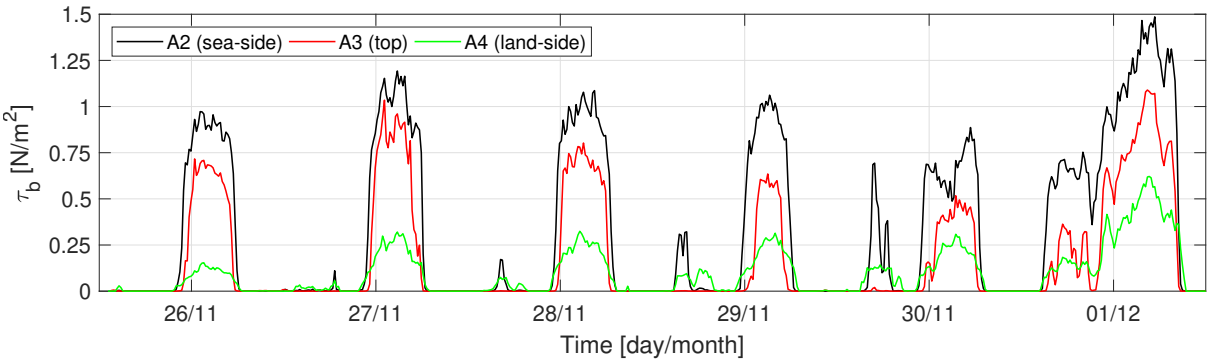

Figure 5.14: Wave-induced bed shear stresses at A2 (sea-side chenier), A3 (top of chenier) and A4 (land-side chenier) for the period 26 November - 1 December. Note that a Manning coefficient of 0.015 has been used here (fine sand).

The threshold shear stress for bed erosion ($\tau_{cr;ero}$) slightly deviates along the accreting transect, as can be seen in Figure 5.15. The largest values for $\tau_{cr;ero}$ occur around the chenier ($\tau_{cr;ero} \approx 0.4$ N/m^2), which is relatively sandy. Closer to the shore, where smaller grain sizes occur, that value tends to decrease towards 0.05 N/m^2 whereas at A6, a more sandy location, the threshold tends to lie more towards 0.15 N/m^2.

Seedlings have been found to establish between the vegetation patch and the mangrove forest in the accreting transect (BioManCo, 2018) before the winter measurement period. Furthermore, the bed level at A6 (behind the vegetation patch) and A7 (in front of the mangrove forest) remains relatively stable along the measurement period. Based on this, the locations A6 and A7 will be further investigated on possibilities for Windows of Opportunity in Section 5.3.

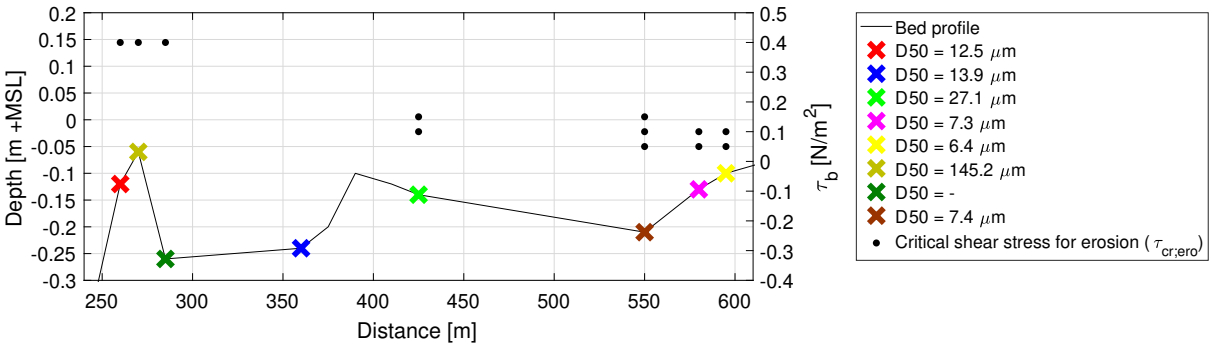

Figure 5.15: Critical erosion for sediment mobilisation along the accreting transect. The shore is located on the right side of the figure. Multiple values for $\tau_{cr;ero}$ on a location indicate the range of values that have been found here.

5.3 Modelling

This section describes the results of the modelling part of this research. First, the model is used to identify WoO for the conditions that actually occurred during the winter period. Then, the influence of the chenier and vegetation patch on shear stresses along the accreting transect is examined and the possible effect of a developing chenier in the eroding transect is discussed. Lastly, an attempt is made to find an indication of vegetation strength growth rates which must be met by mangrove seedlings in order to be able to establish on cheniers, as was found to occur by BioManCo (2018).

5.3.1 Identifying Windows of Opportunity

For the locations of A7 (in front of mangrove forest) and A6 (behind vegetation patch), a time series of bed shear stresses is computed for the time period 19 November 2017 - 31 December 2017. It is desired to explore the Windows of Opportunity that occur within this period by means of the threshold conditions for mangrove establishment defined by Balke et al. (2011) and Equation 2.12.

It should be noted that the bed shear stresses for determining Windows of Opportunity are calculated by means of the root-mean-square wave height (H_{rms}), whereas during the data analysis the spectral significant wave height (H_{m0}) was used. Eventually, calculating with H_{rms} results in higher maximum shear stresses since the largest waves have a higher weight factor. Since a seedling can be washed away by a single large wave, this method is more beneficial in order to determine possibilities for mangrove establishment. Furthermore, the model calculations include current-induced bed shear stresses as well.

When the bed shear stresses of the model are compared to the bed shear stresses from the data analysis, the same methods should be used. In these cases, the modelled bed shear stresses are converted to the same format as used in the data analysis, i.e. calculating with H_{m0} and an output interval of 15 minutes.

First, the model results for the actual situation are discussed. This is the model that is validated based on the data analysis results. Further on, model scenarios are discussed in which the influence of the chenier and the vegetation patch in the transect are tested. Finally, model results of the eroding transect are presented, in which the possibilities for accretion of the currently eroding shoreline - due to the development of the chenier - are discussed.

5.3.1.1 Actual situation (November-December 2017)

Figure 5.16 presents the bed shear stresses at locations A7 and A6 in the first and the second plot, respectively. During HW events, the shear stress at A7 is on average 0.05 N/m^2 and the maximum detected shear stress is 0.38 N/m^2. Further offshore, at A6, these values are slightly larger with an average of 0.08 N/m^2 and a maximum of 0.58 N/m^2. The periods of low bed shear stresses are accompanied by low energy waves offshore and spring-tide, as can be seen in the lower two plots of Figure 5.16. The water levels during HW are then relatively high and the waves relatively low, which results in small shear stresses.

Within the modelled time period, the longest inundation-free period takes around 14.5 hours and occurs on 21 November 2017. This is much shorter then the, by Balke et al. (2011) defined, required inundation-free period of 5 days. Even at the highest situated location in the accreting transect, the longest inundation-free period does not exceed 16 hours. Nevertheless, as mentioned in Section 3.3.2, mangrove colonisation has been found to occur in this area, meaning that the required inundation-free period must be shorter here. However, it should be noted that the average water level throughout the north-west monsoon is approximately 10 cm higher than throughout the south-east monsoon (BioManCo, 2018). This means that throughout the south-east monsoon, the dry periods are likely much longer. This will be further discussed in Chapter 6.

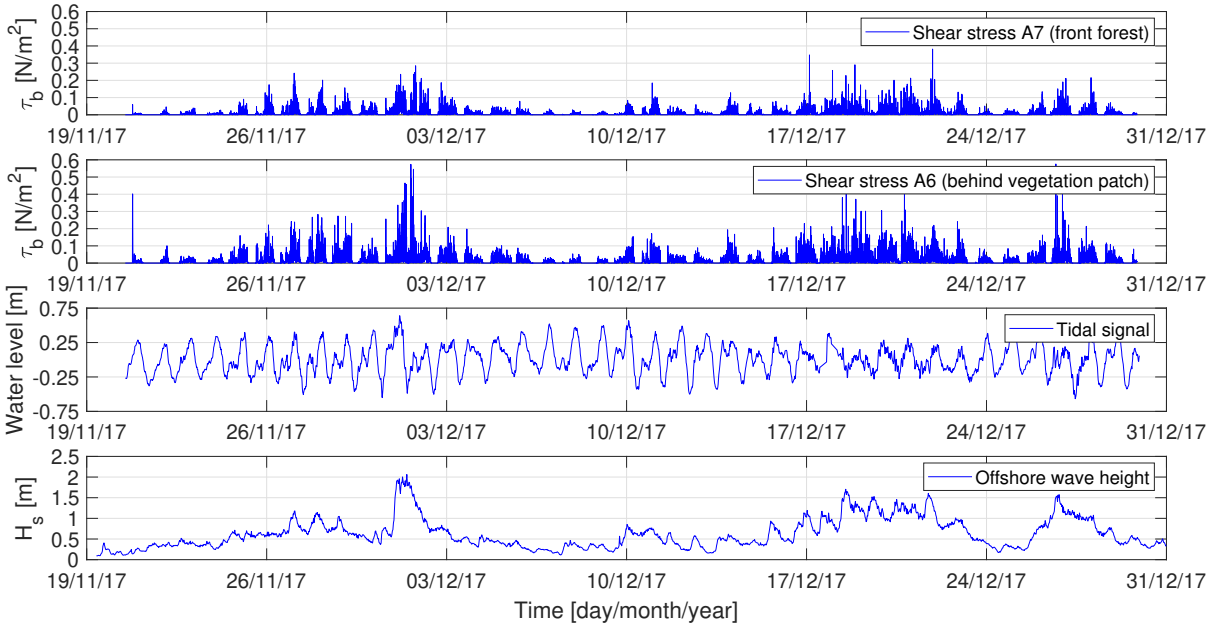

Figure 5.16: Wave- and current induced bed shear stresses at A7 (in front of forest) and A6 (behind vegetation patch). The third and fourth plot present the tidal signal and offshore wave climate, respectively.

Under the assumption that the inundation-free period on 21 November 2017 is long enough to prevent pioneer mangrove seedlings from floating up, a qualitative analysis can be carried out about the required period of low bed shear stresses that follows up the inundation-free period and about sensitive parameters that determine the feasibility of this low energy period. Equation 2.12 contains two essential parameters that determine the possibility for WoO: the critical bed shear stress for sediment mobilisation ($\tau_{cr;ero}$) and the growth rate of the vegetation strength (k).

Based on the bed level analysis in Section 5.2.6, the value for $\tau_{cr;ero}$ can initially be set at 0.1 N/m^2 and the value for k is set at 3.3e^{-3} Pa/hour (Balke et al., 2011). This is referred to as the 'ideal situation'. Due to the uncertainty of both parameters, their influence on the Windows of Opportunity at both locations is tested by means of an extra scenario in which k equals the minimum value that was found from the flume experiment of Balke et al. (2011), 1.2e^{-3} Pa/h. This is combined with a changed value for $\tau_{cr;ero}$ which is based on the findings in Section 5.2.6. For A7, $\tau_{cr;ero} = 0.05$ and for A6, $\tau_{cr;ero} = 0.15$.

The Windows of Opportunity after the inundation-free period on 21 November 2017 for A7 and A6 are presented in Figure 5.17. For seedling establishment, the vegetation strength curves should not be intersected by the occurring bed shear stresses.

At A7, the ideal situation and the situation with an ideal k value and minimum $\tau_{cr;ero}$ value will both result in seedling establishment, as can be seen in the right plot of Figure 5.17. A minimum k value seems to result in a vegetation strength that is just enough to survive the large shear stresses on 27 November. In the case that this minimum k value is combined with very easily erodible bed material ($\tau_{cr;ero} = 0.05$) the shear stresses at 26 and 27 November are sufficiently large to dislodge the seedlings.

At A6, the possibilities for seedling establishment considerably decrease for a deviating scenario from the ideal situation. For a minimum k value only, the large wave events on 27 November will dislodge the seedlings, as can be seen in the right plot of Figure 5.17. In the case that $\tau_{cr;ero}$ is increased to 0.15 N/m^2 the possibility of dislodgement decreases significantly.

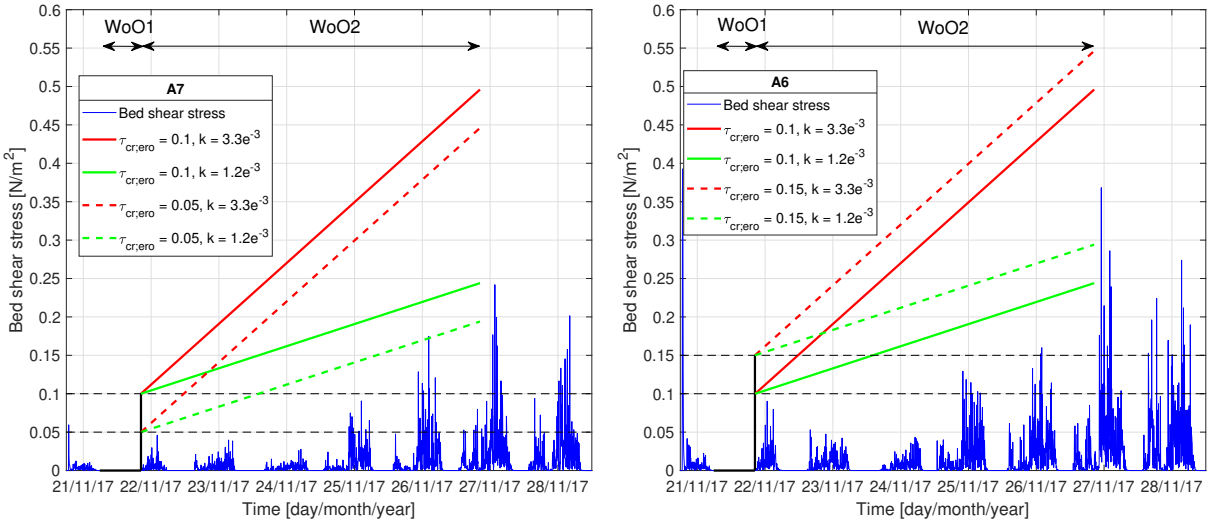

Figure 5.17: Windows of Opportunity at A7 (left) and A6 (right), based on wave- and current induced bed shear stresses. WoO1 represents an inundation-free period on 21 November 2017. WoO2 is represented by the growth curves of the vegetation strength which depend on the varied parameters k and $\tau_{cr;ero}$. The red lines present the situations at which $k = 3.3e^{-3}$ Pa/h, at the green lines $k = 1.2e^{-3}$ Pa/h. The black dashed lines represent the considered values for the critical shear stress for sediment mobilisation.

5.3.1.2 The influence of the chenier and the vegetation patch on shear stresses along the transect

In this section the influence of the chenier and the vegetation patch on the shear stresses along the accreting transect are explored. This is done by means of three scenarios. The original case represents the actual situation, with chenier and vegetation patch. In the other two scenarios, either the chenier *or* the vegetation is removed. The results of an additional case, without any protection at all, is presented in Appendix C.4 and are not elaborated on here.

The shear stresses are calculated based on H_{m0} and are averaged over a time interval of 15 minutes. This way, the presented shear stresses can be compared to the results of the bed level analysis in Section 5.2.6 to determine whether a location will have an eroding or an accreting character.

The influence of the chenier on the shear stresses along the transect is larger than the influence of the vegetation patch, as can be seen in Figure 5.18. At A7, the absence of the chenier causes that the shear stresses during HW increase from 0.1 N/m^2 to around 0.2 N/m^2. At A6 the shear stresses increase from 0.15 N/m^2 to around 0.3 N/m^2.

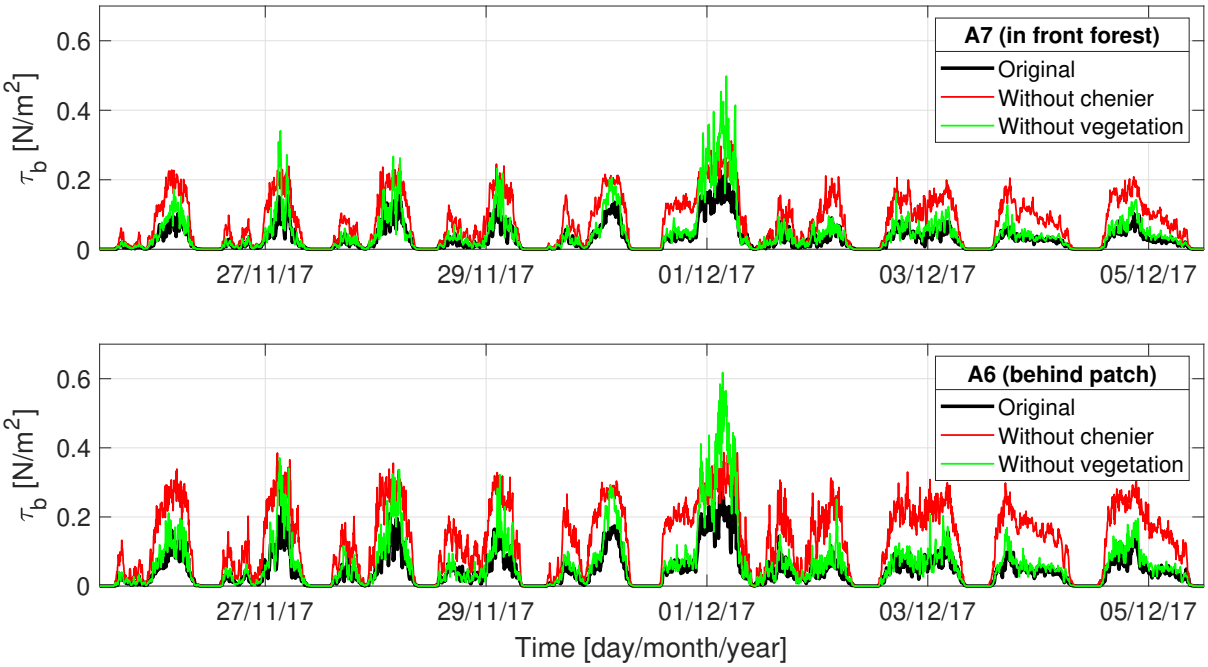

Figure 5.18: Wave-induced bed shear stresses at A7 (upper) and A6 (lower). Distinction is made between the three scenarios: 1) original case, 2) without chenier, and 3) without vegetation. The shear stresses are calculated with H_{m0} and averaged over a time interval of 15 minutes.

Similar as during the wave analysis in Section 5.2.3, it can be seen in both plots of Figure 5.18 that the vegetation especially affects the largest waves and not so much the small waves. During the high energy wave events of 27 November, 28 November and 1 December, the scenario without vegetation results in similar or even larger shear stresses than the scenario without a chenier. However, after the 1 December storm the wave conditions get calmer and the effect of the vegetation largely decreases.

Figure 5.18 also clearly shows that the black line, representing the original case scenario, deviates around the erosion threshold of 0.1 N/m^2, as was also shown in Section 5.2.6 for these locations. With the absence of either the chenier or the vegetation patch this threshold is exceeded considerably. For the vegetation scenario this is especially the case during high wave energy events before 2 December. These observations seem to suggest that both the chenier and the vegetation patch are essential parts in order to maintain the accreting character of this shoreline. The chenier seems to be a more continuous defence, since without the chenier, even the lower waves produce twice as large shear stresses.

The development of the shear stresses for the considered scenarios already indicate that the possibilities for WoO significantly decrease at both locations when either the chenier or the vegetation patch is gone.

The number of periods with low bed shear stresses decrease considerably, which can be seen in Figure 5.19 where the wave- and current induced bed shear stresses at A7 for the various scenarios are presented. In order to highlight the periods during which WoO are the most likely to occur, the red lines represent the periods with a length of at least three days in which the shear stresses do not exceed 0.1 N/m^2. The chenier has the largest effect on the length of these periods, as can be seen in the middle plot of Figure 5.19. In this plot it can also again be seen that the vegetation patch effectively attenuates especially large waves, resulting in lower shear stresses during the storm events compared to the situation without vegetation and with chenier as presented in the lower plot of Figure 5.19.

At A6, the duration of the periods with low shear stresses decreased well below the three days for both scenarios. This already indicates that WoO are not likely to occur when either the chenier or the vegetation patch is taken away.

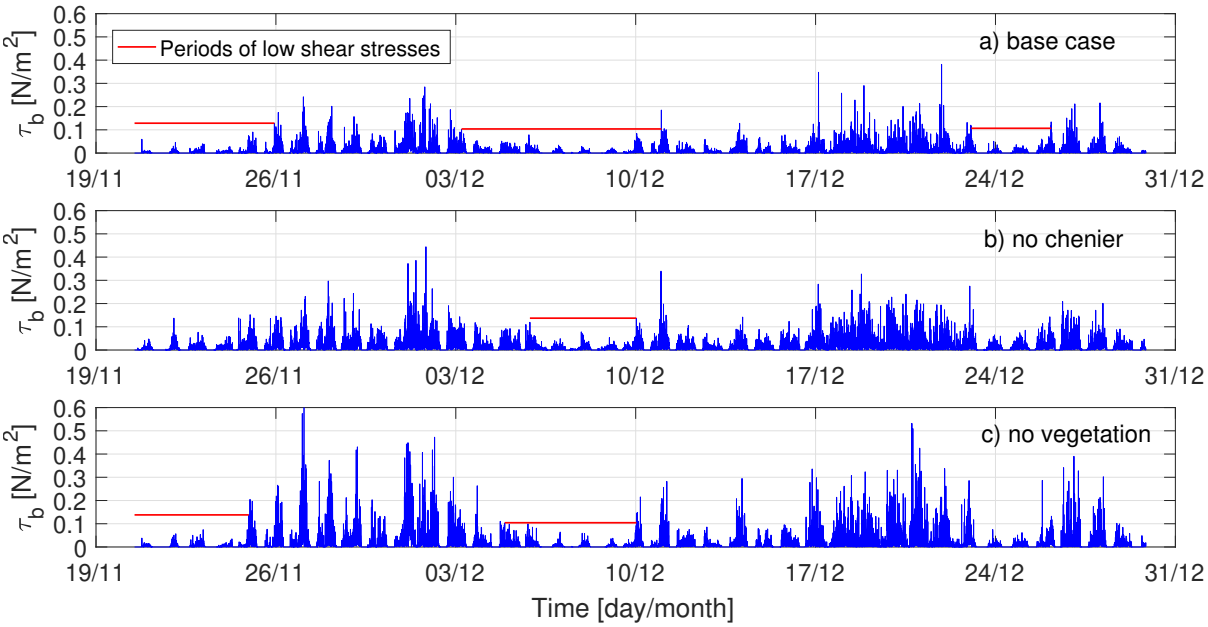

Figure 5.19: Periods of wave- and current induced bed shear stresses below 0.1 N/m^2 of at least 3 days at A7 for various scenarios. Upper: Base case; 5.4 days, 7.8 days, 3.1 days. Middle: Without chenier; 4.1 days. Lower: Without vegetation patch; 4.4 days, 5.1 days.

To validate this hypothesis, the probability for WoO at A7 and A6 is tested for the scenario without chenier, because this scenario has a larger influence on the bed shear stresses. Similar as in Section 5.3.1.1 the situation on 21 November 2017 is examined. It should be noted that the length of the inundation-free period differs from the original scenario because of the 1-dimensional flow in the model. During rising tide, the chenier prevents that the area between the chenier and the shore is flooding until the water exceeds the bed level of the top of the chenier. Therefore, in the situation without a chenier, the inundation-free periods are significantly lower.

At A7, the high shear stress just after the inundation-free period probably already rips out the anchored seedlings, looking at the left plot of Figure 5.20. Despite this event, the scenarios with an ideal growth rate (indicated by the red lines) indicate large possibilities for establishment.

Without a chenier, the shear stresses at A6 become so large that identifying WoO seems impossible, as can be seen in the right plot of Figure 5.20. In any scenario, the shear stresses on 27 November are too large for seedlings to establish.

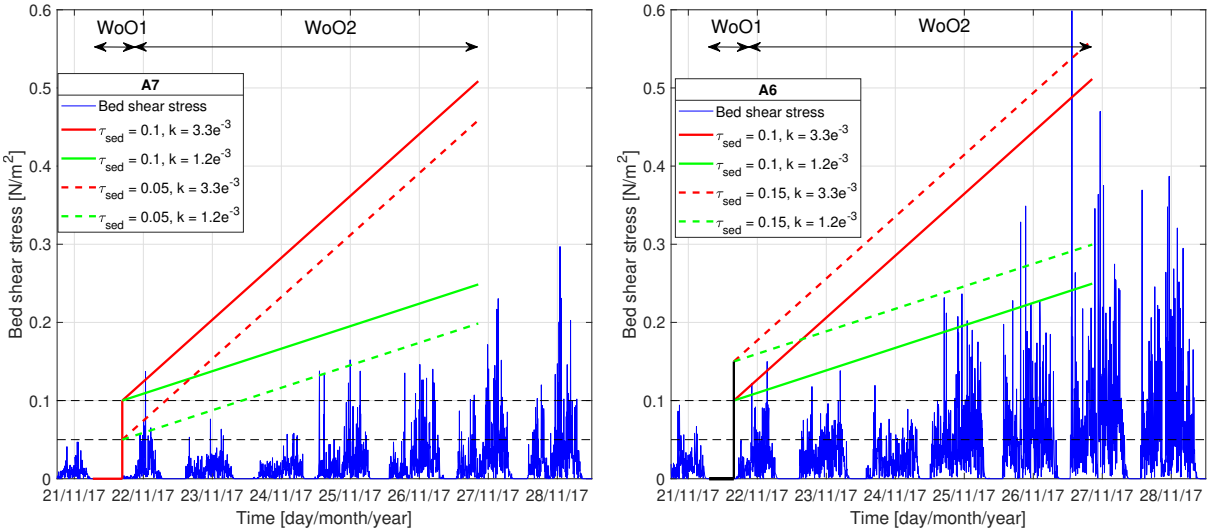

Figure 5.20: Windows of Opportunity at A7 (left) and A6 (right), based on wave- and current induced bed shear stresses. WoO1 represents an inundation-free period on 21 November 2017. WoO2 is represented by the growth curves of the vegetation strength which depend on the varied parameters k and $\tau_{cr;ero}$. The black dashed lines represent the considered values for the critical shear stress for sediment mobilisation.

5.3.2 The effect of a developing chenier in the eroding transect

The results of the bed level analysis in Section 5.2.6 showed that the bed inside the mangrove forest in the eroding transect is gradually eroding. It was also observed that this erosion rate decreased along the winter period, and the bed level remained stable after 24 December 2017. This is likely the result of the developing chenier in the eroding transect that was observed by BioManCo (2018). In this section, the effect of a developing chenier in the eroding transect is analysed by means of three modelling scenarios that are presented in Figure 4.7. The base case scenario represents the actual situation and is validated by means of the data analysis (see Section 4.2.4). In the base case the bed level of the top of the chenier is located at -0.3 m +MSL. In the second and third scenario, the bed level of the chenier is raised up to -0.15 m +MSL and 0 m +MSL, respectively. The results of an additional situation, without chenier, are presented in Appendix C.4 and are not elaborated on here. The occurring bed shear stresses around the shoreline are compared with the threshold shear stresses for bed erosion, as found in Section 5.2.6, in order to determine when the reversal from an eroding shoreline to an accreting shoreline occurs. As mentioned, the focus lies on the locations around the shoreline. Therefore the locations of E5 and E4 are analysed in this section. E4 is located right in front of the shoreline. This is an essential spot, since the behaviour of the bed level at this location can largely influence the erosion of the shoreline. With accretion, the wave heights will eventually become lower, whereas with erosion, the wave heights will increase more initiating a positive feedback effect (Winterwerp et al., 2013). E5 is located at the forest edge, on top of the brushwood cliff.

For the base case scenario, the bed shear stress at E4 fluctuates around 0.2 N/m^2 during HW events whereas at E5, the shear stresses deviate around 0.5 N/m^2. The latter was also found in Section 5.2.6 where it can be seen that these bed shear stresses result in erosion. Since an average shear stress of 0.5 N/m^2 only results in gradual erosion, it can be expected that a minor shift can already result in accretion.

At E5, the chenier height especially affects the occurring bed shear stresses during high energy wave events, as can be seen in the upper plot of Figure 5.21. Between 26 November - 30 November, the average HW shear stresses decrease from 0.50 N/m^2 to around 0.25 N/m^2. After 1 December, the shear stresses were already around 0.3 N/m^2 and decrease only slightly for larger chenier heights. An average HW bed shear stress of 0.2 N/m^2 is much lower than the initial shear stress of 0.5 N/m^2 and will probably result in accretion within this vegetated location, based on the critical shear stress for erosion of 0.4 N/m^2 that was found in Section 5.2.6. Note that this value is much lower in reality, since the effect of vegetation on the bed shear stresses is not taken into account.

At the un-vegetated location of E4, a critical shear stress of around 0.1 N/m^2 is expected based on the $\tau_{cr;ero}$ values that were found for light sandy mud sediments in Section 5.2.6. At E4, the average HW bed shear stresses in the initial situation reduce from 0.20 N/m^2 to 0.05 N/m^2 when the top of the chenier is located at MSL. For the scenario in between, with the chenier at -0.15 m +MSL, the shear stresses have already decreased significantly to 0.10-0.15 N/m^2. The latter is not enough for accretion of the bed level, but when the chenier has grown towards MSL the shear stresses decrease well beyond the critical shear stress for erosion of 0.1 N/m^2. Therefore, when the chenier is situated around MSL, it can be expected that the bed at E4 eventually starts accreting.

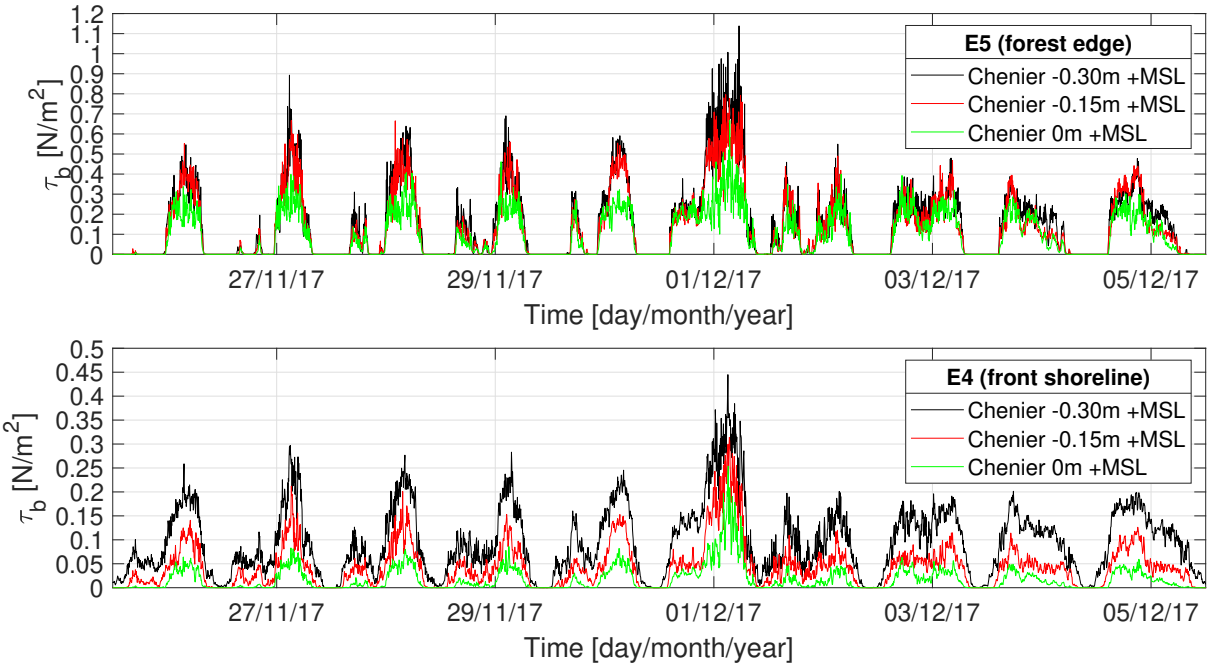

Figure 5.21: Wave-induced bed shear stresses at locations E5 (upper) and E4 (lower) for various scenarios.

Both E4 and E5 are probably not suitable for mangrove establishment, looking at how the locations are situated. E4 is situated at -0.5 m +MSL which seems to be too low for sufficiently long emergence periods. E5 is situated right beyond the cliff of brushwood at which waves break and is consequently subject to high shear stresses most of the time. A potential location for mangrove establishment in the eroding transect might be the new developing chenier, which is further discussed in Section 5.3.3.

5.3.3 Exploring conditions for seedling establishment on the inner side of a developing chenier

In Section 3.3.2 it was mentioned that during the winter period, seedlings have been found to establish on a chenier that has developed during the winter period in front of the coast of Timbul Sloko, just south the accreting transect (BioManCo, 2018). In this section, an attempt is made to determine the conditions that these seedlings must have survived in order to establish. This way, an indication can be acquired about the required growth rate of the vegetation. The considered location for seedling establishment is the inner side of the chenier, as presented in Figure 4.7. Note that for each scenario, the bed level of the considered location changes as well, which influences the bed shear stress. However, this is necessary since more opportunities for seedling establishment occur when the bed level is higher. Furthermore, it should be noted that, although a chenier in the eroding transect is selected, this analysis aims on the possibility of mangrove establishment on cheniers *in general*, so it does not imply colonisation in the eroding transect in particular.

In Figure 5.22 the development of the bed shear stresses at the inner side of the chenier for the various scenarios can be observed. The shear stresses decrease significantly from an average around 0.6-0.8 N/m^2 in the base case scenario, to around 0.2 N/m^2 for a chenier height at MSL. The chenier height thus positively influences the decrease of shear stresses, although the bed level at the considered location raises. In Section 5.2.6 it was found that erosion on the chenier occurs from bed shear stresses around 0.4 N/m^2, indicating that a chenier with a bed level at -0.15m +MSL should already offer possibilities for seedling establishment in terms of shear stresses.

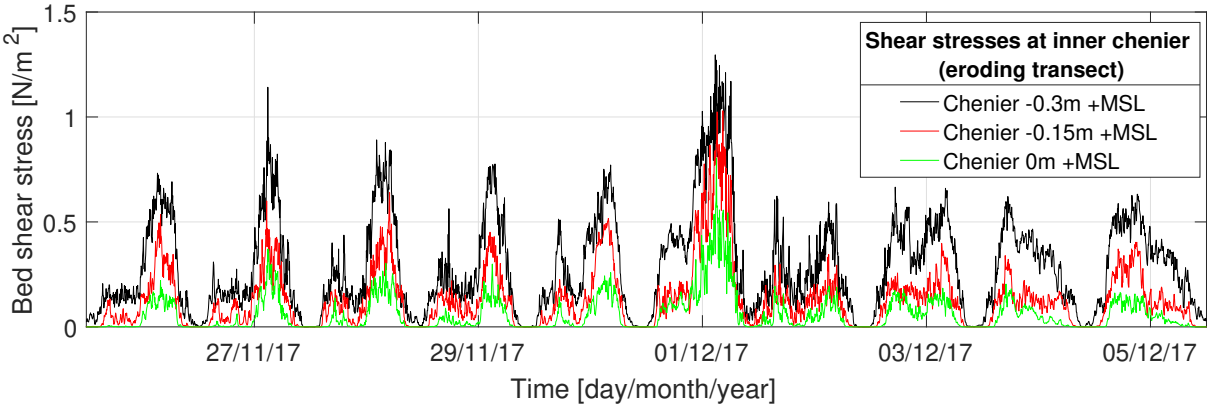

Figure 5.22: Wave-induced bed shear stresses at the inner side of the chenier in the eroding transect for various scenarios.

Since there is no validation available about the required chenier size to enhance seedling establishment, it is assumed that a chenier with a bed level at MSL suffices to allow for establishment at the chenier. This is assumed, based on observations of seedling establishment on cheniers with a bed level around MSL (BioManCo, 2018).

The occurring bed shear stresses throughout the modelled time period, accompanied with the possible WoO are presented in Figure 5.23, with the MSL case in the upper plot and the base case in the lower plot. Two time moments have been chosen, based on the two longest inundation-free periods, during which WoO are tested. Based on Equation 2.12, a fixed value for $\tau_{cr;ero}$ has been chosen at 0.4 N/m^2 corresponding to the critical bed shear stress for erosion at a chenier (see Section 2.2.3). By adjusting the value for the growth rate of the vegetation strength (k) an indication can be acquired about the range of values in which k must lie to accomplish seedling establishment in this period. In Figure 5.23, the solid red and green lines correspond to the average and maximum k values according to Balke et al. (2011), respectively.

First, the focus lies on the MSL case, in the upper plot of Figure 5.23, in which it is assumed that colonisation occurs. In the first period, between 21 November and 2 December, WoO seem to occur for $k = 6.3e^{-3}$ Pa/h. For the second period, $k = 5.3e^{-3}$ Pa/h seems to suffice to accomplish establishment.

Under the applied assumptions, the mangrove seedlings should have a vegetation strength growth rate

between 5.3e^{-3} Pa/h and 6.3e^{-3} Pa/h to survive under these conditions on the inner side of a chenier.

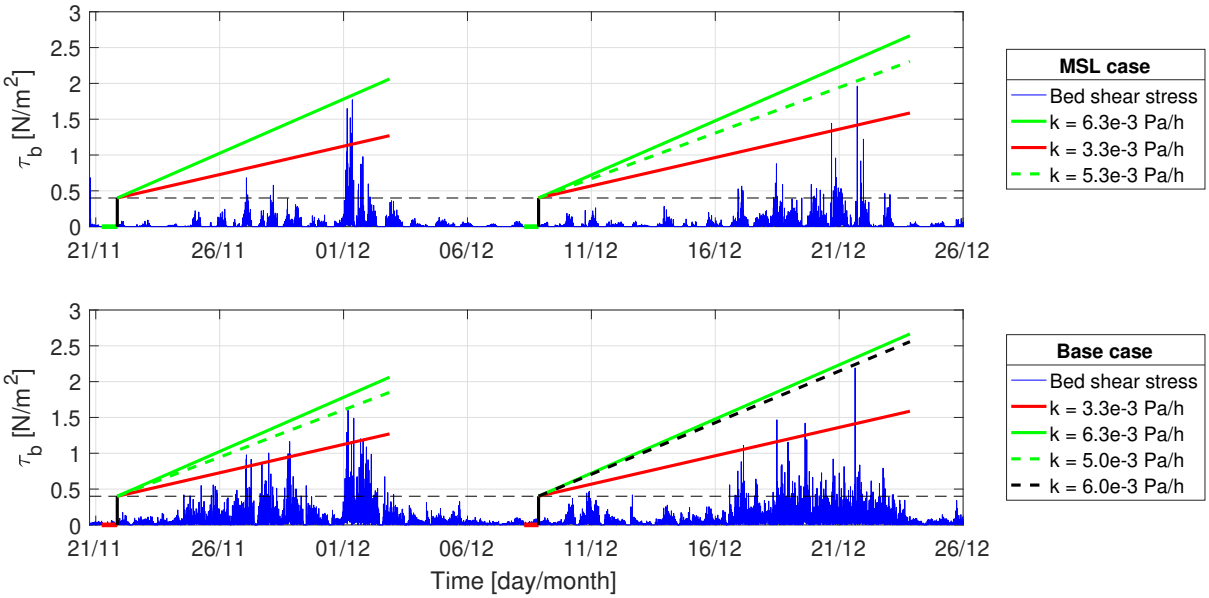

Figure 5.23: Windows of Opportunity at the inner side of the new chenier in the eroding transect. Upper: MSL case, lower: base case. Two moments in time have been selected based on an available inundation-free period. A fixed value for $\tau_{cr;ero}$ has been set at 0.4 N/m^2. The value for k is adjusted such to accomplish establishment.

By comparing the MSL case with the base case, presented in the lower plot of Figure 5.23, it seems that the highest occurring bed shear stresses remain of a similar value in both cases. The largest differences can be found in the overall shear stresses that are considerably lower for a higher chenier, as was also found in Figure 5.22, and the durations of inundation-free periods. Looking at the required growth rates for the base case scenario, this seems to suggest that the required value of k does not vary significantly for a higher chenier. However, it is important to note that the inundation-free periods in the MSL case, presented by the horizontal green lines in the upper plot of Figure 5.23, do not occur for the base case scenario, where the same periods have been marked with horizontal red lines in the lower plot. This indicates the importance of the bed level elevation of the chenier in order to accomplish seedling establishment. Furthermore, seedling establishment at cheniers is often endangered due to the large bed level variations that can occur here, which also followed from the bed level analysis in Section 5.2.6.

6. Discussion

In this chapter, the results that have been acquired during this research are discussed. First, the limitations of the research methods are described. Then, the results are discussed by means of three subjects: wave energy dissipation, sediment dynamics and Windows of Opportunity. Finally, the eroding and accreting transect are compared by discussing the influence of cheniers and vegetation on the behaviour of the shoreline.

6.1 Reflection on research methods

During this research, results have been collected by means of a data analysis and one-dimensional XBeach models. These methods are extensively described in Chapter 4. This section elaborates on the most important limitations of both research methods. Additional limitations regarding data analysis and modelling can be found in Appendix B.9 and Appendix C.3, respectively.

6.1.1 Data analysis

The data analysis has been carried out with a significantly reduced amount of data, mainly due to physical complications with the instruments that arose during the measurement period. Since the useful data comprises a relatively short time period (10 days), the trustworthiness of the data analysis outcomes got affected. The calibration of the wave loggers and the reliability analysis of the SED sensors are extensively described in Appendix B.4.2 and Appendix B.5, respectively.

Furthermore, the bathymetry of both transects was not measured accurately due to which the depth along the profile sections, with lengths up to 250 metres, had to be assumed based on literature and earlier system analyses. This created uncertainty about occurring dissipation mechanisms and affected the reliability of the XBeach modelling results. Additionally, the bathymetry was determined by linking the depth measurements to the stage of the tidal signal and the monthly average water level around the period of measurements (see Appendix D.3). It is important to note that the monthly average water level varies throughout the year, as described in Section 3.2.2 and Appendix D.1.2. This variation can increase up to thirty centimetres which considerably affects the bed level elevation of the transects compared to MSL and causes significant variations in durations of inundation-free periods throughout the year. Therefore, the bathymetry used during this research reflects on the period November-December 2017, only.

Moreover, it should be noted that the bed shear stresses that are calculated based on the wave analysis correspond to 15-minute intervals, due to which single large waves are excluded. This might have resulted in an underestimation of calculated shear stresses. At vegetated locations (E5, A8 and A9), the calculated shear stresses are overestimated since the effect of vegetation on the near-bed particle velocity is neglected. To include this, vegetation properties like stem diameter, vegetation height and drag coefficient are required. Lastly, the calculated shear stresses are wave-induced only. It is assumed that this approaches the actual occurring shear stresses good since the tidal current velocities are small (see Appendix D.1).

6.1.2 Modelling

A modified version of the numerical model XBeach (Bendoni, 2015) was used to reproduce the hydrodynamics along both the accreting and the eroding transect with two separate one-dimensional models. This way, scenarios have been simulated in order to analyse the local bed shear stresses along the transects for various situations. The used XBeach version is limited to the phase-averaging approach (surfbeat mode) to calculate hydrodynamics (see Appendix A.3). Since non-hydrostatic processes like wave breaking and interaction with vegetation occur along the transects, the application of the surfbeat mode brings a limitation to the model by affecting the reliability of calculated bed shear stresses along the transects. This is described in more detail in Appendix C.3. In order to model the non-hydrostatic behaviour of the flow on a single wave scale, the 'non-hydrostatic mode' should be used, which can be done in the original XBeach environment.

Furthermore, the model results are very sensitive to the bathymetry, as was found in Section 4.2.3. As mentioned in the previous section, the uncertainty about the bathymetry of the transects affects the reliability of the model results as well. In particular the determination of the vegetation strength growth factor (k) might vary dependent on the shape of the modelled chenier (see Section 5.3.3). Moreover, the presence of cheniers limited the one-dimensional flow along the modelled profiles. Due to the one-dimensional flow, the chenier in the accreting transect blocks the water during ebb and flood flows, whereas in reality the water flows around this obstacle. Therefore, waves only enter the transect when the water level exceeds the bed level of the chenier, which increases the length of the apparent inundation-free periods (periods of zero bed shear stresses) along the transect. The modelled inundation-free periods are overestimated by around four hours.

Finally, vegetation has been applied in the model to reproduce the effect of the vegetation patch on hydrodynamics in the accreting transect. It should be noted that the applied vegetation is not based on representative vegetation properties in the transect, but mainly configured in order to validate the data results. A quantitative analysis based on the modelled vegetation might therefore not be reliable. However, the modelled vegetation affects the waves similarly as was observed during the data analysis, i.e. relative increase of energy dissipation for larger waves. This way, the effect of vegetation on wave propagation along the transect, that was examined qualitatively in Section 5.3.1.2, can be assumed to correct. More information about vegetation properties, in terms of geometry (height/width) and density, is required to be able to model the vegetated areas with more care.

6.2 Wave energy dissipation processes

The wave transformation along the accreting and eroding transect has been analysed extensively in Sections 5.2.2 and 5.2.3. Wave friction coefficients (f_w) were calculated as a measure for the amount of wave energy dissipation along the separately defined sections in the transects. The calculated f_w values were compared to values that are representative for bottom friction on intertidal mud flats according to Lacy and MacVean (2016), i.e. $f_w = 0.02 - 0.1$. When f_w values above 0.1 are found, this indicates that additional dissipation processes rather than bottom friction are present. Figure 6.1 presents a visualisation of the amount of energy dissipation for various incoming wave heights in terms of f_w for the separate sections along both the eroding transect (Figure 6.1(a)) and the accreting transect (Figure 6.1(b). Note that Figure 6.1 is based on the calculated f_w values that are presented in Table 5.3 and is mainly presented here to give an indication of the difference in energy dissipation between the profile sections. The complete bathymetries of the profiles are presented in Figure 5.2.

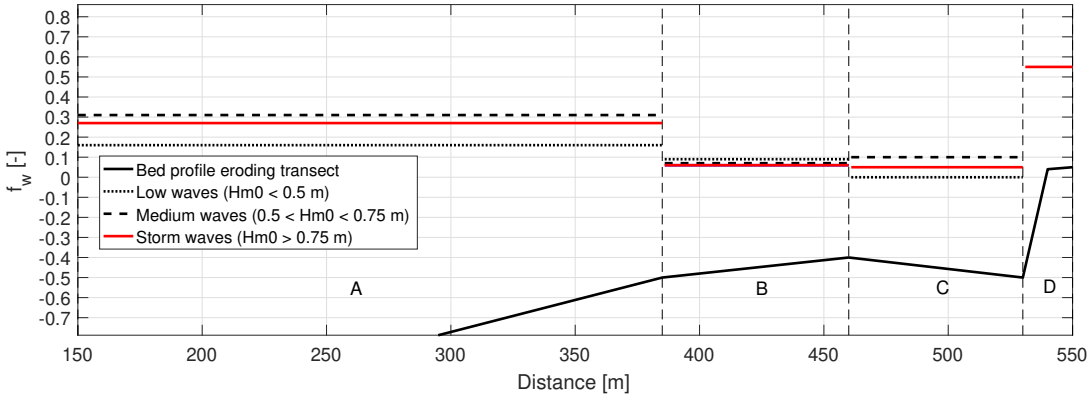

(a) Energy dissipation along the eroding transect

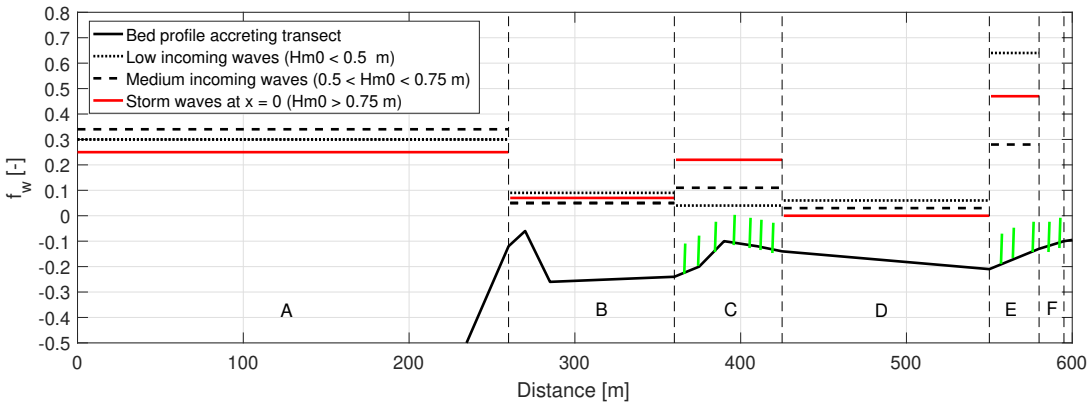

(b) Energy dissipation along the accreting transect

Figure 6.1: Wave energy dissipation in terms of f_w along the eroding transect (a) and the accreting transect (b), based on Table 5.3. Missing f_w values exceed the limits of the graph.

6.2.1 Wave breaking due to cheniers

The linear profile that had been assumed in section A of the eroding transect (see Figure 5.2), seemed to be a wrong assumption. Along this section, relatively much wave energy is dissipated ($f_w = 0.16 - 0.31$), which indicates that additional dissipation mechanisms, besides bottom friction, are occurring (see section A in Figure 6.1(a)). Fluid mud dissipation might be occurring, but this is not expected to be dominant. This is further explained in Section 6.2.3. Instead, based on a wave breaking analysis in Section 5.2.5 and a model sensitivity analysis in Section 4.2.3, it was found that a shallow obstacle must have been present, at the beginning of the measurement period (end November 2017), in the considered profile section with a maximum bed level around -0.3 m +MSL. Several possibilities for the occurrence of this obstacle can be thought of and are discussed hereafter.

The extended width of the cheniers that are present in front of the Demak coast seems to suggest the possibility that the chenier in the accreting transect might extend its tail towards the eroding transect, where the bed level is slightly lower (see Section 3.3.3). The obstacle in the eroding transect could also be a new, developing chenier, which is supported by BioManCo (2018) who observed at the *end* of the winter period that a chenier had developed in the eroding transect, up to a bed level around 0 m +MSL, whereas at the same time the chenier in the accreting transect had disappeared. This might as well be the result of alongshore propagation of the chenier due to which the top is now situated in the eroding transect and the tail in the accreting transect.

Furthermore, the wave friction coefficients in section B of the eroding transect showed values between 0.05-0.9 indicating a rather high bottom roughness compared to section C that is located closer to the shore. This is supported by the relatively large grain sizes measured in section B (30-60 μm) compared to section C (10 μm) (see Table D.2), resulting in higher wave friction coefficients. Again this supports the possibility that a sandy chenier was already present in the eroding transect.

The development of a chenier in the eroding transect probably affects the shoreline since waves break on the chenier and the cross-shore gradient in wave energy is enhanced (Winterwerp et al., 2013). Consequently, less erosion or even accretion of the currently eroding shoreline can be expected.

Chenier development is further elaborated on in Section 6.3 and the influence of the cheniers on the coastal morphology is discussed in Section 6.5.

6.2.2 Vegetation

The effect of vegetation on hydrodynamics was extensively studied prior to this research in order to understand the wave transformation along the vegetation patch in the accreting transect (see Section 2.3.2). In general, dissipation increases with wave height (as shown in Equation 2.10) and short waves dissipate relatively more compared to long waves (Mendez and Losada, 2004; Horstman et al., 2014). Additionally, it should be noted that the influence of the wave period on energy dissipation decreases from deep water ($kh >> 1$) towards shallow water ($kh << 1$).

Although the wave periods were not measured accurately, the average wave period seems to lie between 4-6 seconds, which implies that, combined with a small water depth, mainly shallow water situations occur along the accreting transect. Therefore, it can be expected that along the vegetation patch the wave height has a larger influence on the amount of energy dissipation by vegetation compared to the wave period. Consequently, at section C in Figure 6.1(b) the amount of energy dissipation increases considerably for larger wave heights ($f_w = 0.04 - 0.22$). Furthermore, the higher friction values were accompanied by larger water depths as well, indicating that a larger part of the mangrove is submerged which may result in more drag resistance from the mangrove canopy.

On average, the wave period behind the vegetation patch is slightly longer than in front of the patch (5.1 seconds against 4.6 seconds on average), supporting the relatively large amount of *short* wave dissipation. Compared to the amount of energy dissipation due to bottom friction only, the effect of vegetation seems to be rather small, especially during low wave heights ($H_{m0} \leq 0.15$ m). Also given the fact that the vegetation patch mainly consists of sand, with a relatively high wave friction coefficient, this suggests that vegetation hardly affects the wave heights during small wave events. However, it should be noted that, even during small wave events, the peak wave periods increase. Consequently, the bed shear stresses at the shoreline decrease even if the wave heights remain unchanged.

The effect of the vegetation patch on wave dissipation was further explored with the XBeach model (see Section 5.3.1.2). It appeared that for very large wave events, such as the 1 December storm, the vegetation attenuates wave energy even more than the chenier, indicating the importance of the vegetation patch on shoreline protection in the accreting transect. It should be noted though that the applied vegetation in the model does not represent the actual vegetation properties from the field, as mentioned in Section 6.1.2. Therefore, the modelled effect of vegetation on hydrodynamics might deviate from reality. In order to understand the effect of the vegetation patch on wave dissipation better, the vegetation properties should be studied in more detail to be able to apply the actual vegetation into the model with more care.

6.2.3 Bottom friction and fluid mud dissipation

The grain sizes along the transects vary locally, as can be seen in Table D.2. The results of the data analysis showed that this local variability in grain sizes affects the amount of energy dissipation due to bottom friction (see Section 5.2.3). A clear difference could be identified between relatively sandy sections (e.g. section B in Figure 6.1(a)), with $0.06 \leq f_w \leq 0.09$, and muddy sections (e.g. section D in Figure 6.1(b)), with $0 \leq f_w \leq 0.06$. In muddy sections, the possible occurrence of fluid mud dissipation must also be considered.

Close to the shore in the accreting transect, along section D, the bed becomes more muddy and relatively fluid, as was observed by BioManCo (2018). This observation tends to indicate an additional energy dissipation process, namely fluid mud dissipation (see Section 2.2.4). The amount of energy dissipation in this section is low overall ($f_w = 0 - 0.06$), with less dissipation for larger waves. This is in contrast with Elgar and Raubenheimer (2008) who found that fluid mud dissipation rates increase for lower frequencies, indicating that fluid mud dissipation is probably not dominantly present here. However, fluid mud dissipation is also strongly sensitive to the local water depth which increases during large wave events and consequently decreases the effect of fluid mud on the energy dissipation (Rogers and Holland, 2009). Since the layer thickness and viscosity of the fluid mud layer largely determine the amount of energy dissipation, more insight in these sediment properties is required to examine the effect of fluid mud on wave energy dissipation in more detail (Rogers and Holland, 2009).

6.3 Sediment dynamics

The morphology largely influences the possibility for Windows of Opportunity at a location, as can be seen in Equation 2.12. Therefore, in this section the observed behaviour of the bed level at specific locations is discussed in order to discover the relevant physical processes that influence the morphology.

6.3.1 Sediment characteristics

According to laboratory experiments by BioManCo et al. (2018), the soil samples from muddy areas in Demak contain on average around 20% fine sand and have a dry density of 585 kg/m^3 due to which the soil can be characterised as light sandy mud (Mitchener and Torfs, 1996). According to Mitchener and Torfs (1996) this corresponds to a critical bed shear stress between 0.15-0.25 N/m^2. Additionally, based on the same experiment, for the sediment at the sandy cheniers, a critical bed shear stress between 0.4-1.5 N/m^2 can be expected.

Whereas the muddy samples that have been used in the laboratory experiments give a good indication of the *average* grain size at the muddy areas along the Demak coast, the grain sizes along the investigated transects differ and might deviate from average values. As mentioned in Section 3.3.1, the grain sizes decrease towards the shore, leading to decreasing values for the critical shear stress for erosion ($\tau_{cr;ero}$) towards the shore, as well, as was found during the bed level analysis in Section 5.2.6.

Along the accreting transect, where most of the SED sensors were deployed, the highest value of $\tau_{cr;ero}$ was found at the sandy chenier, with $\tau_{cr;ero} \approx 0.4$ N/m^2, which is in line with the expected value of $\tau_{cr;ero}$ at the chenier as well (BioManCo et al., 2018; Mitchener and Torfs, 1996). Although no samples have been taken at the vegetation patch, it is believed that this is an old chenier, based on the sandy soil that was observed here (BioManCo, 2018). Therefore, $\tau_{cr;ero}$ has probably a comparable here to that at the chenier. Just at the landward side of the vegetation patch, $\tau_{cr;ero}$ had decreased to around 0.15 N/m^2 to decrease even further into the muddy mangrove forest to $\tau_{cr;ero} \approx 0.05 - 0.10$ N/m^2.

In the eroding transect, the bed profile is rather sandy overall with grain sizes similar or slightly larger than just behind the vegetation patch in the accreting transect. At the edge of, and inside the mangrove forest, the mud has similar grain sizes as in the accreting transect.

The varying grain sizes along the transects affect the possibilities for mangrove establishment, since these possibilities rely on a sufficiently large value for $\tau_{cr;ero}$ (see Equation 2.12). This is further discussed in Section 6.4.

6.3.2 Bed level development

According to Winterwerp et al. (2005), a large gradient in shear stresses from offshore to nearshore is required to provide transport of fine sediments in nearshore direction. During the bed level analysis, it was observed that at various locations in the transects, sedimentation events occurred when large offshore waves were observed (see Section 5.2.6).

Distinction can be made between *gradual* erosion or sedimentation events and *sudden* events. At the forest edge in the eroding transect, the long term bed level development is clearly associated with the offshore wave climate as can be seen in Figure B.27. During high wave events the bed is rather stable, or even accreting, whereas during low waves the bed erodes. In this case, the eroding or stable pattern remains for at least a couple of days.

Just behind the vegetation patch in the accreting transect, the storm of 1 December resulted in local shear stresses beyond 0.25 N/m^2, but these resulted in a sudden sedimentation peak. It is likely that at this location, sand deposited that was earlier eroded from the sandy vegetation patch where shear stresses over 0.4 N/m^2 occurred during the same event. At the landward side of the vegetation patch the shear stresses drop far below 0.4 N/m^2, causing the observed deposition.

Around the chenier, similar sedimentation peaks have been observed, but with a longer duration. Sediment is eroded in front, and on top of the chenier and is deposited at the landward side of the chenier, as can be seen clearly between 25 November and 2 December in Figure 5.13. This seems to suggest that the chenier that was present at the beginning of the measurement period has been propagating in onshore direction. The observations also suggest that a new chenier has arrived at this location around half December, around the same time as when the offshore waves have been picking up. This is further explored in Section 6.3.3.

The above mentioned theory of Winterwerp et al. (2005) is supported by the results of the bed level analysis. It should be noted that the theory tends to have a different effect on sand and mud. Due to its larger grain size, sand reacts much faster on hydrodynamic forcings than mud, resulting in sudden sedimentation peaks, especially around the chenier and the vegetation patch, whereas fine sediments show a more gradual behaviour.

6.3.3 Chenier development

Although cheniers are dominant appearances along the Demak coastline, as was elaborated on in Section 3.3.3, it is still uncertain how they move and how they are being formed.

Cross-shore chenier propagation should be associated with erosion on the seaward side and deposition at the landward side of the chenier, which was observed to occur at the chenier in the accreting transect (see Section 5.2.6 and 6.3.2). Earlier, in Section 6.2 the suggestion was made that cheniers might even be moving in alongshore direction, which might be associated with alongshore currents. However, the data collection of this research did not allow for studying alongshore chenier propagation. More information about nearshore currents and bed level changes in alongshore direction are desired to study chenier propagation in more detail.

The observed movement or development of cheniers seems to coincide with the amount of wave energy, and probably also the duration of wave events, which can be seen at the development of a chenier at A3 around half December (see Figure 5.13). It should be noted though that this instrument had been moved, probably around the same time, due to which these observations might not be reliable (see Section 6.1.1). However, at the edge of the eroding forest, a long period of erosion suddenly changed into a long period of a stable, or even accreting bed level during a relatively long high energy wave event, as can be seen in Figure B.27. In Section 6.3.2 it was discussed that this reversal is the result of a large offshore to nearshore shear stress gradient. However, that gradient must have been achieved by a sufficiently large obstacle, indicating that the small chenier that was already present in the eroding transect had likely grown larger during the same high wave event. This would also support the observations of BioManCo (2018) who observed a chenier around MSL in the eroding transect after the winter period.

Since a chenier is a lens of sand situated in a muddy environment, mechanisms for sorting coarse sediment grains from fine grains must be occurring (Slingerland and Smith, 1986). According to Slingerland and Smith (1986) sorting can take place during deposition, where coarse grains separate from fine grains

due to their difference in settling velocities. The sediment composition in the Demak area shows that relatively large sand particles (100-500 μm) are present in the soil (BioManCo et al., 2018), explaining the large grain sizes at the chenier ($D_{50} \approx 150\mu$m, see Table D.2). During periods of high wave energy both sand and mud might come in suspension, after which sand deposits rather quickly and mud is likely transported elsewhere. This segregation might cause that a sand bar is formed locally. This process requires a peak in shear stresses (likely to be caused by wave breaking) on the location where the chenier is developed, in order to initiate the sorting process. More research into the development and behaviour of cheniers is required to understand these processes better.

6.4 Windows of Opportunity

In order to determine whether Windows of Opportunity for mangrove establishment occur in the considered transects, the threshold conditions for establishment of an *Avicennia alba* seedling are used, which are defined by Balke et al. (2011) as a sequence of four events.

6.4.1 Seedling dispersal

The first event that must occur is seedling dispersal. Seedling dispersal is dependent on the availability of seeds, which changes on a seasonal time scale, and a simultaneously occurring high water event to transport the seeds towards the shoreline. The fruiting season differs per mangrove specie and also depends on the geographical location. According to BioManCo (2018), *Avicennia marina* establishes mainly during the south-east monsoon period whereas *Avicennia alba* seedlings were found mainly after the north-west monsoon (see Section 3.3.2). Other research showed that *Avicennia marina* has its fruiting season between December and February, although this was measured in Bali (Indonesia) (Kitamura, 1997). In this particular research it was assumed that seedling dispersal occurs throughout the whole year, in order to focus mainly on the second and third conditions (disturbance from tidal inundation and wave forcing) defined by Balke et al. (2011), but it should be noted that without seedling dispersal, Windows of Opportunity can not occur.

6.4.2 Inundation-free period

The second condition describes an inundation-free period of 5 days that is required to let the roots of the stranded seedlings grow sufficiently long to prevent them from floating. Model results showed that the longest inundation-free period, measured at the highest situated location in the accreting transect, takes only around fifteen hours. Nevertheless, mangrove establishment has been found to occur in the accreting transect even at lower situated locations (BioManCo, 2018).

However, the bathymetry was determined based on the average water level over a short time period. An analysis of the measured water levels at the tidal station of Semarang (as described in Appendix D.1.2) showed that the monthly averaged water level varies considerably on a seasonal time scale, with differences up to thirty centimetres. Consequently, longer inundation-free periods can be expected when the average water level is relatively low, which generally occurs between February-April and August-September (see Figure D.3). Since the highest water levels occur during the north-west monsoon period, the *Avicennia alba* seedlings are possibly less likely to survive compared to the *Avicennia marina* seedlings that seem to establish during the south-east monsoon period.

For this research, the bathymetry was determined based on the average water level during November-December 2017. In March 2017, the average water level was twenty centimetres lower which would result in a higher bed profile compared to MSL, as presented in Figure 6.2. The tidal signal during March 2017 (as presented in Figure D.4) shows that a minimum bed level of around 10 cm +MSL is required in order to acquire an inundation-free period of 5 days in this month. This threshold is included as the solid green line in Figure 6.2 and it can be seen that even in March 2017, this threshold is hardly exceeded along the profile.

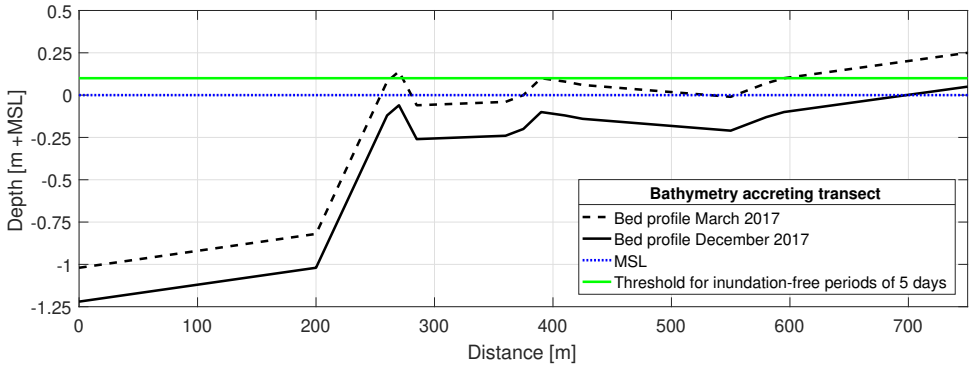

Figure 6.2: Comparison of the bathymetry of the accreting transect in March 2017 and December 2017. The solid green line represents the threshold bed level above which inundation-free periods from 5 days or longer can occur based on the tidal signal in March 2017.

Therefore, inundation-free periods of 5 days are still not likely to occur which indicates that the minimum inundation-free period at this specific site location might be shorter compared to the flume experiments that were carried out by Balke et al. (2011), which seems to suggest that the seedling roots attach to the soil much earlier. Various reasons for this difference can be proposed.

The mangrove seedlings in the flume experiment from Balke et al. (2011) were inevitably exposed to different circumstances than the mangrove seedlings in the coastal area of Demak. The availability of nutrients in a flume is likely much scarcer than in nature which might result in a longer required inundation-free period in order to reach a sufficient root length to prevent floating. Another possibility is that mangrove seedlings have been growing already on higher grounds after which they have been washed away to lower grounds where the roots entangled in the soil rather quickly, resulting in a shorter required inundation-free period (personal communication with prof. P.M. Herman). In the remainder of this section it is assumed that long enough inundation-free periods occur throughout the considered time period.

6.4.3 Minimum disturbance from bed shear stresses

The inundation-free period should be followed up by the third condition, a period of low bed shear stresses during which the seedling roots gain strength and are able to resist larger forces as time goes on. For convenience, the equation that determines the vegetation strength of a seedling (Equation 2.12) is presented here again (Hu et al., 2015a):

$$\tau_v = k(t - t_{WoO1}) + \tau_{cr;ero} \tag{6.1}$$

The growth rate of the vegetation strength (k) and the critical shear stress for sediment mobilisation ($\tau_{cr;ero}$) are important parameters in order to determine whether a long enough period of low bed shear stresses occurs and how large these maximum shear stresses may be. The representative values for k and $\tau_{cr;ero}$ have been found to come with large uncertainties and are likely to vary strongly for various situations.

According to Balke et al. (2011), the maximum shear stress to prevent dislodgement of an *Avicennia alba* seedling increases linearly from 0.17 N/m^2 to 0.52 N/m^2 in approximately three days. Following Equation 6.1, this means that the value of $\tau_{cr;ero}$ lies around 0.17 N/m^2. Since $\tau_{cr;ero}$ depends on the local sediment properties, it is evident that this value varies for the location of this research, between 0.05-0.15 N/m^2 for muddy locations and around 0.4 N/m^2 around cheniers (see Section 5.2.6). The importance of $\tau_{cr;ero}$ for seedling establishment already indicates that seedlings can establish on cheniers under more rough conditions than at muddy locations, supporting the mangrove colonisation on the old chenier in the accreting transect. It should be noted though that muddy areas are favourable for mangrove growth based on soil properties like nutrient availability, soil fertility and salinity (Hossain and Nuruddin, 2016; Ball, 1998).

In Equation 6.1, the value for k is uncertain as well. Based on the average growth rate in the experiments

of Balke et al. (2011), k can be estimated at $3.3e^{-3}$ Pa/hour (1 Pa = 1 N/m^2). However, the minimum and maximum values lie around $1.2e^{-3}$ Pa/h and $6.3e^{-3}$ Pa/h, respectively. This value has a considerable effect on the Windows of Opportunity that can be identified, as was shown in Section 5.3.1.1.

For two muddy locations, one just at the landward side of the vegetation patch (location 1, $\tau_{cr;ero} = 0.10 - 0.15$ N/m^2) and one just in front of the mangrove forest (location 2, $\tau_{cr;ero} = 0.05 - 0.10$ N/m^2), the possibilities for occurring WoO were tested by varying $\tau_{cr;ero}$ and k within representative values. Furthermore, it was assumed that a selected inundation-free period (on 21 November 2017) was sufficiently long to prevent the seedlings from floating.

It was found that at location 1, the initial growth rate of $3.3e^{-3}$ Pa/hour seems to be sufficient to allow for seedling establishment, for both $\tau_{cr;ero} = 0.15$ N/m^2 as for $\tau_{cr;ero} = 0.10$ N/m^2. Applying the minimum growth rate would inevitably result in dislodgement here (see Figure 5.17). At location 2, only the worst combination of $\tau_{cr;ero} = 0.05$ N/m^2 and $k = 1.2e^{-3}$ Pa/h would result in dislodgement, whereas for the other combinations Windows of Opportunity seemed to occur.

The results have shown that k is the most sensitive parameter in Equation 6.1 due to which it is much desired to define the best applicable value for this parameter in more detail. An attempt has been made to determine an indication for k based on observed mangrove colonisation on developing cheniers, as was found by BioManCo (2018). Under the assumption that mangrove colonisation had occurred on the inner side of a chenier (top at 0 m +MSL), between 20 November - 31 December 2017, the mangrove seedlings must have had a strength growth rate between $k = 5.3e^{-3}$ Pa/h and $k = 6.3e^{-3}$ Pa/h (see Section 5.3.3). This lies within the range of observed k values of the experiment by Balke et al. (2011).

6.4.4 Minimum disturbance from sediment dynamics

The last stage of the WoO as defined by Balke et al. (2011) focuses on the ability of seedlings to outgrow or adjust to disturbances from erosion and sedimentation events (Balke et al., 2013). According to Balke et al. (2013) disturbance from sediment dynamics can be seen as a main bottleneck for mangrove colonisation. This stage is mainly important for locations where large variations in bed level can occur, like at cheniers as was found in Section 5.2.6. At these locations, it is likely that seedlings survive the external hydrodynamic forces due to the strong soil characteristics, but eventually fail due to the dynamic behaviour of the chenier. At dynamic morphological locations it is therefore desired that fast-growing seedlings establish to resist sediment disturbances. This might be a reason that the faster growing *Avicennia alba* establishes mainly during the north-west monsoon, when the morphology is most dynamic.

Due to the deviant required inundation-free period compared to Balke et al. (2011), the spatially varying value for $\tau_{cr;ero}$ along the transects and the large uncertainty about the value of k that holds for this project area, it cannot be said with certainty whether Windows of Opportunity actually occur in the accreting transect within the considered time frame (20 November - 31 December 2017). This indicates the necessity of more research into the representative values for these parameters in the considered area, together with a validation of actual seedling establishment with corresponding hydrodynamic conditions.

6.5 Comparing both transects

The distinction that has been made between an eroding and an accreting transect has been supported by the bed level analysis in Section 5.2.6 that presents gradual erosion inside the forest in the eroding transect and accretion inside the forest of the accreting transect. This is probably the cause of the chenier and the vegetation patch that are only present in the accreting transect, as was discussed in Section 6.2. Furthermore, the bed level along the eroding transect is situated significantly lower than the accreting transect, resulting in larger waves that can approach the shore, inducing more erosion. However, the morphology of both transects has changed during the winter period, as was observed by BioManCo (2018). Whereas the chenier in the accreting transect seemed to have disappeared, a chenier became clearly visible in the eroding transect.

In order to gain more insight into the effects of the physically changed appearance of both transects, modelling scenarios were carried out for both the accreting and the eroding transect. An attempt is made to identify the tipping point beyond which the eroding transect changes into an accreting transect and vice versa.

The focus has been concentrated on the effect of the chenier and the vegetation patch on the bed shear stresses at specific locations. Modelling results in Section 5.3.1.2 have showed that in the accreting transect, the complete disappearance of the chenier would result in a doubling of the average bed shear stresses during HW at locations 1 and 2 (defined in Section 6.4). Whereas with a chenier present, these locations have an accreting or stable bed level, without a chenier these locations will inevitably be eroding. This supports the earlier hypotheses of EcoShape (2015) which imply that coastline stability is likely the result of, amongst others, the presence of cheniers.

Based on BioManCo (2018), who observed that the chenier in the eroding transect had grown towards approximately 0 m +MSL during the winter period, model tests were carried out in order to analyse the effect of this developing chenier on the occurring bed shear stresses around the shoreline. The model results showed that when the chenier height is increased from the initially determined -0.3 m +MSL towards 0 m +MSL, the shear stresses around the shoreline decrease sufficiently to allow for bed level accretion, which can be seen in Figure 5.21.

The effect of vegetation on wave dissipation was already discussed in Section 6.2, and based on this it can be concluded that both the vegetation patch and the chenier are necessary in order to maintain a stable shoreline in the accreting transect. Whereas the vegetation mainly dissipates large waves, cheniers can be seen as more continuous defence mechanisms, as the model results showed in Section 5.3.1.2. Therefore, when the chenier shrinks in size, as has been observed in the accreting transect during the winter period by BioManCo (2018), it can be expected that this will result in erosion of this shoreline.

The considerable effect of a chenier on the occurring shear stresses along the transects already indicates that the changing appearances of both transects influence the possibilities for occurring Windows of Opportunity as well. As presented in Figure 5.20 the possibilities for WoO along the accreting transect will reduce significantly, although it should be noted that this strongly depends on the applicable values for $\tau_{cr;ero}$ and k. On the other hand, the calmer conditions in the eroding transect will positively affect the possibilities for WoO here. It should be noted though that, since the eroding transect is situated significantly lower than the accreting transect, the calm conditions must hold on long enough to provide the desired bed level elevation to achieve sufficiently long inundation-free periods, in the first place.

7. Conclusions and recommendations

In this chapter, the final conclusions of this research are presented and recommendations for further research are proposed.

7.1 Conclusions

Two transects without permeable structures along the coastline of Demak (Indonesia), one with mangrove recruitment and one with mangrove retreat, have been analysed during the north-west monsoon period in terms of hydrodynamics and morphology in order to answer the following question:

Can Windows of Opportunity for mangrove establishment be identified, looking at the effect of waves?

A wave data analysis was successfully carried out in order to gain insight about the wave transformation along the transects and the relevant energy dissipation mechanisms. The energy dissipation mechanisms included in the analyses are cheniers, vegetation and bottom friction. The analysis showed that cheniers are most effective in continuously inducing a large gradient in wave energy from offshore to nearshore and are therefore essential in order to maintain a stable coastline (see Figure 7.1).

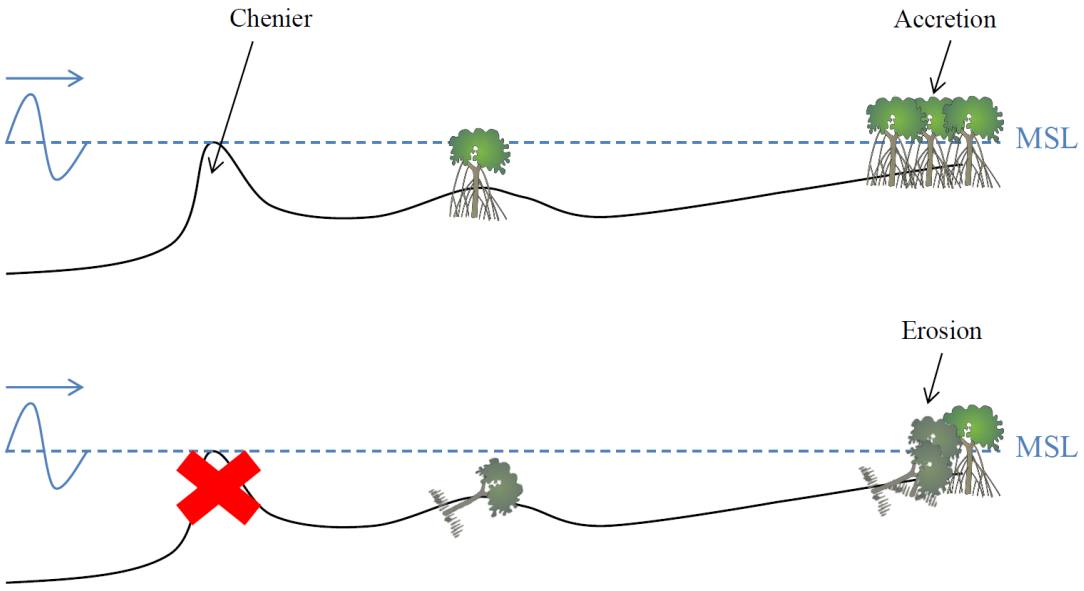

Figure 7.1: Dominant influence of cheniers on the stability of the coastline.

Vegetation seems to be mainly effective in attenuating large waves, rather than small waves. Due to the shallow water conditions the influence of the wave period on the amount of energy dissipation by vegetation is relatively small. Furthermore, the heterogeneity of grain sizes along the transects affects the amount of dissipation due to bottom friction locally, though bottom friction does not seem to be an important energy dissipation mechanism in the considered coastal area.

In order to study the morphology along the transects, a bed level analysis was carried out. This analysis showed that the morphology is most dynamic around the chenier, where the largest shear stresses occur. Based on the results, it was found that cheniers might propagate in cross-shore direction during relatively long periods of high wave energy. Sheltered locations have a more stable bed level, but still show a response to the wave climate.

The bed level analysis also showed that the sediment grain sizes, and thus the critical shear stresses for bed erosion ($\tau_{cr;ero}$), vary along the transects. As $\tau_{cr;ero}$ is an important requirement for WoO (Equation

2.12), this indicates the spatial variation of the initial vegetation strength along the transects.

The wave transformation along the eroding and the accreting transect was successfully reproduced with the numerical model XBeach, by means of two separately validated one-dimensional models, one for each transect. Two locations along the accreting transect, in between the vegetation patch and the mangrove forest, were selected in order to identify Windows of Opportunity based on Balke et al. (2011).

It was concluded that, due to the uncertainty about the required length of the inundation-free period, the spatially varying value for $\tau_{cr;ero}$ and the uncertainty about the required value for the growth rate of the vegetation strength (k, see Equation 2.12), it could not be confirmed whether Windows of Opportunity have occurred in the transects throughout the considered time period. However, it was found that the average water level varies significantly throughout the year with the highest water levels occurring during the period in which data for this research was collected. Although it cannot be said with certainty when the fruiting seasons of the dominant mangrove species exactly occur, based on the monthly average water levels, it seems that February-April and August-September are the best periods for mangrove establishment. Finally, as an addition to the threshold conditions defined by Balke et al. (2011), model results showed that an applicable value for the vegetation strength growth rate (k) in this area can be estimated to lie between $5.3e^{-3}$ Pa/h and $6.3e^{-3}$ Pa/h.

7.2 Recommendations

Several recommendations for further research are formulated in this section. First, recommendations regarding the application of this study are described, after which improvements for further research are proposed.

7.2.1 Application

This research improved the system understanding at the coastal zone of Demak with an emphasis on the importance of cheniers for coastal stability and mangrove recruitment. The improved system understanding will help in revealing the processes that are important to analyse in more detail during further research, which is elaborated on in Section 7.2.2. Furthermore, the acquired knowledge about wave transformation and morphological behaviour along the transects is valuable when it comes to validating future numerical models of the coastal area. This opens the possibility of modelling a larger stretch of the coastline with a certain degree of validation. Finally, new insights into the effect of cheniers on wave energy dissipation can be used in order to fulfil the desire of reproducing a similar effect to achieve coastline stability. An attempt might be made to identify and realise Windows of Opportunity for natural chenier development. For instance, by forcing local sediment sorting to initiate a positive feedback to enhance chenier development (see Section 6.3.3). Another suggestion might be to focus on artificial chenier development, for instance by means of sand nourishments.

7.2.2 Further research: data collection

This research highlights the importance of cheniers which raises in particular questions about the development and behaviour of these sandy structures. During the next field trip, it is important that the BioManCo project team focuses on studying the behaviour of cheniers thoroughly. In this research, studying the behaviour of cheniers was limited to cross-shore propagation and not much could be concluded in terms of sediment transport. Deploying SED sensors in alongshore direction, measuring sediment transport (by means of collecting multiple sediment samples at a location through time) and collecting drone images are examples of actions that can be carried out in order to track chenier propagation along the shore. Furthermore, it is much desired to map a detailed bathymetry around cheniers and monitor how this bathymetry changes through time as well.

In order to gain more insight about the vegetation growth rate (Equation 2.12) that is applicable for the pioneer mangroves in this area, it is desired to analyse how seedlings develop during a certain period of which the hydrodynamic conditions are known. This can be done by measuring the seedling density at a certain location before, and after a series of wave measurements.

7.2.3 Further research: numerical modelling

Modelling results in this research showed that nearshore hydrodynamics are very sensitive to physical processes such as severe morphological changes (chenier development) and energy dissipation by vege-

tation. Yet, knowledge about the development of cheniers and establishment of vegetation in this area is limited. Therefore, it might not be feasible to include and validate hydrodynamics, morphological behaviour (including chenier development), and dynamic vegetation in a single numerical model. It is important to take into account that the model results are very sensitive to these uncertain physical processes which considerably affect the reliability of model outcomes. It is therefore recommended that model studies are focused on particular processes that occur in the area about which more knowledge is desired.

When the focus lies on understanding chenier development, the wave data analysis of this research can be used to validate a non-hydrostatic XBeach model which includes processes like wave asymmetry and skewness that affect sediment transport. Although the original version of XBeach does not contain cohesive sediment transport formulations, a detailed hydrodynamic model can already be useful in order to predict or explain morphological changes.

Furthermore, current studies on the implementation of dynamic vegetation in numerical models can be improved based on the application of Windows of Opportunity and vegetation growth properties, as was done in this research.

To conclude, I want to raise everyone's awareness about the importance of nature-based solutions in civil engineering. Large-scale application of the Building with Nature concept is much desired in order to protect ourselves from sea-level rise while maintaining prosperous and flourishing coastlines around the world. Make Building with Nature trending topic in civil engineering!

8. Bibliography

Balke, T., Bouma, T. J., Horstman, E. M., Webb, E. L., Erftemeijer, P. L. A., and Herman, P. M. J. (2011). Windows of opportunity: thresholds to mangrove seedling establishment on tidal flats. *Marine Ecology Progress Series*, 440:1–9.

Balke, T., Herman, P. M. J., and Bouma, T. J. (2014). Critical transitions in disturbance-driven ecosystems: identifying windows of opportunity for recovery. *Journal of Ecology*, 102:700–708.

Balke, T., Webb, E. L., Van den Elzen, E., Galli, D., Herman, P. M. J., and Bouma, T. J. (2013). Seedling establishment in a dynamic sedimentary environment: a conceptual framework using mangroves. *Journal of Applied Ecology*, 50:740–747.

Ball, M. (1998). Mangrove species richness in relation to salinity and waterlogging: A case study along the adelaide river floodplain, northern australia. *Global Ecol. Biogeogr. Lett.*, 7:73–82.

Bendoni, M. (2015). Salt marsh edge erosion due to wind-induced waves Dissertation. Phd thesis, University of Braunschweig and University of Florence, Florence.

BioManCo (2018). PhD reseach project; Bio-morphodynamic modeling of Mangrove-mud Coasts. Phd research project, Delft University of Technology, Delft.

BioManCo, Smits, B. P., and Hanssen, J. (2018). Soil properties in Demak. Report of laboratory experiments, Delft University of Technology and Deltares, Delft.

Bosboom, J. and Stive, M. J. F. (2015). Coastal Dynamics I. Lecture notes, Delft University of Technology, Delft.

Cole, P. and Miles, G. V. (1983). Two-dimensional model of mud transport. *Journal of Hydraulic Engineering*, 109:1–12.

Deltares (2014). Delft3D-FLOW User Manual. Manual, Deltares, Delft.

Deltares (2015). XBeach User Manual. Manual, Deltares, Delft.

Deltares (2018a). Deltares. `https://www.deltares.nl/nl/software/delft3d-suite/`. Accessed: 22-02-2018.

Deltares (2018b). Deltares. `https://www.deltares.nl/en/software/delft3d-flexible-mesh-suite/`. Accessed: 22-02-2018.

EcoShape (2015). Building with Nature Indonesia; Securing Eroding Delta Coastlines. Tech. report, Ecoshape.

Elgar, S. and Raubenheimer, B. (2008). Wave dissipation by muddy seafloors. *Geophysical Research Letters*, 35:1–5.

Faridah-Hanum, I. and Latiff, A. (2014). *Mangrove Ecosystems of Asia; status, challenges and management strategies*. Springer, New York.

Friedrichs, C. T. (2011). Tidal flat morphodynamics; a synthesis. *Elsevier*, pages 137–170.

Horstman, E. M., Dohmen-Janssen, C. M., Narra, P. M. F., van den Berg, N. J. F., Siemerink, M., and Hulscher, S. J. M. H. (2014). Wave attenuation in mangroves: A quantitative approach to field observations. *Coastal Engineering*, 94:47–62.

Hossain, M. D. and Nuruddin, A. A. (2016). Soil and mangrove: A review. *J. Environ. Sci. Technol.,*, 9:198–207.

Hu, Z., Belzen, J., Wal, D., Balke, T., Zheng, B. W., Stive, M., and Bouma, T. J. (2015a). Windows of opportunity for salt marsh vegetation establishment on bare tidal flats: The importance of temporal and spatial variability in hydrodynamic forcing. *J. Geophys. Res. Biogeosci.*, 120:1450–1469.

Hu, Z., Lenting, W., Wal, D., and Bouma, T. J. (2015b). Continuous monitoring bed-level dynamics on an intertidal flat: Introducing novel, stand-alone high-resolution sed-sensors. *Geomorphology*, 245:223–230.

IOC (2018). Ioc sea level monitoring. `http://www.ioc-sealevelmonitoring.org/station.php?code=sema`. Accessed: 12-09-2018.

Jonsson, I. G. (1966). Wave boundary layers and friction factors. *Proceeding of 10th conference on Coastal Engineering*, 2:1546.

JRC (2018). Webcritech. `http://webcritech.jrc.ec.europa.eu/SeaLevelsDb/Home/TideChart/1807`. Accessed: 22-03-2018.

Kitamura, S. (1997). Iden Mangrove. Book, Staf Ahli JICA / Forestry Agency Japan, Japan.

Krone, R. B. (1962). Flume studies of the transport of sediment in estuarial shoaling processes. Final Report Hydraulic Engineering Laboratory and Sanitary Engineering Research Laboratory. Report, University of California, Berkeley, USA.

Lacy, J. R. and MacVean, L. J. (2016). Wave attenuation in the shallows of san francisco bay. *Coastal Engineering*, 114:159–168.

Lofquist, K. (1960). Flow and stress near an interface between stratified liquids. *The Physics of Fluid*, 3:158–175.

Longuet-Higgins, M. S. (1953). Mass transport in water waves. *Phil. Trans. R. Soc. Lond. A.*, 245:535–581.

Mazda, Y., Magi, M., Kogo, M., and Nguyen-Hong, N. (1997). Mangroves as a coastal protection from waves in the tong king delta, vietnam. *Mangroves and Salt Marshes*, 1:127–135.

McIvor, A., Moller, I., Spencer, T., and Spalding, M. (2012). Reduction of wind and swell waves by mangroves. Natural Coastal Protection Series: Report 1. Report, The Nature Conservancy and Wetlands International, Cambride.

McIvor, A. L., Spencer, T., Moller, I., and Spalding, M. (2013). The response of mangrove soil surface elevation to sea level rise. *The Nature Conservancy and Wetlands International*, page 59 pages.

Mehta, A. J., Hayter, E. J., Parker, W. R., Krone, R. B., and Teeter, A. M. (1989). Cohesive sediment transport. i: Process description. *Journal of Hydraulic Engineering*, 8:1076–1093.

Mendez, F. J. and Losada, I. J. (2004). An empirical model to estimate the propagation of random breaking and nonbreaking waves over vegetation fields. *Coastal Engineering*, 51:103–118.

Miche, R. (1944). Mouvements ondulatoires des mers en profundeur constante on decroisante. *Annales des Ponts et Chaussees*.

Mitchener, H. and Torfs, H. (1996). Erosion of mud/sand mixtures. *Coastal Engineering*, 29:1–25.

Morison, J. R., Johnson, J. W., and Schaaf, S. A. (1950). The force exerted by surface waves on piles. *Journal of Petroleum Technology*, 2(05):149–154.

Mullarney, J. C., Henderson, S. M., Reyns, J. A. H., Norris, B. K., and Bryan, K. R. (2017). Spatially varying drag within a wave-exposed mangrove forest and on the adjacent tidal flat. *Continental Shelf Research*, 147:102–113.

Nepf, H. M. (1999). Drag, turbulence, and diffusion in flow through emergent vegetation. *Water Resources Research*, 35(02):479–489.

Partheniades, E. (1965). Erosion and deposition of cohesive soils. *Journal of the Hydraulics Division*, ASCE 91 (HY 1):105–139.

Rogers, W. E. and Holland, K. T. (2009). A study of dissipation of wind-waves by mud at cassino beach, brazil: Prediction and inversion. *Continental Shelf Research*, 29:676–690.

Slingerland, R. and Smith, N. D. (1986). Occurrence and formation of water-laid placers. *Ann. Rev. Earth Planet. Sci.*, 14:113–147.

Smits, B. P. (2016). Morphodynamic optimisation of the design of semi-permeable dams for rehabilitation of a mangrove-mud coast. Msc thesis, Delft University of Technology, Delft.

Suzuki, T., Zijlema, M., Burger, B., Meijer, M. C., and Narayan, S. (2012). Wave dissipation by vegetation with layer schematization in swan. *Coastal Engineering*, 59:64–71.

Systems, O. S. OSSI-010-003 Wave Gauge User Manual. Manual, Ocean Sensor Systems.

Van Ledden, M. (2003). Sand-mud segregation in estuaries and tidal basins. Phd thesis, Delft University of Technology, Delft.

Van Rijn, L. (1993). Principles of sediment transport in rivers, estuaries and coastal seas. Tech. rep., Delft Hydraulics, Delft.

Watson, J. G. (1928). *Mangrove forests of the Malay Peninsula*. Malayan Forest Records No. 6. Fraser and Neave, Kuala Lumpur.

Wegen, M. v. d., Jaffe, B., Foxgrover, A., and Roelvink, D. (2017). Mudflat morphodynamics and the impact of sea level rise in south san francisco bay. *Estuaries and Coasts*, 40:37–49.

Willemsen, P. (2016). Manual for analyzing raw data obtained with the SED sensor. Manual, TU Twente, Twente.

Winterwerp, J. C. (1999). On the dynamics of high-concentrated mud suspensions. Phd thesis, Delft University of Technology, Delft.

Winterwerp, J. C. (2011). The physical analyses of muddy sedimentation processes. *Elsevier*, pages 311–359.

Winterwerp, J. C. (2014). Rehabilitation of Mangrove-mud Coasts; the bridge between science and engineering or the road from engineering to science. Presentation, Deltares, Delft.

Winterwerp, J. C., Borst, W. G., and Vries, d. M. B. (2005). Pilot study on the erosion and rehabilitation of a mangrove mud coast. *Journal of Coastal Research*, 21(2):223–230.

Winterwerp, J. C., Erftemeijer, P. L. A., Suryadiputra, N., Eijk, P. v., and Zhang, L. (2013). Defining eco-morphodynamic requirements for rehabilitating eroding mangrove-mud coasts. *Wetlands*, 33:515–526.

Winterwerp, J. C. and Kesteren, W. G. M. (2004). Introduction to the physics of cohesive sediment in the marine environment. *Elsevier*, 56.

Winterwerp, J. C., Van Weesenbeeck, B., Van Dalfsen, J., Tonneijk, F., Astra, A., Verschure, S., and Van Eijk, P. (2014). A sustainable solution for massive erosion in Central Java. Tech. report, Deltares and Wetlands International.

Wyrtki, K. (1961). Physical Oceanography of the Southeast Asian waters. Tech. report, UC San Diego, San Diego.

List of Figures

List of Tables

A. Modelling software

This appendix elaborates on the modelling software that has been used in this research. It is described which model is the best suitable for this research by means of considering several options. Appendix C.1 describes the model set-up that is applied for this research.

The selection of a suitable model depends on several requirements. It is demanded that the model includes all of the following features:

- 1-dimensional wave propagation and transformation
- Cohesive sediment transport formula
- Interaction between hydrodynamics and vegetation

Several models were considered. The possibilities consist of standalone models and combinations of models. The main modelling suites are described first, after which an elaboration of a combination of models and modifications to existing models are described.

A.1 Delft3D

Delft3D is a software suite that is able to simulate 2D and 3D flows, sediment transport and morphology, waves, water quality and ecology, and provides the interaction between these processes (Deltares, 2018a). Delft3D-FLOW is the core of the model which simulates non-steady flow and transport phenomena by numerical calculations of the Navier-Stokes and transport equations. The model includes a vegetation model (simulate vegetation drag) and transport formulas for cohesive sediment (Deltares, 2014). SWAN is the default wave model that is used in Delft3D.

SWAN is an extensive module which includes several processes that are not necessary to include in case of a 1D model. Particularly directional spreading of waves is not a necessity for 1D models and will cause an unnecessary amount of computation time.

A.1.1 Roller model

Because of the difficulties with SWAN regarding 1D modelling, the 'roller model' option can be used. This is an extension of the original Delft3D program which assumes alongshore gradients to be zero at the lateral boundaries and allows the modelling of the effect of short waves on long waves (Deltares, 2014). The roller model is applicable in case of a narrow-banded wave spectrum with respect to direction and frequency. This way, a dominant frequency and direction can be extracted from the wave data in order to determine the direction of wave propagation. The model combines a wave action balance equation reflecting single frequency short waves to a roller energy equation representing infragravity waves originating from short wave dissipation via a breaker index formulation (Wegen et al., 2017). Wave dissipation is thus based on depth-induced breaking where the wave energy transforms in roller energy after which it dissipates through turbulence.

The main disadvantage of the roller model is that is not (yet) capable of of modelling the interaction between waves and vegetation. Since this is a vital part of mangrove-coast modelling, a stand-alone Delft3D model can not be used.

A.2 Delft3D Flexible Mesh

Delft3D-FM (DFM) is the successor of the Delft3D suite (Deltares, 2018b). The most important difference is that DFM uses a combination of structured and unstructured modelling of water related flows. Furthermore, DFM comes with an interface which makes modelling more user-friendly, an thus easier. The advantage of modelling with unstructured grids is not important for this case of modelling a 1D cross-shore coast. However, DFM is used a the basis for several modified models, for instance as a combination with XBeach which will be explained hereafter.

A.3 XBeach (official release)

XBeach is a numerical model that is used to calculate littoral hydrodynamics and morphological response of the nearshore area during storms. The hydrodynamic processes in the model comprise short wave transformation (refraction, shoaling and breaking), long- (infragravity-) wave transformation, wave-induced setup and unsteady currents. Also overwash and inundation are included. Furthermore, XBeach includes effects of vegetation, like damping on waves and currents (Deltares, 2015). The original version of XBeach does not include cohesive sediment transport formulas. Therefore, the original version of XBeach would not be compatible to model a mangrove-mud coast. However, since a modified version of XBeach will be used instead (see Section A.4), the important formulations for the calculation of hydrodynamics, which are not adapted in the modified version, will be shown here.

A.3.1 Hydrodynamics

In order to calculate hydrodynamics, the surfbeat mode of XBeach is used. This is a phase-averaging approach which calculates the short wave motion based on the wave action equation:

$$\frac{\delta A}{\delta t} + \frac{\delta c_x A}{\delta x} + \frac{\delta c_y A}{\delta y} + \frac{\delta c_\theta}{\delta \theta} = -SINK \tag{A.1}$$

in which A is the wave energy, c_g the group velocity, c_θ the refraction speed, and SINK refers to the dissipation induced by wave breaking, bottom friction or vegetation.

A.3.2 Bed shear stress

The bed shear stress is calculated with Equation A.2:

$$\tau_{bx} = c_f \rho u_E \sqrt{(1.16 u_{rms})^2 + (u_E + v_E)^2} \tag{A.2}$$

in which u_E and v_E are the Eulerian velocities in x- and y-direction, respectively.

Note here that the bed friction is a constant, and based on the Manning coefficient:

$$c_f = \frac{g n^2}{h^{1/3}} \tag{A.3}$$

A.3.3 Vegetation

The model supports the effect of vegetation on short- and long wave dissipation and flow interaction. The dissipation effect of vegetation on short waves is modelled by using the approach of Mendez and Losada (2004). The short wave dissipation is a function of the local wave height combined with vegetation parameters that are defined on specific locations in the model domain, being: the drag coefficient (C_d), the stem diameter (b_v), the vegetation density (N_v) and the relative vegetation height (α). The vegetation elements can be schematised by means of vertical layers. For a mangrove, these layers are for instance, the roots, stem and canopy. The total short wave dissipation (D_v) by vegetation is then the sum of the dissipation of all the specified layers ($\sum D_{v,i}$).

$$D_{v,i} = A_v \cdot \frac{\rho C_{D,i} b_{v,i} N v, i}{2\sqrt{\pi}} \cdot \left(\frac{gk}{2\sigma}\right)^3 \cdot H_{rms}^3 \tag{A.4}$$

Next to short wave dissipation, also long waves and the mean flow are affected by vegetation. This effect is modelled by adding a drag force to the momentum equation which value depends on the flow velocity, water density, and the earlier defined vegetation parameters. Again, the total drag force (F_D) is the sum of the computed drag force of different vertical layers ($\sum F_{v,i}$) that is described by Equation A.5.

$$F_{v,i}(t) = \frac{1}{2} \rho C_{D,i} b_{v,i} N_{v,i} h_{v,i} u^L(t) |u^L(t)| \tag{A.5}$$

A.4 XBeach with cohesive sediment

Bendoni (2015) developed a *sand-mud-module* for XBeach to account for the interaction between sand- and mud fractions, thus cohesive and non-cohesive sediment fractions. This module is based on the similar sand-mud module that is already implemented in Delft3D. The concept of Bendoni's sand-mud module is based on the fractions of sand and mud that determine the composition of the sediment. Since the clay content of the soil composition determines the cohesive behaviour of the sediments, the *sand-mud-module* defines a critical mud fraction ($p_{m,cr} = 0.3$) to represent a threshold beyond which cohesive sediment formulations for erosion (not for deposition) will be applied instead of non-cohesive formulation (Van Ledden, 2003). The cohesive sediment formulations for erosion and deposition are important for this research and are described hereafter. In any case, very fine sediments are considered ($d_{50,sand} = 0.2mm$) and bedload is neglected. The information in this section is purely based on the PhD-thesis by Bendoni (2015).

A.4.1 Hydrodynamics

Bendoni (2015) focuses on the phase-averaging approach to calculate hydrodynamics in the model. This mode is referred to as 'surfbeat mode' and is explained in Section A.3. The reason for this choice is that the other approach, the phase resolving approach, solves the Nonlinear Shallow Water Equations (NSWE) and accounts for the non-hydrostatic behaviour of the flow, such as wave steepening, swash processes, wave reflection and sediment transport at a single wave scale. Compared to the phase-averaging approach, this approach is much more computationally expensive and too extensive for the purposes of Bendoni's research.

It is important to note that for the calculation of the bed shear stress, distinction is made between hydrodynamics and morphology. For hydrodynamics, the bed shear stress is calculated by means of Equation A.2, whereas for morphology Equation A.11 is used.

A.4.2 Morphology

Erosion
The absolute erosion rate is:

$$E_m^* = \frac{1}{\rho_s} M_c \left(\frac{\tau_b}{\tau_{cr,c}} - 1 \right) H_f \left(\frac{\tau_b}{\tau_{cr,c}} - 1 \right) \tag{A.6}$$

in which M_c is the erosion parameter, τ_b is the critical shear stress for erosion and H_f is the Heaviside function. The Heaviside function equals 0 for a negative argument and 1 for a positive argument.

The erosion parameter, M_c, is calculated based on the erosion parameters for pure mud (M_m) and for the non-cohesive sediment fraction (M_{nc}):

$$M_{nc} = \rho_s w_{s,s} F_s \cdot 0.015 \frac{d_{50,s}}{a_c d_*^{0.3}} \tag{A.7a}$$

$$M_c = \left(\frac{M_{nc}}{M_m} \right)^{\frac{1-p_m}{1-p_{m,cr}}} \cdot M_m \tag{A.7b}$$

in which $w_{s,s}$ is the sand settling velocity, F_s is a shape factor, a_c is the reference height from the bed for the equilibrium sediment concentration and d_* is the dimensionless grain size.

The critical shear stress for erosion of cohesive sediment fractions was defined by Van Ledden (2003):

$$\tau_{cr,c} = \frac{\tau_{cr,s}(1 + p_{m,cr}^{\beta} - \tau_{cr,m})}{1 - p_{m,cr}} \cdot (1 - p_m) + t_{cr,m} \text{for} p_m \geq p_{m,cr} \tag{A.8}$$

where $\tau_{cr,m}$ represent the critical shear stress for pure mud and β is a constant parameter set at 1.5 according to Van Ledden (2003).

Settling velocity and deposition
In contrary to the erosion process, the deposition rates for cohesive and non-cohesive sediments are calculated separately according to (Winterwerp, 1999) who found that this assumption is true when the mud concentration is lower than the 'gel point concentration' which is between 30-180 kg/m^3, which was not reached during the simulations of Bendoni (2015). Therefore, the deposition rates do not depend on the critical mud fraction. A significant difference between cohesive and non-cohesive sediments is the settling velocity. Beyond a certain concentration, mud particles tend to flocculate resulting in larger volumes and thus larger settling velocities. On the other hand, a larger concentration causes that settling flocs are hindered by each other, affecting the settling velocity negatively. In the *sand-mud-module*, the settling velocity of mud is determined according to the formulation by Cole and Miles (1983):

$$w_{s,m} = K_{w,m} C_m \tag{A.9}$$

where $K_{w,m}$ is an empirical constant with a value ranging from 0.001 to 0.002 [m/s per kgm^{-3}] and C_m is the depth-averaged mud concentration.

The deposition rate is then defined as follows:

$$D_m = w_{s,m} C_m \left(1 - \frac{\tau_b}{\tau_{dep}}\right) H_f \left(1 - \frac{\tau_b}{\tau_{dep}}\right) \tag{A.10}$$

in which τ_{dep} is a parameter for the critical shear stress below which mud can deposit (Krone, 1962). The deposition rate for mud is thus proportional to the concentration squared, whereas the settling velocity of non-cohesive sediment does not depend on the concentration and the deposition rate is proportional to the concentration to the first power.

The formulation for settling velocity implies that the settling velocity is proportional to the mud concentration for concentrations less than 5,000 mg/L. This linear relationship does not hold for higher mud concentrations, indicating that in the case of higher mud concentrations, a maximum settling velocity must be applied.

Bed shear stress
In contrary to the original XBeach model, the *sand-mud module* calculates erosion and sedimentation fluxes based on the bottom shear stress (τ_b). Also, for hydrodynamic and morphological computation, distinction is made between the determination of bottom shear stresses. Whereas in the hydrodynamic computation both skin friction and form drag are accounted for, in the morphological computation only skin friction is included.

The bed shear stress that is induced by currents and waves is calculated by means of Equation A.11.

$$\tau_b = \tau_w + \tau_c \left[1 + 1.2 \left(\frac{\tau_w}{\tau_c + \tau_w}\right)^{3.2}\right] \tag{A.11}$$

in which τ_w is the shear stress induced by waves:

$$\tau_w = \frac{1}{2} \rho f_w u_{rms}^2 \tag{A.12}$$

where the wave friction factor, f_w, is given by:

$$f_w = 1.39 \left(\frac{A_{orb}}{z_0}\right)^{-0.52} \tag{A.13}$$

A_{orb} is the amplitude of the orbital excursion of a particle which is defined as $A_{orb} = u_{rms} T_p / 2\pi$. T_p is the peak period and z_0 is the roughness related to the grains. τ_c is the shear stress related to the currents and is given by:

$$\tau_c = \rho C_D u_E^2 \tag{A.14}$$

with:

$$C_D = \left[\frac{\kappa}{ln(h/z_0) - 1} \right]^2 \tag{A.15}$$

in which $\kappa = 0.4$ is the Von Karman constant.

Vegetation
Apart from a cohesive sediment module, Bendoni (2015) also developed and implemented a vegetation module. Salt marsh coasts, and also mangrove coasts are subjected to erosion that is caused by both wave impact as shear stress. In this module, it is assumed that the vegetation only affects the critical shear stress of the soil and thus the soil erodibility.

B. Data analysis

In this appendix, the additional information about the data analysis is provided. Section B.1 shows the experimental set-up of the summer 2017 field trip. Information about the measurement instruments can be found in Section B.2. The processing of the raw data is extensively described in Section B.3. Furthermore, the calibration of the wave loggers is described in Section B.4 and the reliability analysis of the SED sensors in Section B.5. The offshore wave buoy data is presented in Section B.6. Finally, additional results from the summer and winter data are shown in Section B.7 and B.8, respectively. Note that in this appendix, original names for the instruments are used (apart from the experimental set-up). The conversion of names used during the analysis is presented in Table 4.1.

B.1 Experimental set-up

In this section the experimental set-up of the summer measurements is presented. The summer period is defined as the time interval between July 31st and August 10th, 2017. The positions of the installed instruments during the summer measurement are presented in Figure B.1. The offshore wave buoy is situated 2 km from the coastline (6.874533° S; 110.485117° E), at a water depth of 6 m.

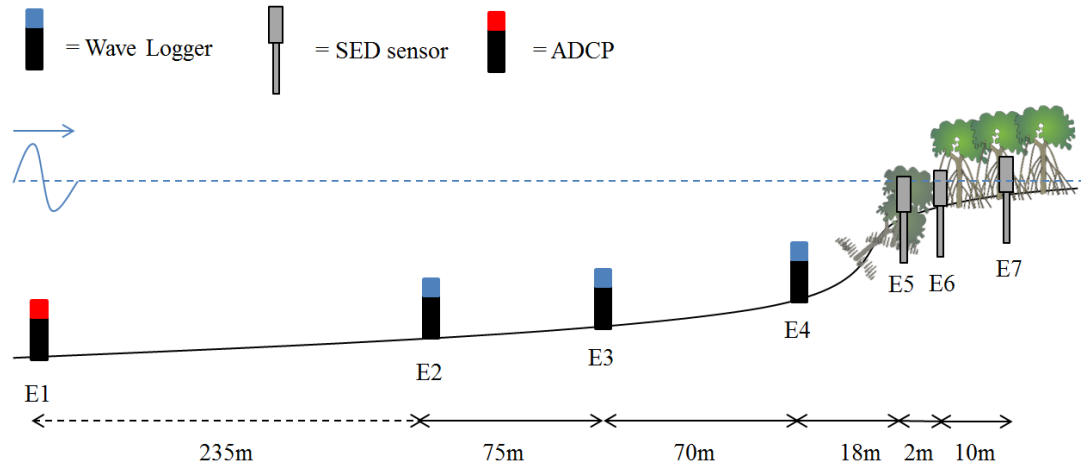

(a) Eroding transcect

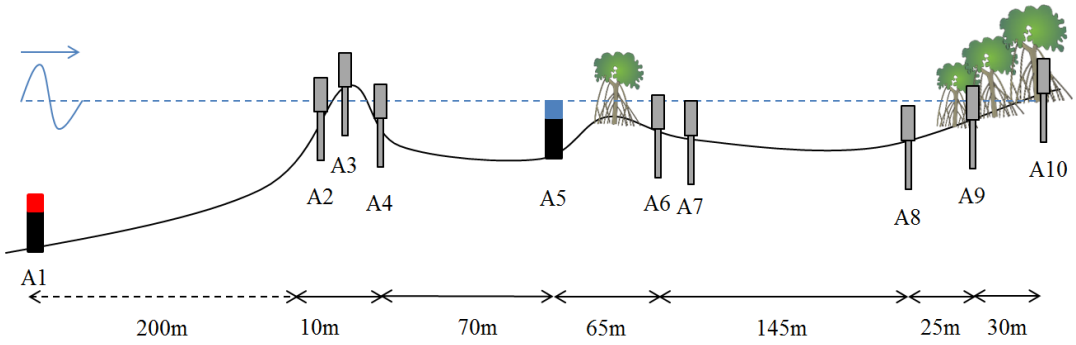

(b) Accreting transect

Figure B.1: Schematisations of the experimental set-up during summer measurements. Note that the schematisations are not on scale and only give a simplified impression of the actual bathymetries. Note also that the ADCP instruments are located at a relatively far distance from the rest of the instruments

B.2 Instruments

The type of instruments that were installed along the coastline transects are: OSSI Wave Gauge (Wave Logger), AquaDopp Current Profiler (ADCP) and SED sensors. In this section, the instruments are described in more detail. The ADCP data was not analysed and therefore not described here.

B.2.1 OSSI Wave Gauge

The Ocean Sensor Systems Wave Gauge (wave logger) was developed in order to measure liquid surface heights at a frequency up to 30 Hz (Systems). The pressure sensor of the wave logger is located on the bottom of the device and data is stored in units of bars.

During the measurements, the sensor was situated 20 cm above the bed. The data was stored at a frequency of 10 Hz. The measurement interval was set at *0*, which means that the device measures continuously.

An image of a wave logger that was used during the measurements is presented in Figure B.7.

B.2.2 SED Sensor

A SED (Surface Elevation Dynamics) sensor is a device that can be used to obtain bed level dynamics by means of light sensitive cells. The device is extensively described by Hu et al. (2015b).

The SED sensor measures the light intensity over 204 cells of 2 mm (see Figure B.2). At each measuring interval, the voltage profile along the measurement section (cell 1 to 191) is analysed in order to determine the bed level. How the raw data is converted into bed level data is described in a manual by Willemsen (2016).

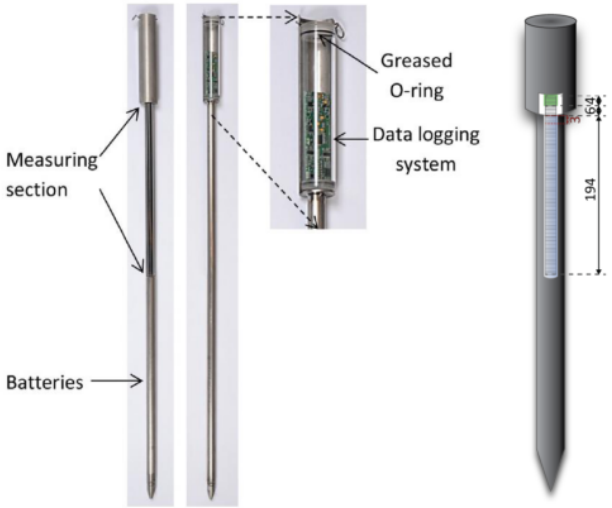

Figure B.2: From left to right: 1) front side of SED sensor, 2) back side of SED sensor, 3) enlarged data logging device (Hu et al., 2015b), 4) distribution of light sensitive cells. The measuring section contains 194 cells and the head 10 cells. The top 3 cells of the measuring section are influenced by the head and not used for collecting data.

In is important to note that the SED sensor only measures when it is light (during sun hours) and when it is emerged. In case the bed level is measured correctly, the voltage profile has the shape of an arctan function. At the location (cell number 1-194) where the voltage is larger than zero, the transition from bed to air occurs.

The SED sensors also contains a pressure sensor which can be used to determine liquid surface heights, similar as the wave logger. The pressure sensor was situated 20 cm above the bed. The pressure was measured continuously with intervals of 19.5 minutes in between which a short break of several seconds occurred. The SED sensor measured in intervals of 20 minutes.

B.3 Data processing

In this section the methods of converting pressure data into (spectral) wave parameters is described.

B.3.1 Wave logger pressure data

The raw pressure data collected by the wave loggers is saved in a different format than the pressure data from the SED sensors. The basic processing cycle is described here based on the wave logger files. The differences with the SED sensor files is clarified at the end of this section.

The raw pressure files are stored as 'WLOG.csv' files in which the collected pressures are presented in units bar.

burstWriter.m
First, these raw pressure files must be structured into burst intervals with the script 'burstWriter.m'. This script requires an interval length which is to be determined by the user. In order to calculate spectral wave parameters, this interval length lies usually between 10-20 minutes. For the sake of simplicity, it was chosen to have 100 intervals each day, which comes to an interval length of 14.39 minutes (= 863.4 seconds). Since the sample frequency is 10 Hz, this results in bursts of 8634 measurements. A file named 'finalbursts.csv' is written in which each column represents one burst.

AirPressureCorrection.m
One wave logger has been collecting air pressure data only, while it was hung up in a tree. The raw water pressure data files must be corrected with this air pressure. These are thus two separate 'finalbursts.csv' files.

In this script the air pressure file is named 'CorrFile'. The 'finalbursts.csv' file that has to be corrected is loaded as 'bursts'. The script assumes that the starting moment of both data collections is similar and determines until which moment there is an overlap (it could be that the air pressure file is longer). Then, the air pressure data is extracted from the bursts file. The pressure data corrected with air pressure is saved as 'bursts_correction.csv'. An example of an air pressure correction on the raw pressure data is presented in Figure B.3.

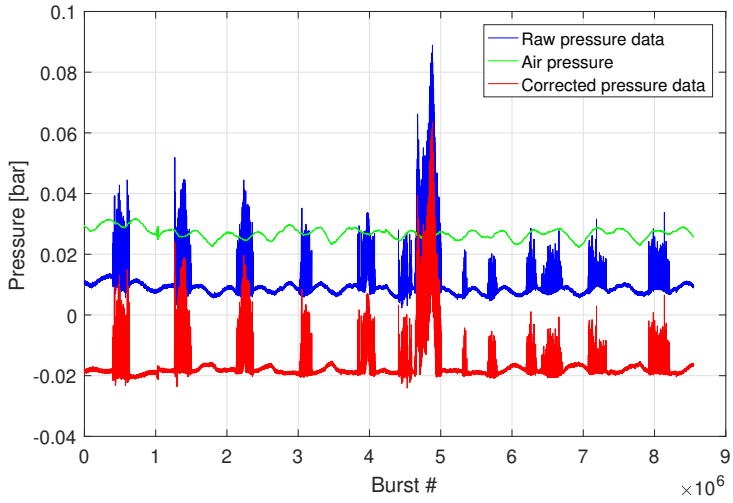

Figure B.3: Air correction applied at a raw pressure signal.

waterDepthCalculator.R
Next, the pressure is converted into values for water depth. Two versions of this script exist. One determines the air pressure itself and extracts this from the pressure data. When the air pressure is measured manually, this is not necessary. This adapted version (waterDepthCalculator-aircorrection.R) therefore skips the air correction part and calculates the water depth only. The required input values is the installationHeight.m (0.2 meters), the burst interval (863.4 seconds) and the sampling frequency (10 Hz). Also make sure that the activation date is correct. This script delivers three output files: 'waterDepth.csv', 'burstInfo.csv' and 'OSSIParameters.csv'. These will be used in the next step.

WaveAnalysis.m
In this script, the variations in water depth are converted into spectral wave parameters. This requires again a couple of input values. Make sure that the sampling frequency and installation height are correct. Because of the sensor height, the lowest measured water depth is in fact equal to the sensor height. Therefore, the water depths from the loaded 'waterDepth.csv' file must be added with the sensor height (0.2 m). It is important here to first check what the water depth time series looks like. For intertidal areas, each low water period will be represented by a horizontal line for which the pressure sensor is emerged. This horizontal line should be around 0.2m. When a wave logger is not emerged during the measurement period, make sure to know the bathymetry at this location. When the depth of the location around, for instance MSL is known, the water depth graph must be translated towards this value. The translation value is therefore not necessarily equal to the sensor height, since also offset of the instrument can play a part.

The applied corrections are presented in Table B.1.

Table B.1: Corrections applied to the measured water depths of the wave loggers

Wave logger	Correction [cm]
27	-33
41	-30
42	+10
43	-35
44	-40
45	+10

The output of this script is the 'neumeierOutput.csv' file. There is also a possibility to calculate the wave spectrum. To do so, adapt the following line: [parameters,names,**spect**] = wavesp(d, installationHeight.m, samplingFreq.Hz);

outputConcatinator.R
This script uses the 'neumeierOutput.csv' and 'burstInfo.csv' to determine time series of the spectral wave parameters. This is finally stored as 'waveParameters.csv'.

B.3.2 SED sensor pressure data

The correction that have been applied to the raw pressure data of the SED sensors is presented in Table B.2.

Table B.2: Corrections applied to the measured water depths of the SED sensors

SED	Correction raw pressure [bar]	Correction water depth [m]
175	-1 bar + 0.05	d - 0.05
177	-1 bar + 0.04	d + 0.05
178	-1 bar + 0.04	d + 0.12
180	-1 bar + 0.03	d - 0.05

B.3.3 SED sensor bed level data

The SED sensor bed level data is processed by means of a single MatLab script, which has been developed by Willemsen (2016).

The script does not need adaptations, so default settings were used (see Figure B.4). The start and end time of the measurement are determined automatically by reading the SED file.

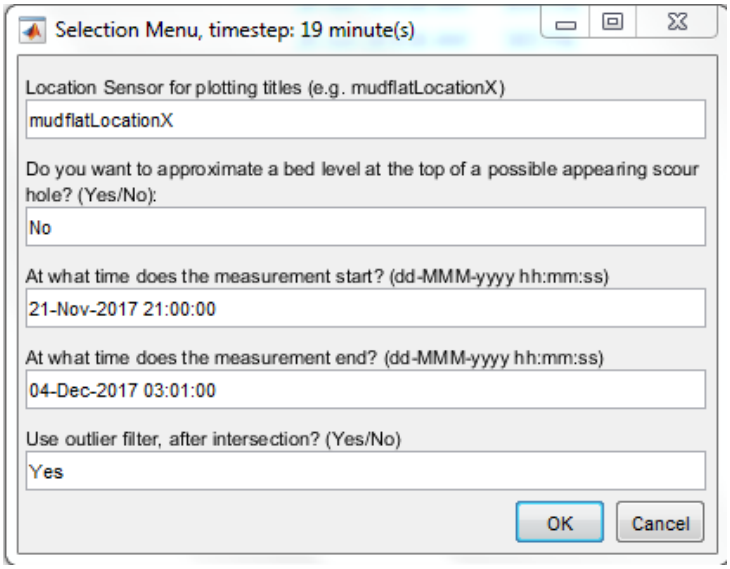

Figure B.4: Input screen for processing the SED sensor bed level data (Willemsen, 2016)

The script determines the bed level by means of the voltage profiles along the vertical measurement section, which is presented in Figure B.2. An example output of such a voltage profile is presented in Figure B.5 (Hu et al., 2015a). The cells covered by the bed give a low voltage (close to zero). The transition point represents the transition from bed level to air. The bed level is determined as the first cell at which the voltage reaches its maximum, i.e. when the voltage profile becomes vertical again.

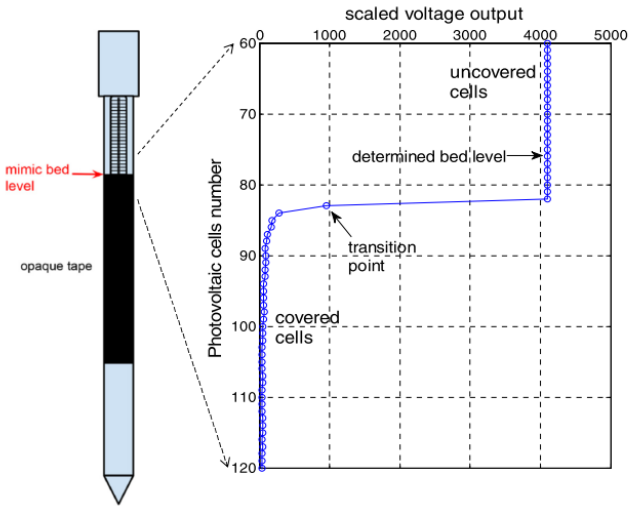

Figure B.5: Determination of bed level by means of the voltage output signal (Hu et al., 2015a).

B.4 Calibration wave loggers

This section describes the calibration measurements that were carried out with the wave loggers in order to determine the offset of the instruments. This was done two times: before and after the winter measurement period.

B.4.1 November calibration

On November 21^{st} 2017 a calibration was carried out to determine the initial offset of the instruments, before installing them in the field. The wave loggers were put into a box in the sea which was gradually filled until certain water depths (see Figure B.6). The water depths inside the box were measured and

compared with the water depths presented by the wave logger data. Table B.3 describes the water depths as measured in the box and by the wave logger. Three water depths were tested: T1, T2 and T3. After each depth measurement, the difference between the real water depth in the box and the measured water depth from the WL is presented. The values in the tables include an air pressure correction which was done by means of the waterDepthCalculator.R script by Greg Fivash (see Section B.3). It can be concluded that the offset of the wave logger instruments varies between 3-4 centimetres. This offset can be accepted as a minor error on the measurement results.

Figure B.6: Calibration of wave loggers before deployment. Photograph by Celine van Bijsterveldt, November 2017.

Table B.3: Calibration of clean wave loggers before deployment. Three water depths were tested: T1, T2 and T3.

WL	T1, box [cm]	T1, WL [cm]	ΔT1 [cm]	T2, box [cm]	T2, WL [cm]	ΔT2 [cm]	T3, box [cm]	T3, WL [cm]	ΔT3 [cm]	Δ_{tot} [cm]
27	44	41	-3	63	60	-3	36	33	-3	-3
29	45	41.5	-3.5	64	60.5	-3.5	35.5	32.5	-3	-3.3
41	46	42	-4	65	61	-4	35	32	-3	-3.7
42	46	-	-	65	-	-	35	-	-	-
43	45	42	-3	64	60	-4	35.5	32	-3.5	-3.5
44	44	43	-1	63	60	-3	36	33	-3	-2.3
45	46	-	-	65	-	-	35	-	-	-

B.4.2 March calibration

After the winter measurements, it appeared that some of the wave loggers were affected by barnacles. Barnacles are sea creatures which grow while attaching themselves to hard substrates. Figures B.7 and B.8 show a clean and a barnacle wave logger, respectively. Since the barnacles have grown on the bottom of the wave logger, where the pressure sensor is located, these creatures could have affected the measurements of the wave loggers. Therefore, a calibration was carried out to analyse the effect of these barnacles on the pressure signals.

Figure B.7: A clean wave logger. Photograph by Celine van Bijsterveldt, March 2018.

Figure B.8: A wave logger with barnacles. Photograph by Celine van Bijsterveldt, March 2018.

The calibration was carried out on March 2^{nd} in a similar way as the November calibration which was described earlier. The wave loggers have been put into a box, this time out of the sea, and the box was gradually filled with water. Three calibration measurements were carried out:

- Calibration with barnacles on WL 44, WL 43 and WL 42. WL 41 partly cleaned and WL 45 and WL 29 completely clean.
- Calibration with all clean wave loggers
- Calibration with clean sensors and socks over the instrument as protection measure

For each calibration, three water depths were applied: 10cm, 20cm, 30cm. During the second calibration in descending order. The analysis of this calibration is less detailed than that of the November calibration. Interest lies mainly in the effect of the barnacles on the pressure sensor from which a conclusion must be drawn whether the short- and long term sensitivity of the sensor is affected.

The results of the calibrations for a clean, accurate wave logger should look like Figure B.9. The three calibrations can be distinguished by the three peaks in the figure. Each peak has a stairs-like shape. The different steps in water depths are clear: from 10cm to 20cm to 30cm.

The effect of the barnacles can be observed from Figure B.10. It is clear the the barnacles have a significant effect on the pressure sensor. The pressure is overestimated by meters and the short term variability's are unclear.

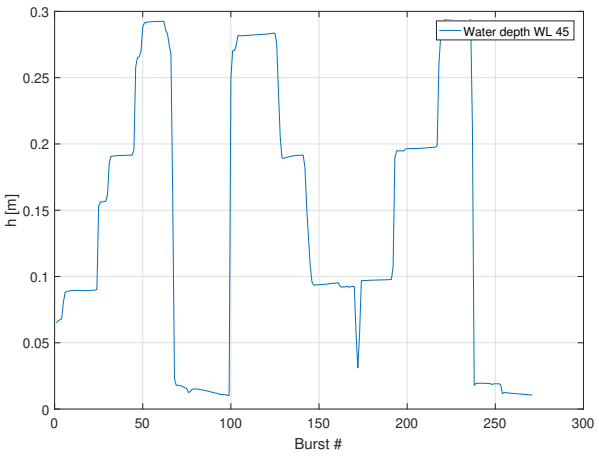

Figure B.9: Water depths during the calibration of WL 45 on 2 March 2018

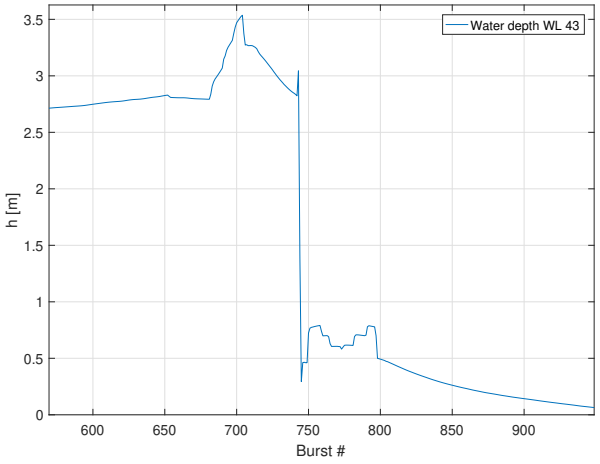

Figure B.10: Water depths during the calibration of WL 43 on 2 March 2018

B.4.3 Effect of barnacles on measurements

Figures B.11 and B.12 present the water depths (without offset and sensor height correction) of wave loggers 43 and 44, respectively. The additional pressure due to the barnacles can be seen clearly. At WL43, the irregularities already start soon after deployment. WL43 is therefore important in order to define the period that will be selected for the data analysis.

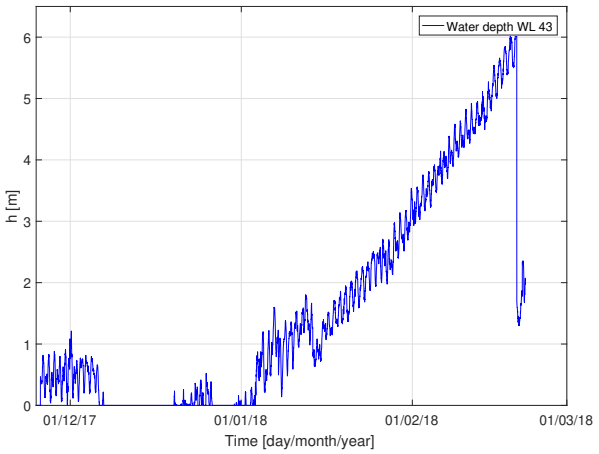

Figure B.11: Water depth time series of WL 43.

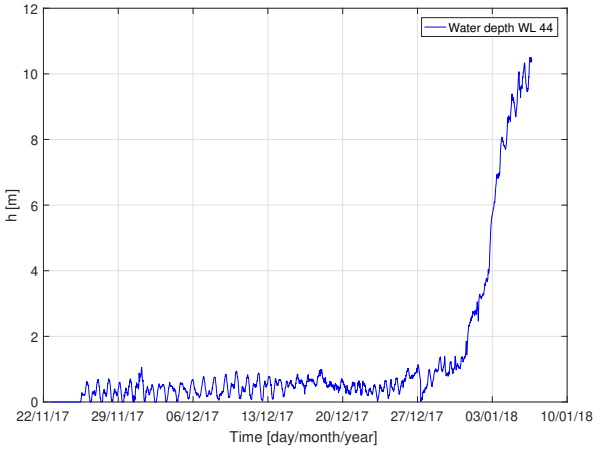

Figure B.12: Water depth time series of WL 44.

B.5 Reliability analysis SED sensors

During the collection of the SED sensors at the end of the winter measurement period, issues had seemed to occur with three instruments. The head of SED 179, containing the pressure sensor and batteries, was removed from its body. SED 180 was found back, lying horizontally beneath the surface. Lastly, SED 181 had possibly been moved during the measurement period since it was found back on a different location.

In Section B.5.1, the raw pressure data of these sensors is analysed in order to determine when each of the problems commenced after which it can be decided until which moment the data is still reliable. The same SED sensors showed remarkable results in terms of huge sedimentation events (see Section 5.2.6). In order to test whether these events are real bed level changes, the raw voltage data is analysed in Section B.5.2.

B.5.1 Raw pressure

In order to determine when each of the problems commenced, the HW events are counted which all represent a single day. The reference moment here is the storm event on 1 December (large peak on the left of the pressure graphs). The air pressure is approximately 1 bar. So, when the pressure sensors are emerged, the pressure should be around 1 bar. This is used as a reference. When the pressure data deviates too much from this reference point, it can be concluded that the pressure sensor is affected.

SED 179
Since the head of the SED sensors includes the pressure sensor and batteries, it can be expected that the pressure file is terminated when the instrument got decapitated. The pressure file stops around 20 December, as can be seen in Figure B.13.

Besides this, it can be seen that the pressure strongly increases after 30 November, just before the peak event on 1 December. This indicates that the pressure sensor is affected somehow and the pressure data from this moment forward is not useful. Since the measurements still continue, this is not the moment where the instrument got broken.

The bed level data shows clear measurement points and is assumed to be reliable until the moment of decapitation around 20 December 2017.

SED 180
SED 180 had been deployed at the seaward side of the chenier. Upon retrieval, the chenier had disappeared and the instrument was found lying horizontally 10 cm beneath the surface.

The pressure data of SED 180 is constant throughout the measurement period, except at the very end (around 12 January 2018) where it suddenly increases drastically (see Figure B.14). This is probably caused by the toppling over event.

Both the pressure and bed level data are assumed to be reliable until 12 January 2018.

SED 181
When SED 181 was retrieved, it was believed that it had been moved towards the seaward side of SED 180. Since the landmarks had all moved this is uncertain though. The coordinate system of the GPS device normally has an offset of maximum 10 m. Since the instrument was retrieved 20m from the initial deployment, it is believed that it has been moved manually. If the instrument had been moved, this should be visible from the pressure data.

The pressure data of SED 181 show a gradual increase around four days after deployment (see Figure B.15. This behaviour is similar to the gradual increase at SED 179 and is too gradual to be explained by someone moving the sensor.

Around 20 December (left red arrow) a sudden jump in pressure occurs. Around the beginning of February 2018 (right red arrow) a similar event occurs but now downwards. Both events could indicate that at these moments the instrument was moved.

Although it cannot be certain *if* SED 181 has been moved, it is assumed that the instrument is in any case not moved until around 20 December.

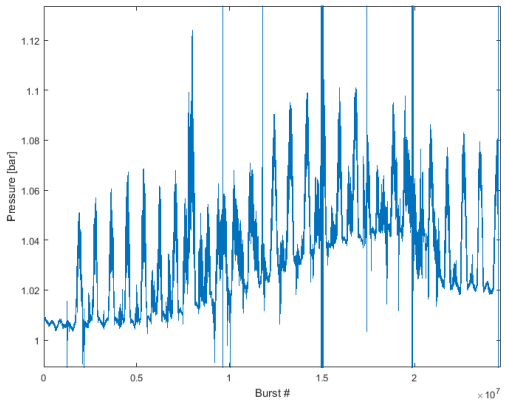

Figure B.13: Raw pressure data of SED 179 in bar.

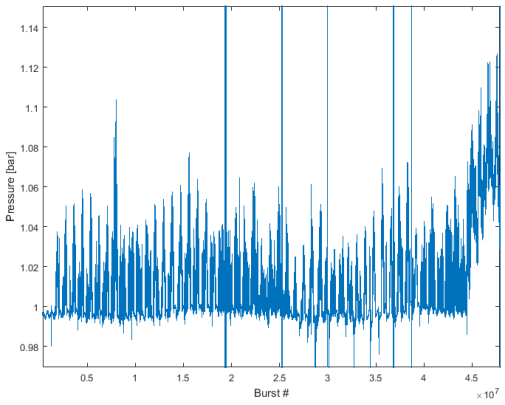

Figure B.14: Raw pressure data of SED 180 in bar.

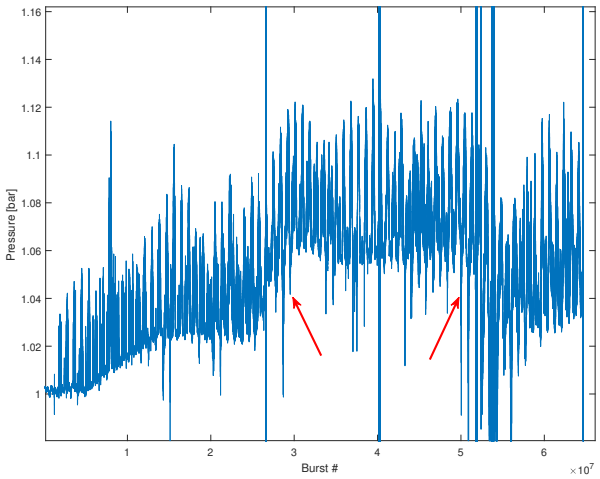

Figure B.15: Raw pressure data of SED 180 in bar. The red arrows point to sudden jumps in the pressure data.

B.5.2 Raw voltage profiles

In Section B.2 the SED sensor is explained in detail and the data processing is described in Section B.3.3. In this section, the raw voltage profiles of SED sensors 179, 180 and 181 are analysed at the moments in time when the large sedimentation events occurred. Based on the example of Figure B.5, the voltage profiles of the three SED sensors around the moment of the sedimentation events are plotted in order to analyse whether the peak event is indeed a result of bed level change, or that other processes may have caused the measurement peak.

Figures B.16, B.17 and B.18 show the voltage profiles of SED 179, 180 and 181, respectively. By plotting the voltage profile before a sedimentation peak and at the sedimentation peak, insight can be gained about whether a real sedimentation event occurred. The voltages of SED 179 and SED 181 show clear profiles that can be compared with Figure B.5. The bed level changes clearly and a real sedimentation event seems to occur. SED 180 seems to show unreliable results, looking at Figure B.17. Before the sedimentation peak, the voltage profile is clear. At the moment of the peak, light sensors 100-170 seem to be covered with something that prevents the light from coming into the sensors. Along the whole vertical, the voltage is much higher than zero, indicating that the sensor is not covered by the bed at all.

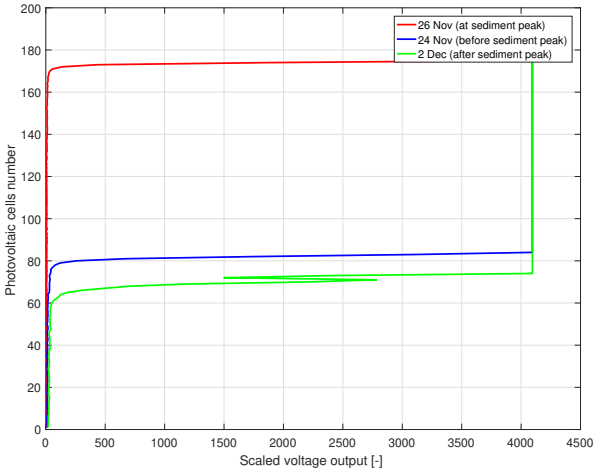

Figure B.16: Raw voltage profile of SED 179.

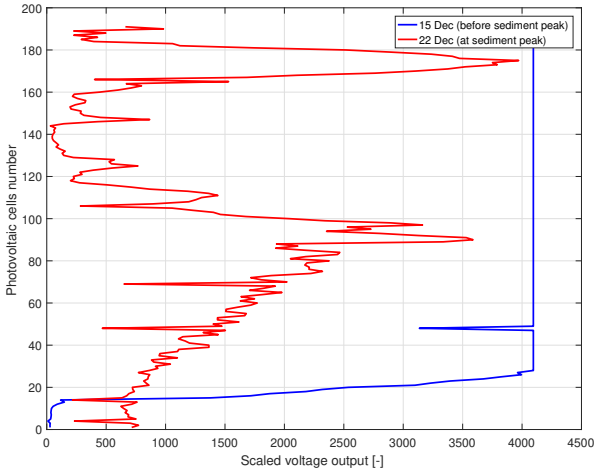

Figure B.17: Raw voltage profile of SED 180.

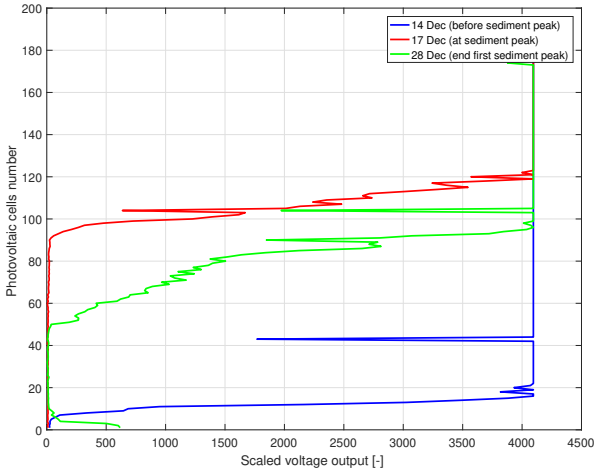

Figure B.18: Raw voltage profile of SED 181.

B.6 Offshore wave buoy

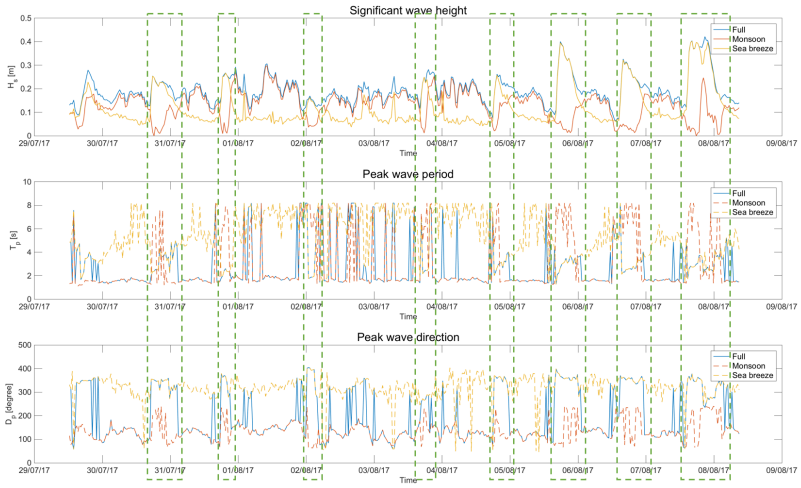

Figure B.19: Summer wave buoy data. Upper: significant wave height. Middle: peak wave period. Lower: wave direction. Courtesy of BioManCo (2018)

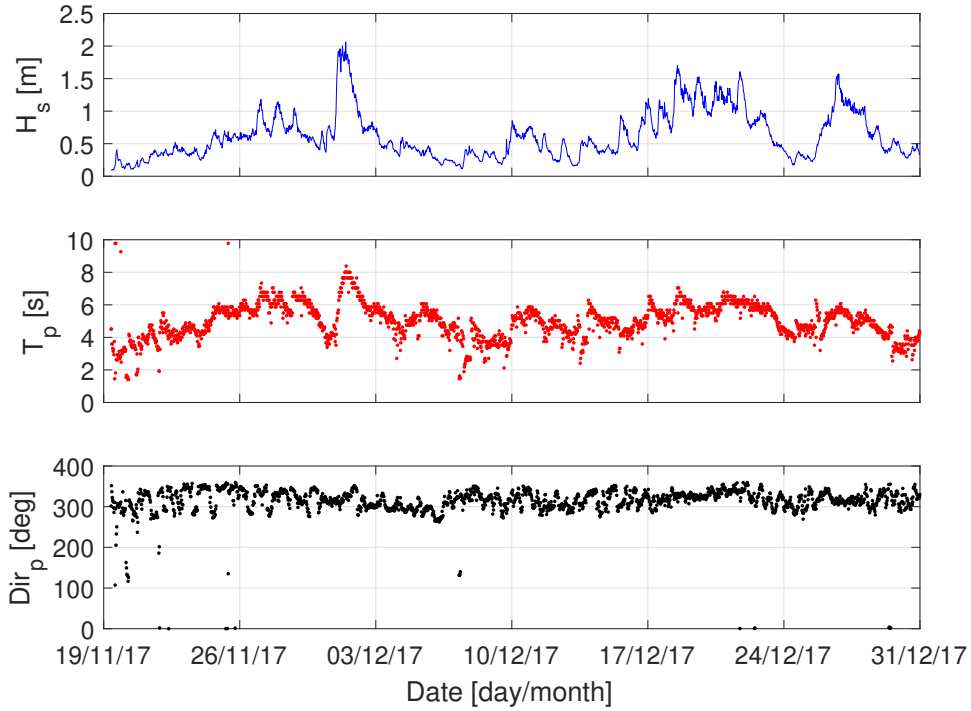

Figure B.20: Winter wave buoy data, 12km offshore. Upper: significant wave height. Middle: peak wave period. Lower: peak wave direction. Courtesy of BioManCo (2018)

B.7 Results summer period

This section presents the data collection of the summer measurement period which lasted from July 31st 2017 until August 10th, 2017. The results are presented briefly, since the focus lies mainly on the winter period. The plots presented here are from the *eroding transect* only.

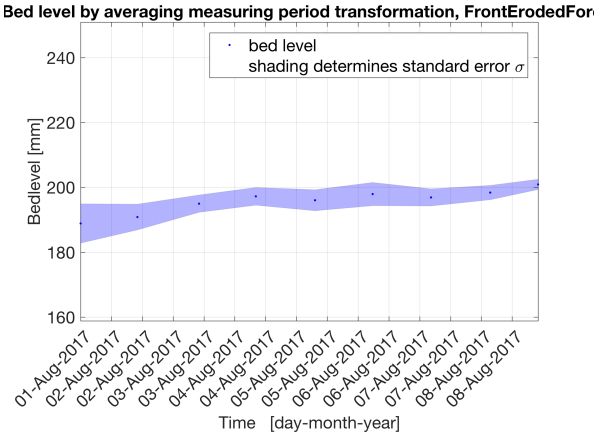

Figure B.21: Bed level development at SED 122

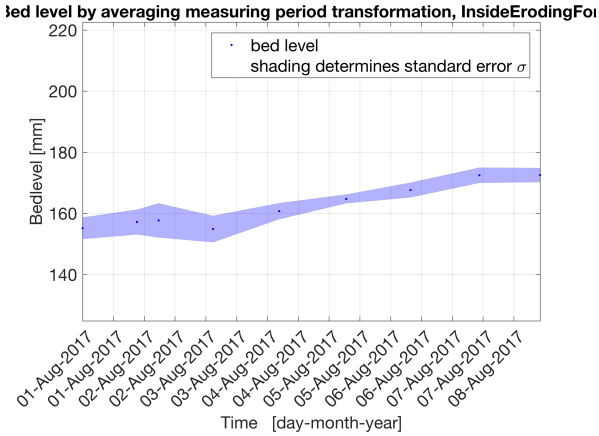

Figure B.22: Bed level development at SED 124

B.8 Results winter period

In this section, additional data measurements from the winter period (25 November 2017 12:00AM - 5 December 2017 12:00AM) are presented. Note that original instrument names are used here. The conversion to names that are used in the analysis can be found in Table 4.1.

B.8.1 Additional wave data

The wave measurements presented here did not qualify to include in the wave analysis since these instruments were to much affected by physical complications. This includes data from SED sensors SED 181 (Figure B.24) and SED 179 (Figure B.23).

Furthermore, note the irregularity of wave period measurements. The blank spaces represent the periods in which the peak wave periods were not measured accurately, resulting in outliers up to 200 seconds.

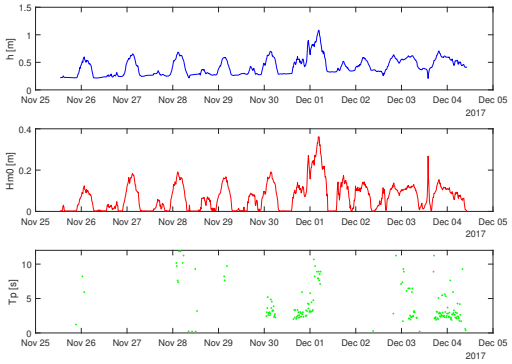

Figure B.23: SED 179. Water depth (h), spectral significant wave height (Hm0) and peak period (Tp)

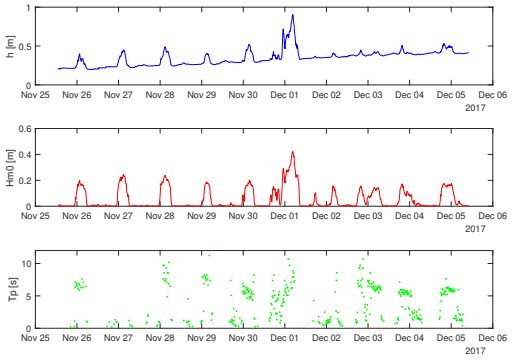

Figure B.24: SED 181. Water depth (h), spectral significant wave height (Hm0) and peak period (Tp)

B.8.2 Long term bed level changes (SED)

This section presents long term the bed level changes measured by the SED sensors.

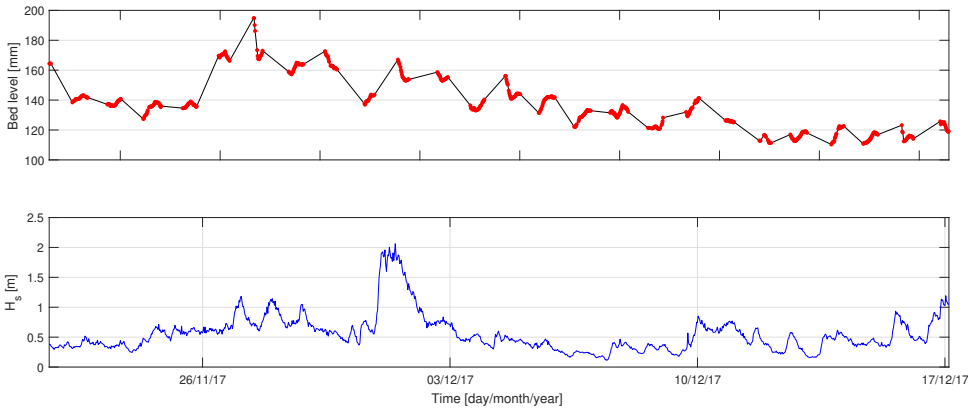

Figure B.25: Upper: Time series of bed level development at SED 174. Lower: Time series of offshore wave data.

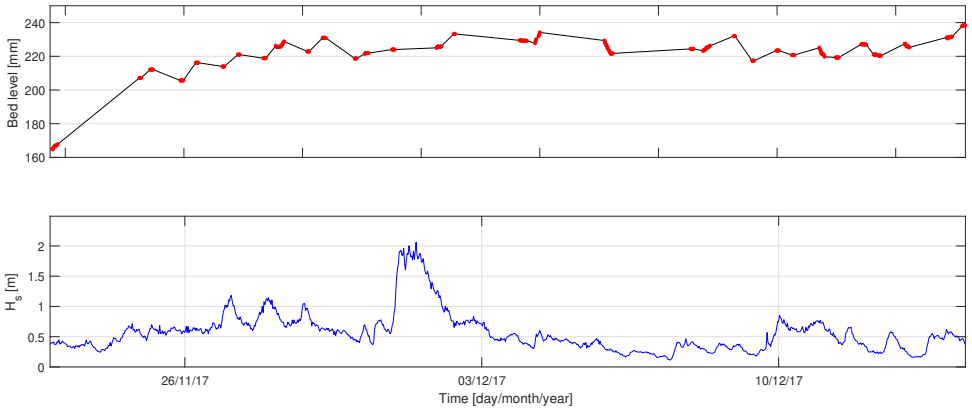

Figure B.26: Upper: Time series of bed level development at SED 175. Lower: Time series of offshore wave data.

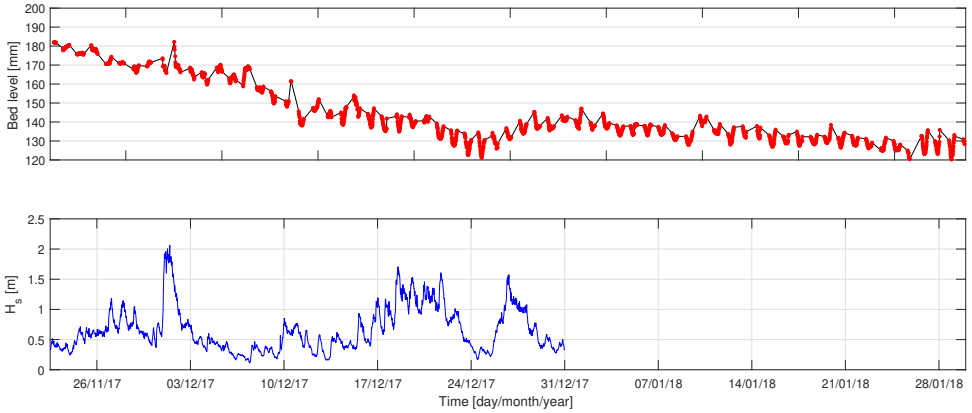

Figure B.27: Upper: Time series of bed level development at SED 176. Lower: Time series of offshore wave data.

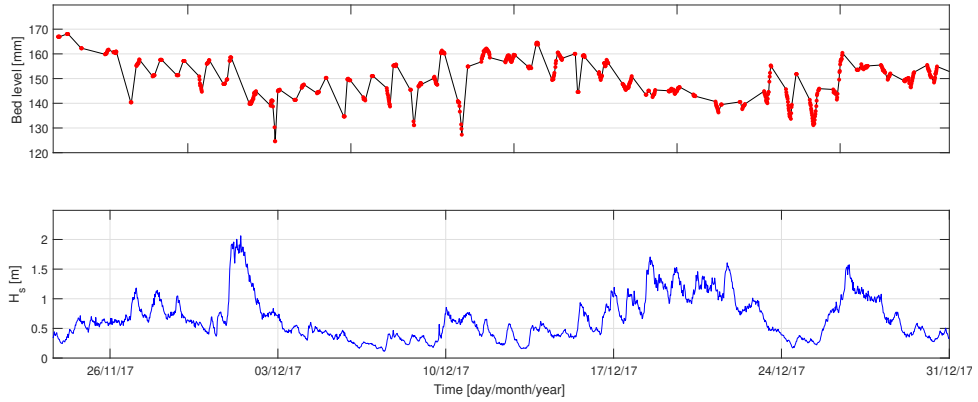

Figure B.28: Upper: Time series of bed level development at SED 177. Lower: Time series of offshore wave data.

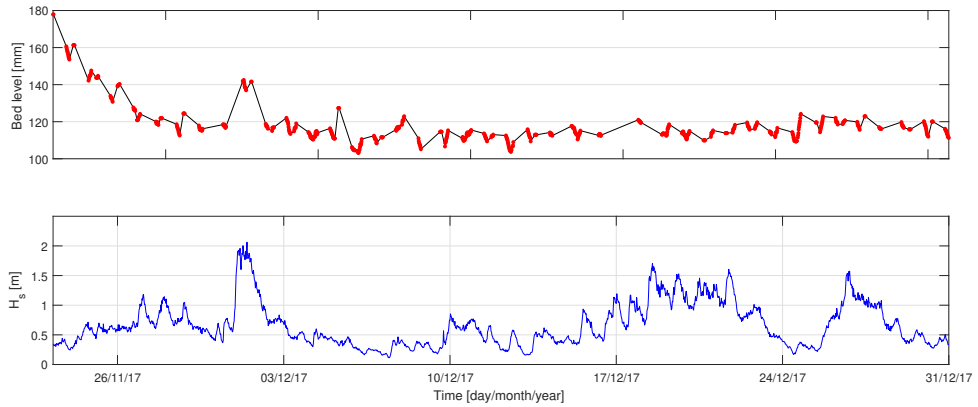

Figure B.29: Upper: Time series of bed level development at SED 178. Lower: Time series of offshore wave data.

B.9 Data analysis limitations

This section elaborates on limitations regarding the data analysis which are mainly the result of physical conditions and instrument limitations.

B.9.1 Physical complications

Looking at the wave data, various wave loggers were subject to the growth of barnacles on the pressure sensors due to which the sensor sensitivity got affected. Furthermore, the SED sensors that were deployed around the chenier in the accreting transect (SED 179, 180 and 181) all faced complications due to which the period of reliable measurements decreased significantly.

The bed level measurements have been collected by the SED sensors only. The physical conditions in the field largely determine the amount of bed level measurements that could have been collected. The sensor measures only if it is emerged and enough light is available (see Appendix B.2). Since the sensor measures in intervals, it could occur that during a measurement period, the sensor is flooded or it is dark outside so that no measurements are collected. In an intertidal area, this considerably affects the amount of collected data.

Moreover, due to the conditions on the intertidal area, instruments got emerged frequently. This clearly affected the calculated peak wave periods for which the amount of outliers increased significantly with the amount of time that the sensor was emerged. This resulted in a limited amount of reliable wave period data due to which average values have been used to calculate the wave friction coefficients in Section 5.2.3 and the bed shear stresses in Section 5.2.6

B.9.2 Instrument locations

The precise locations of the instruments have been determined by means of GPS instruments which can have an error of approximately 10 m, dependent on the signal reach (personal communication with Celine van Bijsterveldt).

C. Model set-up

This appendix includes additional information about the XBeach model that has been used for this research. Section C.1 describes the model set-up and the model validation is described in Section C.2.

C.1 XBeach model set-up

This section describes the model set-up and elaborates on the processes that are included in the model calculations. Also, formulations that are used for the calculations are described. Information is based on the content of the XBeach Manual (Deltares, 2015).

C.1.1 Coordinate system

A 1D cross-shore model was built. The model domain is a single gridline in which the computational x-axis is oriented perpendicular to the coastline and grids in y-direction are excluded. Directional spreading is ignored which leads to perpendicular waves towards the shore. This is assumed since the slope is very mild (1:600-1:1000) and it is likely that the waves have already refracted towards the shoreline before they enter the domain. Therefore, refraction inside the domain can be ignored by using a single directional bin instead of directional spreading. Furthermore, a grid size of 10 m is used.

C.1.2 Vegetation

The vegetation properties that are used in the model are determined based on calibration tests and do therefore not represent the real vegetation properties as present in the mangrove areas.

The vegetation is structured into three sections: roots (1), stem (2) and canopy (3). The corresponding parameters, based on Equation A.4, are presented in Table C.1.

Table C.1: Vegetation properties in the XBeach model.

Parameter	1	2	3
a_h	0.5	1.0	1.5
b_v	0.02	0.10	0.08
N	20	2	20
C_D	0.5	0.5	0.5

C.1.3 Boundary conditions

Four boundary conditions were applied in the model. One offshore boundary, two lateral boundaries and a landward boundary. These are described in this section. Wave and flow boundary conditions are applied at the offshore boundary.

C.1.3.1 Wave boundary conditions

For the wave boundary condition, a time series of Jonswap spectra is defined based on the spectral wave parameters H_{m0} and T_p that have been measured by the offshore wave buoy during the winter period (see Figure C.1). Table C.2 presents the parameters that are used to define the Jonswap spectrum.

Table C.2: Jonswap spectrum XBeach model.

Parameter	Value
$gammajsp$	3.3
s	100
$mainang$	270
$fnyq$	0.5

At the lateral boundaries, also a wave boundary condition is applied. For the surfbeat mode, Neumann leads to shadow zones in the groupiness (Deltares, 2015). To reduce this effect, the gradient along the wave crests of the wave energy can be set to zero, by means of *lateralwave = wavecrest*.

C.1.3.2 Flow boundary conditions

The tidal signal of the Semarang tidal station has been used for the considered time period (see lower plot of Figure C.1. The tide is implemented as a time series of water levels.

In order to let the offshore boundary pass through the generated waves and flows towards deep sea with minimal reflection, a weakly-reflective boundary condition is imposed. The parameter setting *abs1d* is a one-dimensional absorbing-generating boundary condition that allows for the specification of a time-varying water level while absorbing waves that propagate towards offshore (Deltares, 2015).

At the landward boundary, *back = wall*, is used, indicating no flux at this boundary.

The lateral boundaries of the model are the boundaries directed perpendicular to the coastline. In cross-shore direction, a certain water level distribution will develop due to the tidal forcing of the offshore boundary. This distribution must be met by the boundary conditions on the lateral sides. In this model, limited cross-shore extent can be expected, meaning that the alongshore gradient does not vary much. In order to let the model solve the the correct boundary solutions, Neumann conditions are applied at both lateral boundaries which imply that there are no gradients in both surface elevation and velocity in the alongshore direction.

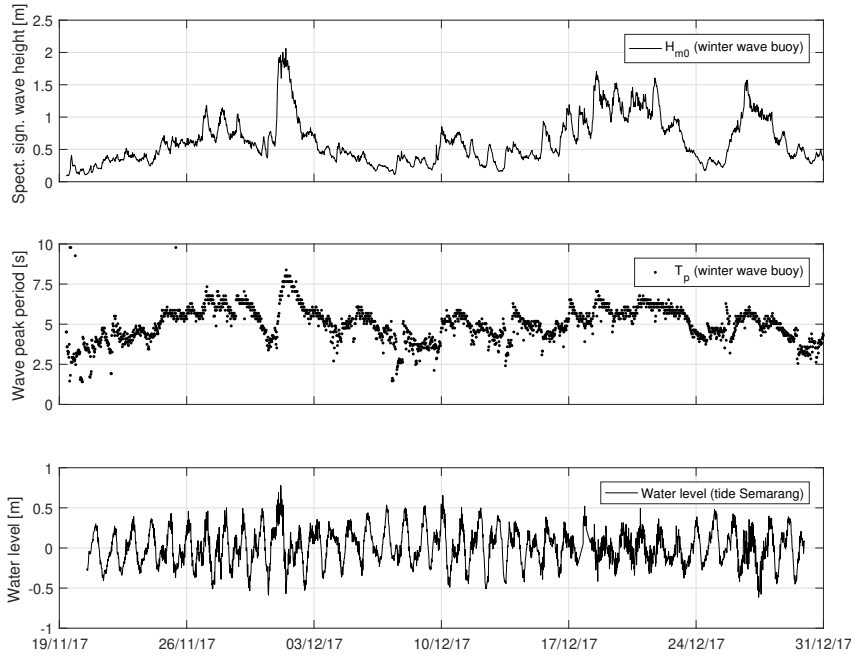

Figure C.1: Wave and tide boundary condition as a time series.

C.2 Model validation

In this section the model validation is described in detail. The focus here lies on explaining the method of the validation tests and interpreting the validation plots. Only the validation of the accreting transect is described here.

The model has been validated by comparing the outcomes of the spectral significant wave height, water depth and bed shear stress with the data analysis. Since the focus lies on the locations A6 and A7, at least the parameters on these locations must coincide with the field observations. Therefore, these locations are considered in this section.

The period over which the model outcomes and field observations are compared is similar to the measurement period that is used during the data analysis: 25 November 2017 - 5 December 2017.

A significant difference between the model and the data is the morphology. In reality, the morphology of the transects seems to change quickly due to its dynamic character. In the model, the morphology is fixed and does not change in time. Therefore, it can be expected that the differences between the model and the data become larger through time.

Another difference between the model and the data results is that XBeach works with H_{rms} whereas the data results are obtained with H_{m0}. Furthermore, the measurement interval of the data is around 15 minutes, whereas the output results of the model are filed each 5 minutes. Therefore, the model results are averaged with a 'moving mean' in order to obtain the average values over a time interval of 15 minutes, instead of 5 minutes. When calculating with the wave height, the model waves heights are corrected by dividing with 0.7 to obtain values representing H_{m0}. This way, the comparisons between the model and data results are similarly calculated.

C.2.1 Water depth

The correctness of the calculated water depth by the model depends on the bathymetry and the tidal signal that have been given as an input. Both possibly contain errors. By comparing the tidal signal at the measurement station of Semarang with the tidal signal observed in the data analysis, it can be concluded that this difference is negligible. Differences between model and data output for the water depth are thus probably the result of an error in the bathymetry data. Note that the minimum water depth from the data is 0.2 m +MSL, which is due to the distance between the sensor and the bed.

Since the model is 1D and groundwater flow is turned off, the water cannot escape during ebb because it is trapped by the chenier. Therefore, the water level inside the transect does not come below the height of the chenier with respect to MSL. This does not affect the occurring wave heights and shear stresses, but it causes that the minimum water depth calculated by the model is equal to the bed level at that location with respect to MSL. For A7 this is 0.21m, as can be seen in the upper plot Figure C.2. During HW, the model outcome is constantly a fraction larger. The difference varies between 5-10 cm. Between 26/11 and 30/11, the first small peak before HW is much larger for the model. This indicates that the bed level is in reality higher than in the model, which can possibly be related to sedimentation events.

The water depth validation at A6 is presented in the lower plot of Figure C.2. The bed level at location A6 is around -0.14 m +MSL which can be seen from the minimum water depth calculated by the model. The differences in water depth are less than for A7. The minimal differences in water depth will hardly affect the wave heights and shear stresses in which the most interest lies.

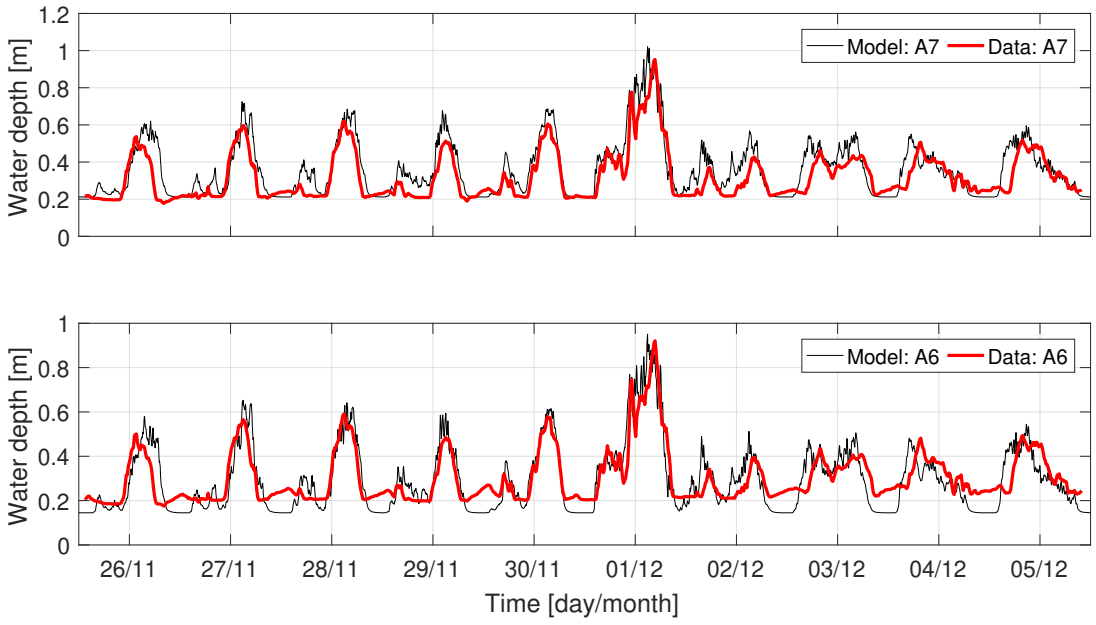

Figure C.2: Waterdepth validation in the accreting transect at A7 (upper) and A6 (lower).

C.2.2 Wave height

The wave heights at both A7 and A6 are very similar to the data measurements, as can be seen in Figure C.3. It can be seen that deviation between the model and data results starts after the storm event on 1 December. The data results start to become slightly larger, even though the data water depths become lower than the model results in this period. However, the differences remain minimal and within acceptable range.

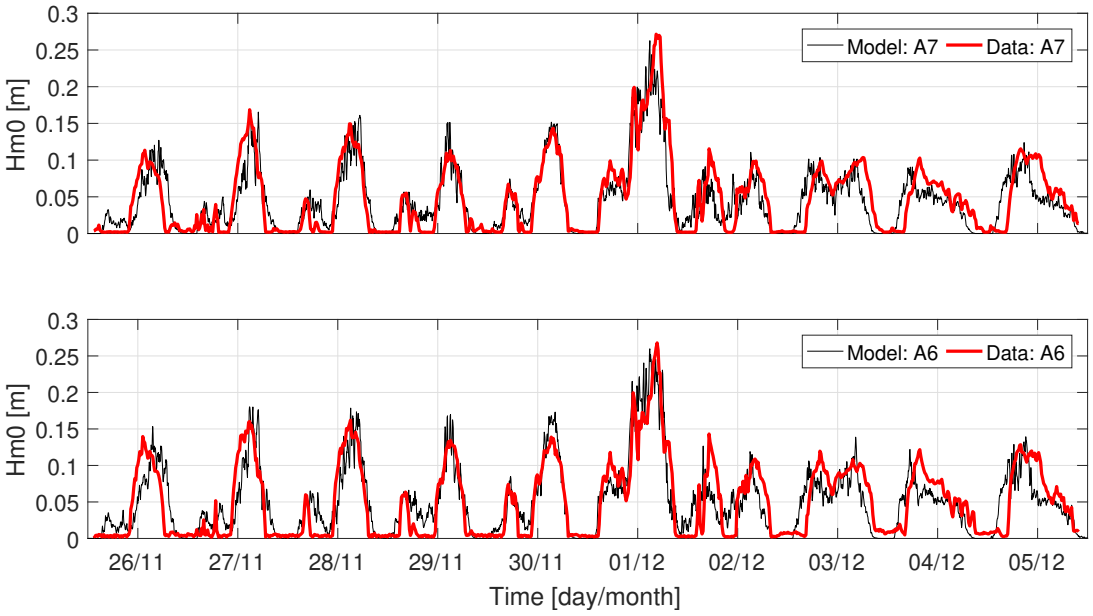

Figure C.3: Waveheight validation in the accreting transect at A7 (upper) and A6 (lower).

C.2.3 Bed shear stress

Xbeach calculates the bed shear stresses by means of Equation A.2. In order to obtain the bed shear stresses from the data results, Equation A.2 has been adapted to an easier formulation, presented by Equation C.1. In this equation, the dimensionless bed friction coefficient (c_f) is calculated based on the Manning bed roughness coefficient (n). For mud, a value of $n = 0.012$ is used.

$$\tau_b = \rho c_f u_0^2 \tag{C.1a}$$

$$c_f = \frac{g n^2}{h^{(\frac{1}{3})}} \tag{C.1b}$$

The comparisons in shear stresses of A7 and A6 are presented in Figure C.4.

At the locations where the water depths or wave heights deviate relatively much from the data results, it can be expected that the same holds for the computed shear stresses at these locations. The shear stresses at A7 are slightly underestimated by the model after 1 December, as can be seen in Figure C.4. At these locations, the model overestimates the water depths, and since the wave heights are approximately equal, this causes lower shear stresses. The difference in water depth is especially large at the first peak after the 1 December storm event. The water depth is here overestimated with around 15 cm, resulting in much larger shear stresses.

At this same moment in time, the deviation in shear stress is even larger at A6. The model here underestimates both the water depth and the wave height, resulting in a large difference between the model and data results here.

On average, the model results slightly underestimate the occurring shear stresses compared to the data results. The changes in bathymetry probably have a large effect on this difference. It can be seen that mainly after the big storm event, the differences become substantial.

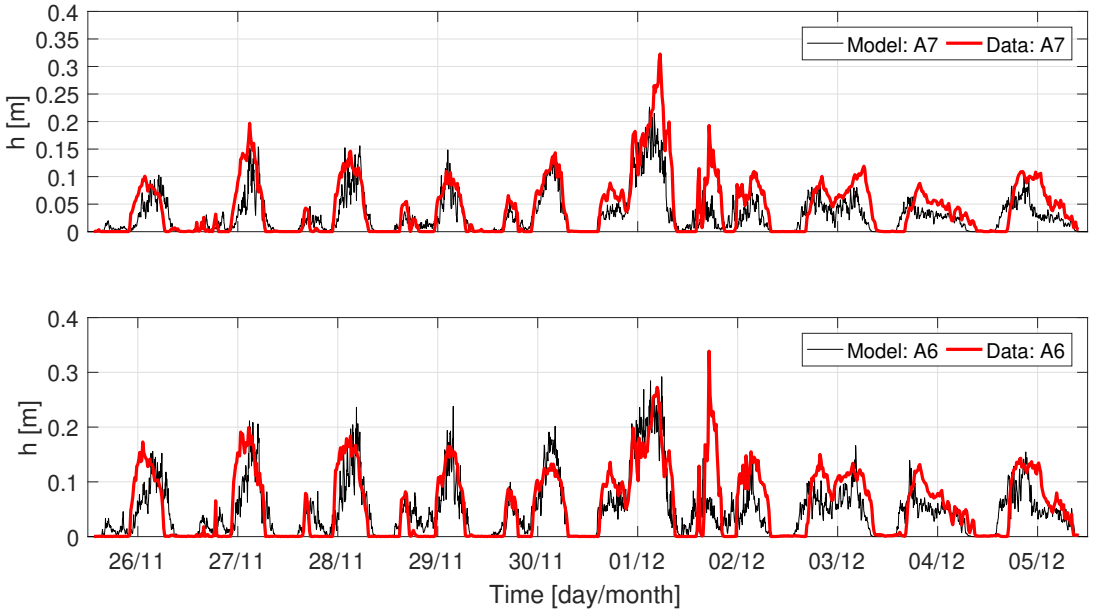

Figure C.4: Bed shear stress validation in the accreting transect at A7 (upper) and A6 (lower).

C.3 Model limitations

This section describes model limitations that might have affected the reliability of the model results. It is assumed that the limitations described here have a minor effect on the reliability of the conclusions of this research.

C.3.1 Phase-averaging approach

By using the phase-averaging approach for calculating hydrodynamics, wave calculations are carried out on a wave group scale. With each calculation, the initial wave height and wave period are used to determine the short wave energy after which the dispersion relation is used in combination with the wave action balance (see Equation A.1) to calculate the propagation of the waves towards the shore, so that the wave period remains the same along the modelled profile (Deltares, 2015). During the data analysis, it was found that the wave period *does* change along the profile, mainly due to the non-hydrostatic effects of wave breaking (decreasing wave period) and vegetation (increasing wave period), which indicates a limitation of the model in terms of simulated hydrodynamics along the transects. This affects the calculated shear stresses which depend on the wave period.

C.3.2 Bathymetry

The model results are highly sensitive to changes in the bathymetry profile, as was seen in Section 4.2.3. Since the morphology at the coastal zone of Demak is very dynamic, the bathymetry changes rapidly (see Section 5.2.6). Even though the modelled time period in this research comprised about 40 days, this may have caused significant bed level changes due to which the exact hydrodynamic outcomes of the model may not be representative to the real situation. Since the focus mainly lied on a qualitative analysis about the effects of cheniers on the hydrodynamics, this limitation is negligible.

C.3.3 Bottom friction

In XBeach it is not possible to model different values for the bottom roughness along a profile. Since grain sizes have been found to vary strongly on a local scale along the transect, the value for Manning deviates as well. For simplicity it has been chosen to use $n = 0.012$ which is representative for mud. For calculations of the shear stresses along cheniers, which consist of fine sand, $n = 0.015$ has been applied. This causes that the calculated shear stresses along the profiles might deviate from reality. In case of $H_{m0} = 0.4$ m, $T_p = 6$ s and $h = 1$ m, τ_b varies between 0.25 N/m^2 and 0.39 N/m^2 for the mud and sand friction coefficient, respectively. It should be noted though that with higher Manning values, the critical shear stress for erosion also increases. Furthermore, in contrast to the data analysis, the modelled wave-induced shear stresses are calculated by means of H_{rms} with an output interval of 5 minutes. Additionally, the modelled shear stresses also include current-induced shear stresses, in contrast to the wave-induced shear stresses from the data analysis. However, since the tidal current velocities are small (see Appendix D.1) and the modelled shear stresses were quite accurately validated with the bed shear stresses from the data analysis (which are wave-induced only) (see Section 4.2.4), it is expected that the addition of currents does not affect the modelled shear stresses significantly.

C.4 Additional model results

This section presents additional model results that were not included in the main report. Figure C.5 shows the results of the simulated scenarios for the accreting transect, including a situation without chenier and vegetation patch, so no protection at all.

Figure C.6 presents the simulations of the scenarios for the eroding transect, including a situation without chenier.

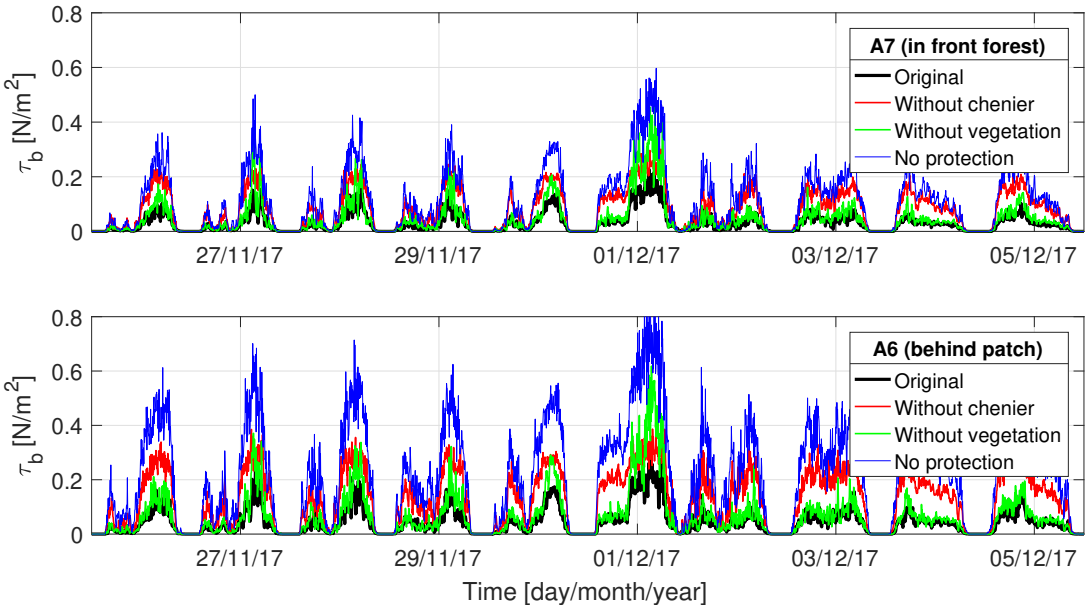

Figure C.5: Wave-induced shear stresses at E7 (upper) and E6 (lower) in the accreting transect, for various situations. Situation without any protection included

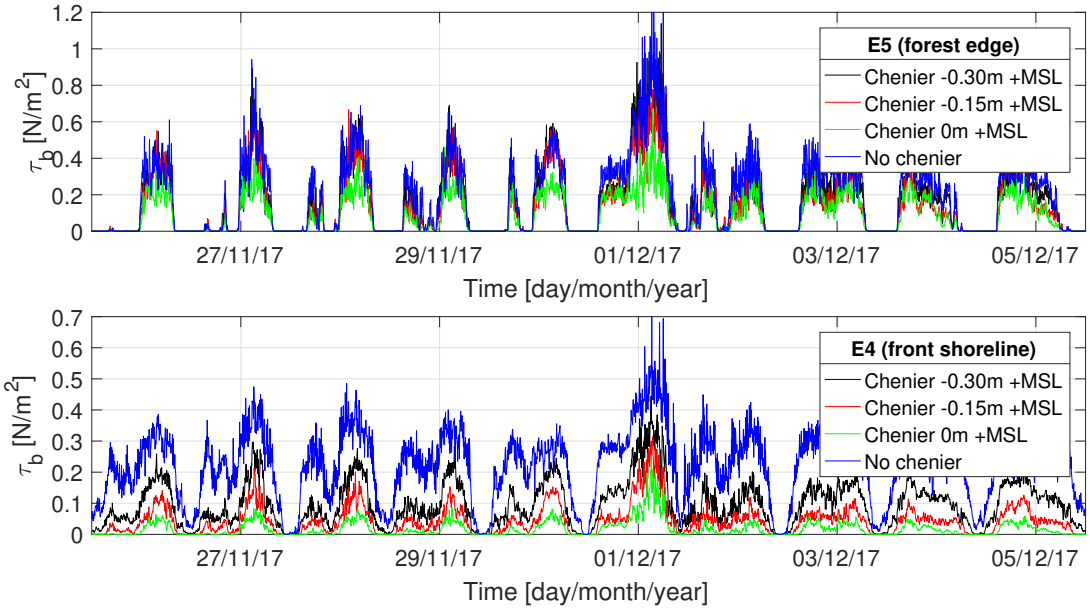

Figure C.6: Wave-induced bed shear stresses at locations E5 (upper) and E4 (lower) in the eroding transect, for various scenarios. Situation without chenier included.

D. Area characteristics

This appendix includes information about the area of Demak. The influence of the tide is described in Section D.1, the sediment composition in Section D.2 and the bathymetry in Section D.3. Section D.4 elaborates on the mangrove species in the Demak area.

D.1 Tide

The water level at the coastline of Demak is influenced by the tide. The tidal signal is dependent on the geographical location of Demak and is described first. Next, the effect of meteorological conditions on the average water level is described.

D.1.1 Tidal constituents

From the tidal constituents presented in Table D.1, the form factor, $F = (K_1 + O_1)/(M_2 + S_2)$, can be obtained. The tide in Demak has a form factor of 2.4, which refers to a mixed tidal signal with dominant diurnal characteristics and small semi-diurnal components. An example of the corresponding tidal signal is plotted in Figure D.1, showing a irregular periodicity and daily inequalities (Smits, 2016). The tidal signal also shows the neap-spring tidal cycle with tidal ranges varying between approximately 0.4 and 0.6 m. With these properties the tidal signal can be characterised as a micro-tidal regime (Bosboom and Stive, 2015).

Table D.1: Tidal constituents at Demak

Tidal constituent	Amplitude [cm]	Phase [deg]
S_0	95.44	-
M_2	7.57	541
S_2	5.93	124
N_2	2.03	440
K_2	1.36	124
K_1	21.41	-32
O_1	11.08	852
P_1	7.07	-32
M_4	0.61	760
MS_4	1.40	321

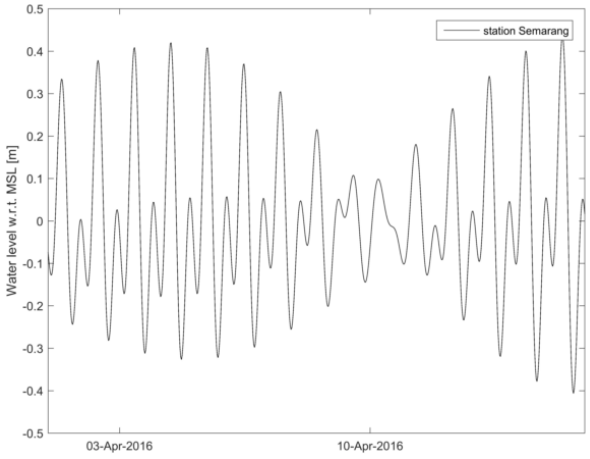

Figure D.1: Tidal signal at a measuring station in Semarang, near Demak (Smits, 2016)

The maximum tidal currents that correspond to the tidal signal are in the order of 15 cm/s (EcoShape,

2015). The bottom shear stress due to currents only can be calculated with Equation D.1.

$$\tau_b = \rho c_f |\bar{U}| \bar{U} \tag{D.1}$$

where c_f is a dimensionless friction coefficient that relates to the Chézy coefficient by $c_f = g/C^2$. For muddy environments, Chézy coefficients around 90 $m^{1/2}/s$ have been found (Winterwerp and Kesteren, 2004). For a current of 15 cm/s, this comes to a bed shear stress of $\tau_b \approx 0.03$ Nm^{-2}.

D.1.2 Seasonal variation of the average water level

The average water level at the Demak coastline is not only determined by tidal forcing. Meteorological conditions play a part as well, which are not included in the tidal constituents that determine the tidal signal. In order to gain insight into the seasonal variability of the average water level, the measured tidal signal at the Semarang station was analysed for the years 2014 until and including 2017.

Figure D.2 presents a moving mean on a monthly scale along the harmonic tidal signal of Semarang. This trendline shows a fluctuation of the average water level throughout the year with an amplitude of 5 centimetres.

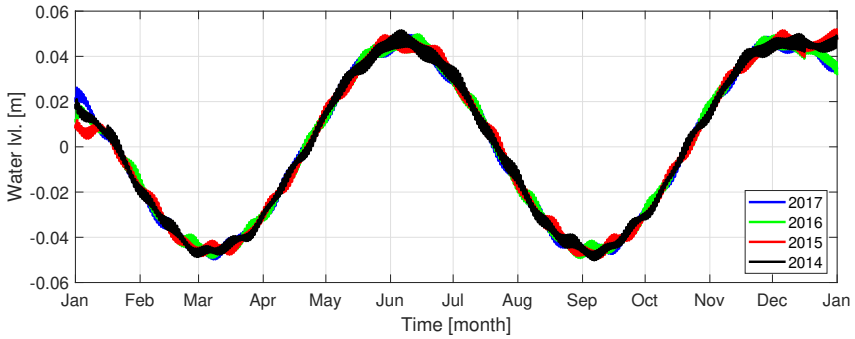

Figure D.2: Monthly moving mean of the harmonic tidal signal at the Semarang tidal station.

A similar trend is observed by plotting the *measured* absolute values of the water level at the tidal station of Semarang, as can be seen in Figure D.3. In contrast to the harmonic tidal signal, Figure D.3 shows that the two minima and maxima have a deviating value. The minimum average water level in September is higher than the minimum average water level in March.

Despite the difference between Figure D.2 and D.3, it can be observed that the average water level shows a two-yearly peak period between October-January and May-July/August. Between February-May and August-September the water levels are relatively low. The lowest water levels seem to occur between February and May. In 2014, the difference in average water level between March and October is around 30 centimetres. In 2017, this difference is 10 centimetres, but this year, the highest water level occurs much later, in December, where the difference with March increased to 20 centimetres. Thus, the contrast between average water levels throughout a year seems to vary each year and the moment at which the water levels are highest varies slightly as well. Nevertheless, a clear seasonal trend of the average water level can be observed.

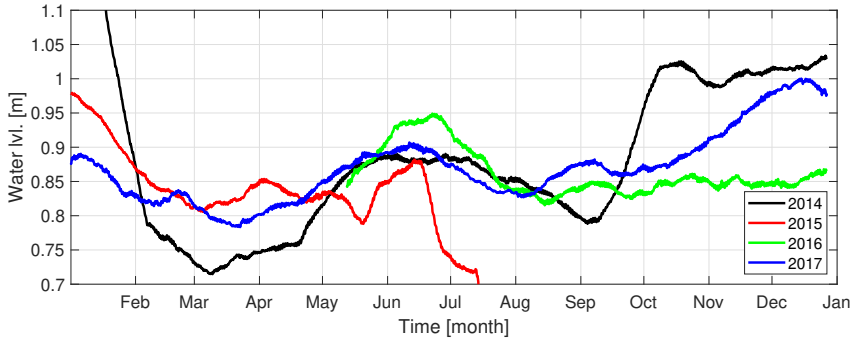

Figure D.3: Monthly average of the absolute water levels measured at the Semarang tidal station for the years 2014, 2015, 2016 and 2017 (IOC, 2018). Empty spaces (in 2015 and 2016) are due to unavailability of data.

Figure D.4 shows the harmonic tidal signal during the month March in 2017. This signal can be used to determine whether a long enough inundation-free period can occur during this month in order to allow for mangrove colonisation according to Balke et al. (2011). In order to acquire a 5 day inundation-free period, a location must be situated at least 10 cm above MSL, as can be seen in Figure D.4.

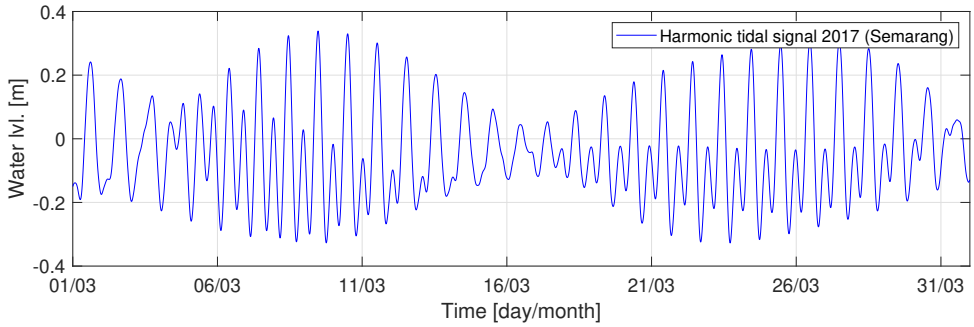

Figure D.4: Harmonic tidal signal in March 2017 at the tidal station of Semarang.

D.2 Sediment composition

Sediment samples were taken in the field by BioManCo (2018) and analysed by means of a laboratory experiment by BioManCo et al. (2018). The grain sizes of the locations were instruments were deployed are presented in Table D.2.

Table D.2: Sediment grainsize per location. The instruments are sorted, starting at the accreting transect with A1 in the left column until A9 in the right column. The remainder of the right column represents the eroding transect. For the visualisation of the locations is referred to Figure 4.1

Location	D_{50} [μm]	Location	D_{50} [μm]
A1 (WL 45)	13.94	A9 (SED 175)	6.42
A2 (SED 180)	12.47	E1 (WL 43)	24.54
A3 (SED 181)	145.22	E2 (WL 44)	32.95
A5 (WL 42)	10.68	E3 (WL 41)	57.61
A6 (SED 178)	27.05	E4 (WL 27)	9.95
A7 (SED 174)	7.35	E5 (SED 176)	7.00
A8 (SED 177)	7.28	E6 (SED 124)	9.59

At the chenier a bulk density of 1580 kg/m^3 and a dry density of 1080 kg/m^3 was found. A regular muddy sample has a bulk density of 1390 kg/m^3 and a dry density of 585 kg/m^3.

By means of Malvern tests, the grain size distribution of mud samples were determined. This gives

information about how the mass of the sediment is distributed over a range of particle diameters. On average, 80% of the mass has a particle diameter below 63μm. Approximately 20-30% of the mass consists of fine sand.

D.3 Bathymetry

In this section, the bathymetry that is used during the data analysis and the modelling is presented. The bathymetry is based on the winter period. The bathymetry of the summer period has not been used during this research, so is not presented here.

Table D.3 presents the bathymetry data that was measured during deployment of the instruments at the beginning of the winter measurement period (BioManCo, 2018). The column 'measured depth' contains several empty spots. During the measurements, these locations were dry, so no water depth could be measured. To obtain these results, the water depth time series from the data analysis is used. For the wave loggers one moment in time was chosen (25 November 14:20PM) at which the tidal cycle was at MSL, so the water level equal to +0m MSL. The water depth observed at this moment is equal to the bed level compared to MSL. For the SED sensors another moment was chosen. The highest water level at 26 November coincides with a water level of +0.34m MSL. So, the highest water depths at 26 November are extracted with 0.34m to obtain the bed level compared to MSL.

For the sake of simplicity not only the empty spots of Table D.3 were determined this way, but also the already known water depths. These lie close together, but it is assumed that it is more reliable to obtain the whole bathymetry with the same method. The resulting bathymetries for the transects are presented in Table D.4. Only for SED 124 the water depths were not measured, so this value is based on assuming a landward slope of 1:1000.

Table D.3: Bathymetry measurement from the winter period. The measured depth is calibrated with the tidal signal measured at the Semarang station.

Location	Date time (UTC)	Local date time (+7 UTC)	Tide Semarang (+/- MSL) [cm]	Measured depth [cm]	Measured depth (+/- MSL) [cm]
WL42	21-11-17 01:39	21-11-17 08:39	-34	-	-
WL45	21-11-17 02:27	21-11-17 09:27	-35	72	-107
SED175	22-11-17 07:29	22-11-17 14:29	-11	-	
SED177	22-11-17 07:37	22-11-17 14:37	-10	-	
SED174	22-11-17 07:42	22-11-17 14:42	-10	7	-17
SED178	22-11-17 23:49	23-11-17 06:49	-9	9	-18
SED179	23-11-17 00:07	23-11-17 07:07	-8	9	-17
SED180	23-11-17 00:17	23-11-17 07:17	-6	-	
SED181	23-11-17 00:21	23-11-17 07:21	-7	1	-8
SED176	23-11-17 06:26	23-11-17 13:26	-16	-	
SED124	23-11-17 06:26	23-11-17 13:26	-16	-	
WL44	25-11-17 05:09	25-11-17 12:09	-21	29	-50
WL41	25-11-17 05:30	25-11-17 12:30	-21	18	-39
WL27	25-11-17 05:45	25-11-17 12:45	-20	32.5	-52.5
WL43	25-11-17 07:19	25-11-17 14:19	0	125	-125

Table D.4: Bathymetries of both transects. The data presented in this table is extracted from the water depth measurements during the winter period. Note that the depth of SED 124 is based on an assumption and therefore presented between brackets.

Eroding		**Accreting**	
Location	Depth [cm +MSL]	Location	Depth [cm +MSL]
E1 (WL 43)	-125	A1 (WL 45)	-122
E2 (WL 44)	-48	A2 (SED 181)	-6
E3 (WL 41)	-39	A3 (SED 180)	-12
E4 (WL 27)	-48.5	A4 (SED 179)	-26
E5 (SED 176)	5	A5 (WL 42)	-24
E6 (SED 124)	(6)	A6 (SED 178)	-14
		A7 (SED 174)	-21
		A8 (SED 177)	-13
		A9 (SED 175)	-10

D.4 Mangrove species

The most dominant mangrove species in the Demak area are *Avicennia marina* and *Rhizophora mucronata* (EcoShape, 2015). *Avicennia marina* is a pioneer specie and together with *Avicennia alba* (a family member) these are the most important pioneer species in the area. In order to achieve mangrove re-establishment, their colonisation behaviour is important to understand. Especially, the fruiting seasons.

Various theories exist about the fruiting seasons of these mangrove species. Kitamura (1997) investigated mangrove species at Bali (Indonesia) and found that *Avicennia marina* has its fruiting season between December and February. Other studies showed that in Malaysia, the *Avicennia marina* fruits between June and August and *Avicennia alba* between July and September (Faridah-Hanum and Latiff, 2014).

Although not investigated in detail, observations by BioManCo (2018) suggest that in the Demak area, *Avicennia marina* establishes during the south-east monsoon period whereas *Avicennia alba* establishes mainly during the north-west monsoon period. The observations of BioManCo (2018) are used as a reference for this research regarding fruiting seasons of mangrove species.

Furthermore, the seedling dispersal of the *Avicennia marina* and *Avicennia alba* differs. *Avicennia alba* seeds generally arrive in clusters which provides safety for establishment. The individually arriving *Avicennia marina* seedlings do not have this safety.

E. XBeach sand-mud module tests

Since the sand-mud module that was implemented by Bendoni (2015) into the original XBeach suite, has not been used after Bendoni's research, some tests were done to identify the abilities of this model regarding sediment mixing (mud and sand) and to observe the effect of the critical mud fraction on erosion rates.

E.1 Zebra model

The sand-mud module is based on identifying one mud and one sand fraction. The distribution of this fractions along a profile can be set by the user. In order to observe the mixing processes that occur between the two sediment fractions, a 'zebra-model' was made (see Figure E.1). The (transect) profile contains two mild slopes (1:500 - 1:1000) and consists of four separate sedimentation fractions; two mud fractions and two sand fractions. To clarify further, a mud fraction consists for 100% of mud. The same holds for the sand fractions.

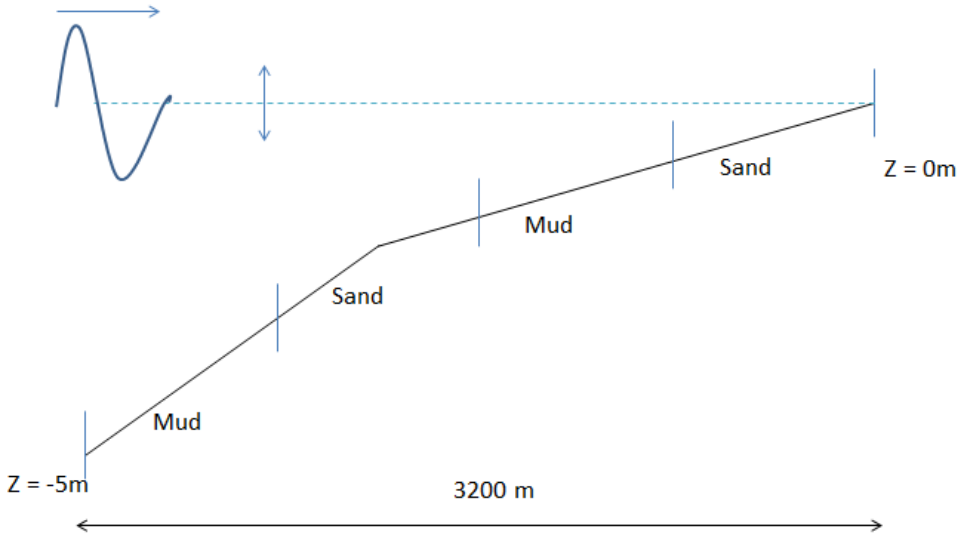

Figure E.1: Schematization of a zebra model

For each test run that was executed, the same hydrodynamic boundary conditions were applied. These conditions are in the order of magnitude of the hydrodynamic conditions that were found in the winter data set from Demak. The tidal signal from the Semarang station for the period 19 November - 8 December 2017 was used which has a tidal range that varies between 60-80cm. The total run time of the simulation is thus 17 days. Furthermore, $H_{m0} = 0.5$m and $T_p = 5$s. The waves approach the shore perpendicularly and Neumann boundary conditions were applied to the lateral boundaries. The bed consists of three 0.5m thick layers (top layer, breathing layer and bottom layer) along the whole profile. The grain sizes for mud and sand are 0.02mm and 0.2mm, respectively.

The main goals of this test were to analyse the mixing of both sediment fractions and to observe the deposition- and erosion rates and correlate these to the observed bed shear stresses. Furthermore, the development of the bed profile will be presented.

Sediment mixing
Figures E.2 and E.3 present the development of the suspended concentration of mud and sand in time. These results show that the concentrations of both fractions are already near their maximum after four hours and the mixing between the sediment fractions is practically zero. When time evolves the mud particles tend to mix along the whole profile whereas the sand particles stick to their initially defined sections. This is mainly due to the higher settling velocities of sand. These plots show that the mixing

process works. The final distribution of the suspended concentrations is presented in Figure E.4

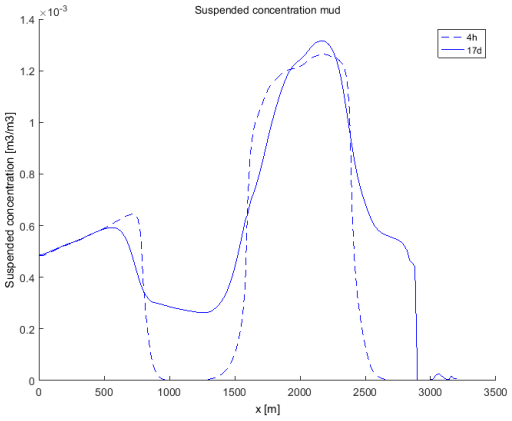

Figure E.2: Suspended concentration development mud

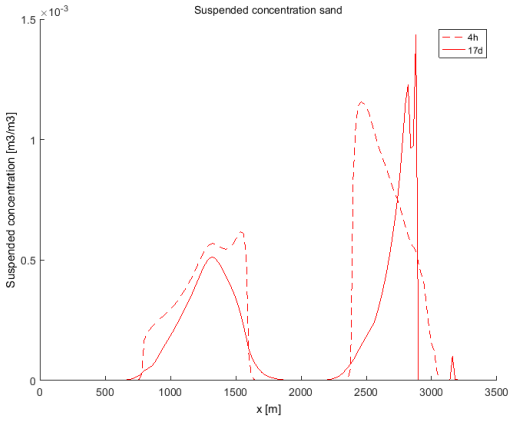

Figure E.3: Suspended concentration development sand

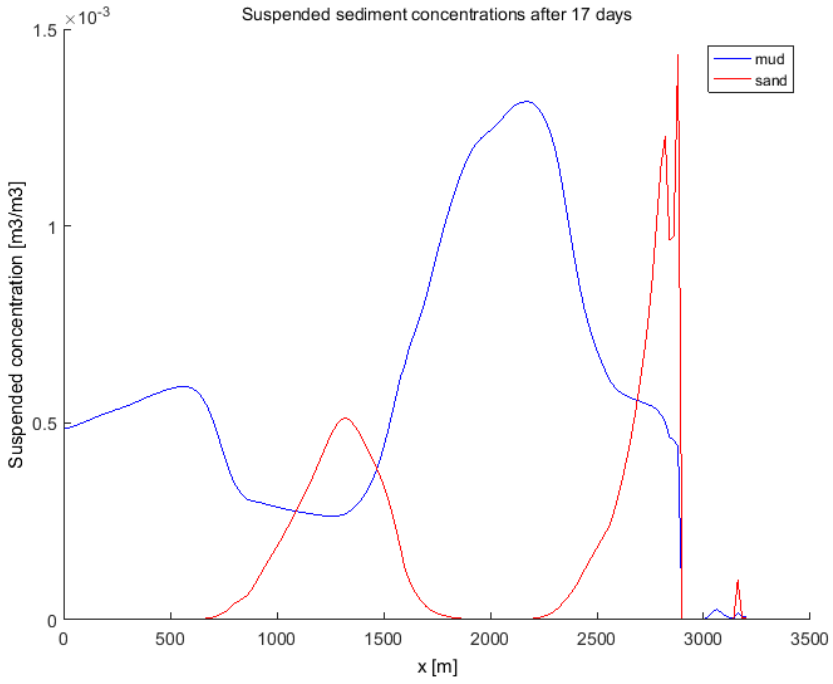

Figure E.4: Final distribution of suspended sediment concentrations along the profile

Deposition and erosion rates
As described in Section A.4, the relations that the model uses to calculate erosion rates depends on the critical mud fraction ($p_{m,cr} = 0.3$). If this threshold is exceeded, the behaviour is according to a cohesive sediment regime. This only holds for erosion rates. The deposition rates are always calculated independently.

For non-cohesive sediments, the deposition rate is proportional to the suspended concentration whereas for cohesive sediments, the deposition rate is proportional to the concentration squared. Figure E.5 shows that the deposition rates follow the same trend as the concentrations as was expected. Looking at suspended mud concentrations in both mud sections in the profile (Figure E.4), an increase of a factor 2.2 can be observed. The deposition rates increase with approximately factor 4.6. For sand, the increase of suspended concentration and deposition rate is equally proportional.

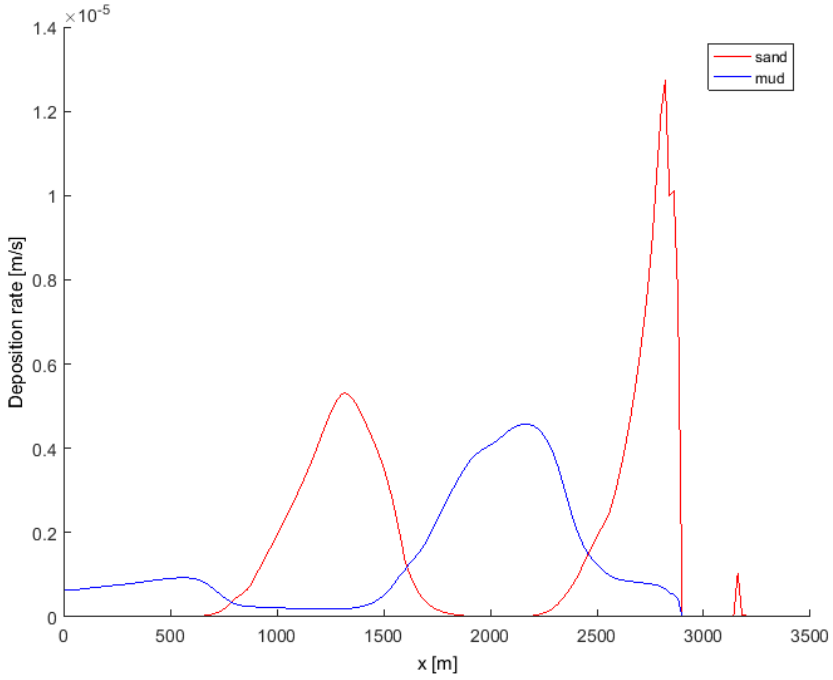

Figure E.5: Final deposition rates along the profile

From the erosion rates in Figures E.6 and E.7, the trend from the suspended concentrations can be found again. The erosion rates indicate areas where a certain sediment has deposited earlier and is thus also an indication of the spreading of sediment along the transect. This spreading is especially visible for the mud fraction, as expected according to earlier findings.

It stands out that the erosion rates for sand are larger than for mud, which is not according to logical expectations due to the higher critical shear stress for erosion for sand.

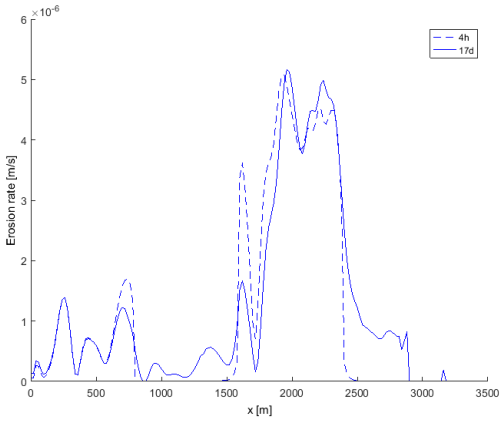

Figure E.6: Erosion rate development of mud along the profile

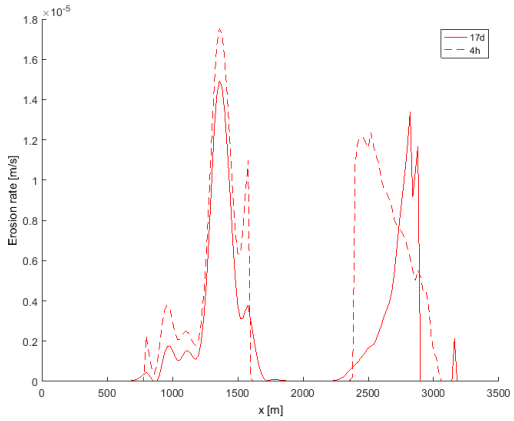

Figure E.7: Erosion rate development of sand along the profile

Bed shear stress vs erosion rate

The erosion rates that are observed should coincide with the bed shear stresses that are present along the profile. Since sediment is already eroded at the most offshore areas of the profile, the bed shear stresses should exceed the threshold shear stresses for erosion at these areas already ($\tau_m = 0.1$ and $\tau_s = 0.5$). However, looking at Figure E.8 this is not the case. This raises the question why sediment is brought into suspension at these early stages and at these areas. An explanation could be that the model has a

certain spin-up time due to which large shear stresses occur initially. However, this was not observed. Figures E.8 and E.9 show that the erosion rates increase in time according to the development of the bed shear stresses. The threshold for mud erosion is not reached within the first 2000m. Other processes should be held accountable for the fact that erosion still occurs.

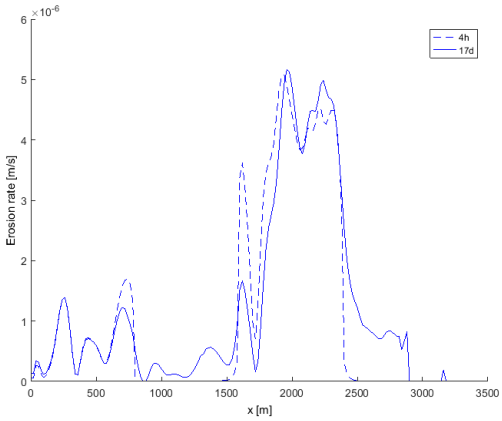

Figure E.8: Development of the bed shear stress along the profile in the first 15 minutes

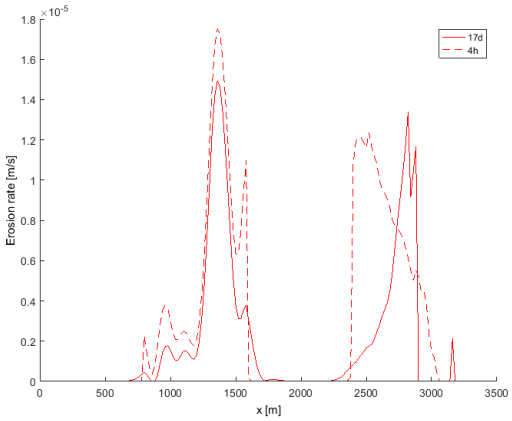

Figure E.9: Development of the erosion rate of mud along the profile in the first 15 minutes

Bed level change

In Figure E.10, the bed level change along the profile is presented. The changes are most prominent at the transition stages between the mud and sand sections. These changes can be extracted from the erosion rates that were presented earlier. The holes and bumps that occur at the transition areas can be related to the significant difference in critical shear stresses for erosion.

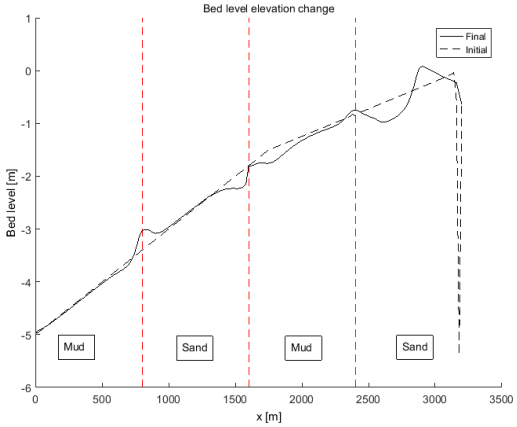

Figure E.10: Development of the bed level elevation of the profile

Due to the significant difference in critical shear stress for erosion, these holes and bulps occur.

F. XBeach sensitivity analysis

A sensitivity analysis was conducted to gain knowledge about the input parameters for the XBeach model that are sensitive and thus useful for calibration matters. The analysis is based on the wave data that was observed in the *eroding transect* during the winter measurements (see Section 5.2.2). From the data, a severe energy dissipation was observed between WL 43 and E2. During the sensitivity analysis, parameters that influence wave dissipation processes were adapted in order to approach the dissipation rates that were observed in the data. Because of a lack of information about, for instance, bathymetry, currents and wind, this analysis was also useful to find out which physical processes might be present in the area that affect the behaviour of the waves. Focus lies on the *short* waves.

In XBeach, three types of short wave dissipation processes are included: bottom friction (D_f), wave breaking (D_w) and vegetation (D_v) (Deltares, 2015). An additional factor is discussed here: bathymetry. Due to highly inaccurate bathymetry information, the possibility remains that variations in bathymetry are unaccounted for. Therefore, also the bathymetry was adapted to visualise the effect on wave propagation.

All the equations that are presented in this appendix are referenced to the XBeach manual (Deltares, 2015) in which additional background information can be found.

F.1 Bottom friction

The short wave dissipation by bottom friction is modelled as Equation G.4.

In this equation, f_w is the only logical calibration parameter. In principle, f_w is calculated by means of Equation A.13. According to that relation, the bottom roughness (z_0) determines the wave friction factor and should therefore adapted to influence the wave friction factor. However, in XBeach the wave friction coefficient is a standalone input parameter. Therefore, changing z_0 does not influence the wave dissipation.

In order to model the effect of the wave friction coefficient, a long, idealised transect was used that reaches from a depth of -12m towards the shore. The transect is idealised to represent a mangrove coast transect. The tidal flat reaches to around 2km offshore with a slope of 1:1000. Then the slope increases to 1:500. A long profile was selected to see when the bottom starts to affect the waves. Details of the runs that were carried out are presented in Table F.1

Table F.1: Runs for the sensitivity analysis of f_w

Run #	H_{m0} [m]	T_p [s]	f_w
1	1.2	6.5	0 (default)
2	1.2	6.5	0.01
3	1.2	6.5	0.02
4	1.2	6.5	0.05

The results of the runs are presented in Figure F.1. The figure shows the values of H_{rms} along the transect distance, x. It can be observed that convergence of the wave heights for the various f_w values starts at a water depth of about 7m. This moment varies with the wave period but is nevertheless important to analyse since it could determine the maximum distance from the shore at which the boundary conditions must be set. The moment at which waves start to feel the bottom does not change for different f_w values.

The wave height correlated to the various wave friction coefficients show clearly that this parameter has a large effect on the wave development. Comparing the wave heights between $fw = 0$ and $fw = 0.05$, the maximum difference is over 20cm. This is a difference of approximately 25%.

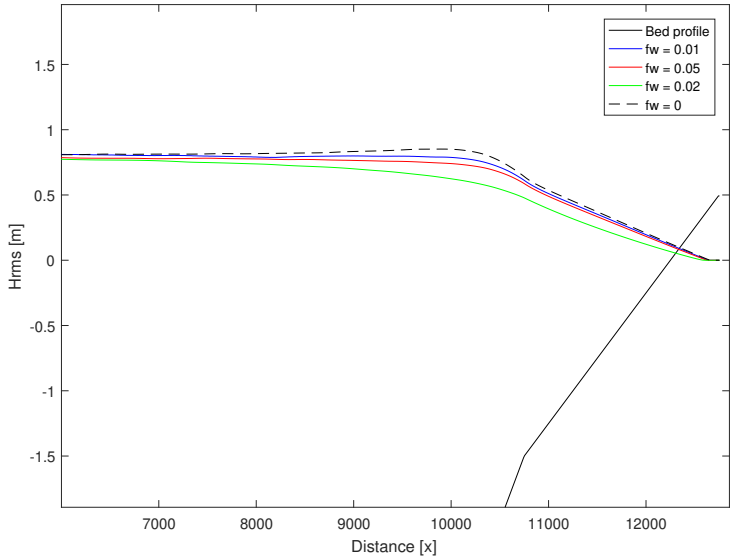

Figure F.1: Results of the sensitivity analysis of f_w on H_{rms}

Changing the wave friction coefficient thus decreases the wave height, according to Equation G.4. It must be noted that bottom friction constantly takes place from the moment that the waves are affected by the bottom. This parameter can not be adapted locally.

F.2 Bathymetry

As mentioned earlier, the sensitivity analysis is used to find out which parameters are helpful in order to obtain the dissipation rates as observed in the data. Regarding wave breaking, the focus lies on the section between E1 and E2 in the eroding transect. The dissipation in this section is much higher than in the other sections, indicating additional dissipation processes such as wave breaking. This is especially the case for incoming waves larger than 40cm (see Section 4.2.3). With the bathymetry as measured in the field, a linear slope has to be assumed along 230m between E1 and 44. Model results have shown that on such a mild slope, no wave breaking occurs, but only surface rollers.

Focus lies on a wave event on November 27^{th}. A wave height of $H_{rms} = 0.55$m was measured at E1 while as E2 the wave height had decreased to $H_{rms} = 0.20$m. From Figure 4.3 it can be observed that the data measurements are best approached when a chenier initiates wave breaking in the particular section. In that case the wave heights are $H_{rms} = 0.52$m at E1 and $H_{rms} = 0.21$m at E2. With a detailed bathymetry available, this is not a valid calibration method. However, no bathymetry points have been measured along the whole section between E1 and E2.

Another possible bathymetry profile is presented hereafter. Since the sensitivity analysis showed that a wave friction coefficient of 0.05 is applicable in the eroding transect, this might be combined with a less shallow obstacle, earlier in the section between E1 and E2, as can be observed in Figure F.2. This combination approaches the data results also quite accurately. Certainly because the wave friction factor might increase locally, between E1 and E2 due to the larger grain sizes at these locations. However, in order to achieve the same wave heights at both E1 and E2, this option still does not deliver a high enough dissipation rate.

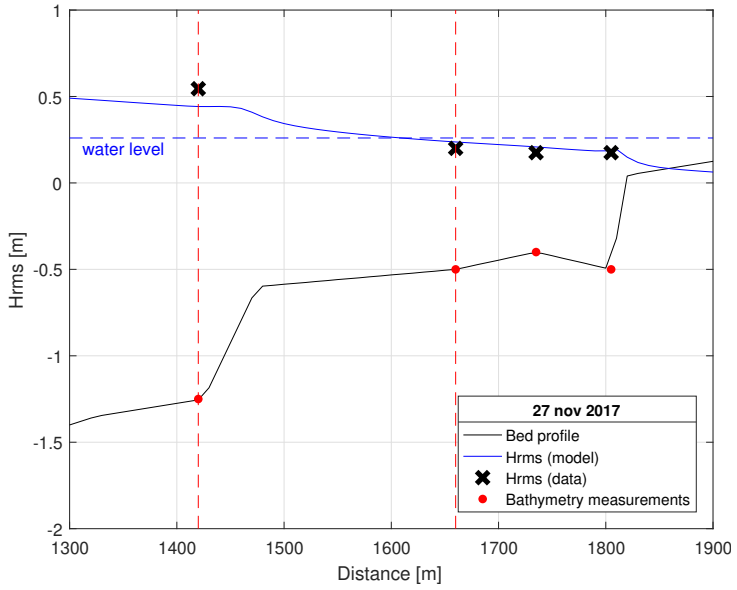

Figure F.2: Sensitivity analysis with a sill between E1 (left red-dotted line and E2 (right red-dotted line).

F.3 Wave breaking

If wave breaking occurs, the amount of dissipation during this process can be adapted. This section focuses on the energy dissipation due to short wave breaking.

The energy dissipation by short wave breaking is calculated according to Roelvink (1993). In this formulation, the dissipation of total wave energy (D_w) is calculated by multiplying the dissipation with a fraction of breaking waves (Q_b) with the total dissipation per breaking event. This relation is given by Equation F.1:

$$D_w = 2\frac{\alpha}{T_{rep}} Q_b E_w \tag{F.1a}$$

$$Q_b = 1 - \exp\left(-\left(\frac{H_{rms}}{H_{max}}\right)^n\right), \quad H_{rms} = \sqrt{\frac{8E_w}{\rho g}}, \quad H_{max} = \gamma(h + \delta H_{rms}) \tag{F.1b}$$

where T_{rep} is the representative wave period. The wave dissipation coefficient, α, counts as an important calibration parameter in this equation and is therefore tested on its sensitivity. Also, γ is important which determines at which wave height to depth ratio waves start to break. The wave model is however calibrated on the default settings for $\gamma = 0.55$ and therefore this value might not be adapted much.

The runs for the sensitivity analysis of α are presented in Table F.2. The values of H_{m0} and T_p are adapted to the peak wave event on November 27^{th}, 2017.

Table F.2: Runs for the sensitivity analysis of α

Run #	H_{m0} [m]	T_p [s]	α
1	1.14	6.1	1.0 (default)
2	1.14	6.1	1.5
3	1.14	6.1	2.5
4	1.14	6.1	10.0

From Figure F.3 it can be observed that the average wave heights decrease for higher alpha values, meaning that overall a larger wave dissipation has occurred. However, looking at the section between

the red-dot lines, it can also be observed that the dissipation *rate* does not increase. The parameter α is thus not sensitive for increasing the wave dissipation on such a short section and is thus not useful for calibration in this case.

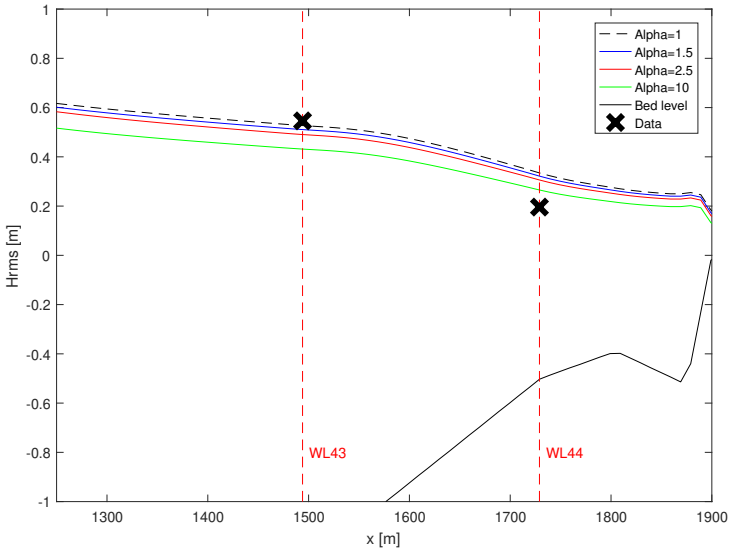

Figure F.3: Results of the sensitivity analysis of α on H_{rms}

G. Additional literature

This chapter contains additional literature on coastal hydrodynamic processes in order to support the literature review of Section 2.1.

G.1 Tide

In this section, basic definitions about tidal waves are explained based on Bosboom and Stive (2015).

G.1.1 Definitions

The daily water level variations that can be observed from the coast are caused by the presence of *tides*. Tides are the result of gravitational pull that is exerted on the earth by the sun and the moon. Due to this force, tidal waves are propagating along the globe with a wave length of several hundreds of kilometres. Tidal waves initiate the occurrence of high and low waters which are called *flood* and *ebb*, respectively. The period from high water to low water is called the *falling period* whereas the period from low water to high water is the *rising period*. This vertical movement is called the vertical tide. The horizontal tide refers to the horizontal movement that is related with the vertical tide and is represented by tidal currents. The direction of the tidal currents depends on the propagation direction of the tide so that distinction is made between *ebb currents* and *flood currents*. The moment where the direction of tidal flow reverses is called *slack water*.

The amplitude of the tidal wave determines the *tidal range* that is observed and depends on the positions of the sun and moon with respect to the earth. When sun, moon and earth are positioned in one straight line, the gravitational pull is maximum and *spring tide* occurs. When the sun and moon are 90 degrees out of phase, their forces weaken each other resulting in a smaller amplitude indicating *neap tide*.

G.1.2 Tidal character

Under the assumption that the sun and moon exert forces directly on the earth's equator, two high and low waters per day of equal height should occur on a certain place on earth. However, the declination angle of the earth introduces irregularities in the earth's movement. These irregularities, together with influences of the sun and moon are described by the tidal constituents. The principal tidal constituents M2 and S2 represent the lunar and solar tide, respectively and occur both twice a day. Due to the earth's declination, other tidal constituents are introduced and represent the daily inequality. The tidal constituents together determine the tidal character of a certain area on the world. Distinction is made between semi-diurnal and diurnal. A semi diurnal character refers to two high and low waters per day whereas a diurnal character experiences only one high and one low water each day. When an area experiences fractions of both characters, this is announced by the term *mixed*.

G.1.3 Tidal asymmetry

The tidal signal shows the water surface elevation around Mean Sea Level (MSL) in time. In an ideal situation, the tidal signal is symmetrical, meaning that high water is just as much above MSL as low water is below MSL and the falling period equals the rising period. However, a tidal signal is always asymmetrical which is referred to as *tidal asymmetry*. When the rising period is shorter than the falling period, the tidal signal is *flood-dominant*. Conversely, a shorter falling period is associated with *ebb-dominance*. A shorter falling or rising period comes with higher tidal currents. Since tidal asymmetry determines the strength of tidal currents and the slack duration of the tide, it has a strong influence on the coastal morphology.

G.2 Waves

This section elaborates on literature regarding wave breaking, wave dissipation due to bottom friction and spectral wave analyses.

G.2.1 Wave breaking criteria

In this section, criteria for wave breaking on mild slopes are described. These criteria are used in order to assess the probability of wave breaking in the analysed transects.

The effect of the bed slope on the wave breaking process is described by the Irribarren parameter and is defined as follows:

$$\zeta = \frac{\tan(\alpha)}{\sqrt{H_0/L_0}} \tag{G.1}$$

in which tanα defines the steepness of the beach and L_0 is the wave length in deep water.

The effect of the value of ζ is visualised in Figure G.1. For ζ values below 0.5, the wave breaking process is of a spilling type. This breaking process is representative for mud flats.

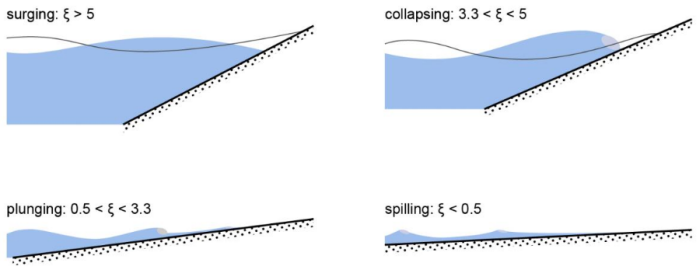

Figure G.1: Breaker types for various Irribarren numbers.

The moment when waves are breaking is determined by the physical limit of the steepness of waves. For this, the breaking criterion that was expressed by Miche (1944) is applied. The limiting wave steepness is based on Stokes wave theory and is described by the following relation:

$$\left[\frac{H}{L}\right]_{max} = 0.142\tanh(kh) \tag{G.2}$$

In shallow water this relation reduces to $\gamma = H/h \approx 0.88$. For solitary wave theory, a non-linear theory which is valid in shallow water, $\gamma \approx 0.78$. Experimental results have suggested that for spilling breakers, waves break earlier and γ lies between 0.6-0.8 (Bosboom and Stive, 2015).

G.2.2 Calculation wave friction factor

An important parameter that influences the short wave dissipation due to bottom friction is the wave friction coefficient, f_w (see Section F.1). This coefficient is used to determine the wave friction due to bottom friction along the transects. By comparing the resulting values to the literature, it can be determined whether bottom friction is the most important dissipation factor, or that other processes such as wave breaking play apart.

The wave friction coefficient is calculated by by analysing the wave energy dissipation along different sections along the transect. These sections are defined as the section between subsequent measuring instruments. The wave dissipation is calculated as follows:

$$D_f = -\frac{dP}{dx} = -\frac{d(c_g \cdot E)}{dx} \tag{G.3a}$$

$$E = \frac{1}{8}\rho g H_{rms}^2 \tag{G.3b}$$

in which P is the energy flux per unit wave crest width, c_g is the wave group velocity and dx is the length of a section. The wave friction factor is then calculated similarly as in XBeach (Deltares, 2015):

$$D_f = \frac{2}{3\pi}\rho f_w \left(\frac{\pi H_{rms}}{T_{m01}\sinh kh}\right)^3 \tag{G.4}$$

where f_w is the short wave friction coefficient and T_{m01} is the mean period defined by the first and zeroth moments of the wave spectrum. For this calculation average values along the corresponding section are used for H_{rms}, T_{m01} and kh.

The local wave friction coefficient can be calculated by means of means of Equations G.5 (Jonsson, 1966). This calculation depends on a roughness parameter which can be estimated based on the sediment composition.

$$f_w = \exp\left[-5.977 + 5.213\left(\frac{\hat{\zeta_0}}{r}\right)^{-0.194}\right] \tag{G.5a}$$

$$\hat{\zeta_0} = \frac{\hat{u_0}}{\omega} \tag{G.5b}$$

$$\hat{u_0} = \frac{\omega a}{\sinh(kh)} \tag{G.5c}$$

G.2.3 Spectral wave analysis

In order to analyse wave information, records of water surface elevations are gathered offshore (see the right side of Figure G.2). The short term variations in surface elevations are then statistically described by determining average wave parameters over such a short period. The length of this interval has to be short enough to be statistically stationary and long enough to get reliable averages. In this research, the short term statistics are determined by means of a spectral analysis.

With a spectral analysis, the variations in the water surface are the result of a summation of an infinite number of sine waves with a variety of heights, periods and directions (Bosboom and Stive, 2015). The various sine waves all come with different frequencies. Lower frequencies are represented by relatively large and long waves which contain more energy than small, short waves that are represented by the higher frequencies. The amplitudes and periods of the sine waves are determined by a Fourier analysis which states that in a stationary wave record the sine waves all have a constant amplitude and phase per component in time.

From the amplitudes of all the harmonic components, the variance density spectrum can be obtained. Since the variance is coupled to the energy by a factor ρg, this spectrum is used to analyse the wave energy. An energy spectrum is presented on the left side of Figure G.2. The variance density spectrum describes the variance density per frequency in the wave record. By analysing the width of the spectrum, one can determine the regularity of the wave field and the energy distribution over the various frequencies.

The area under the spectrum is the zeroth order spectral moment (m_0). This is equal to the total variance integrated over all frequencies (Bosboom and Stive, 2015). When interest lies in analysing particular frequencies (representing shorter or longer waves), other moments can be calculated which focus on lower frequencies (m_{-1}) or higher frequencies (m_1,m_2..). By comparing the wave spectra of different locations in, for instance, a transect from offshore towards the coast, information can be obtained about the wave transformation which is particularly interesting for this research.

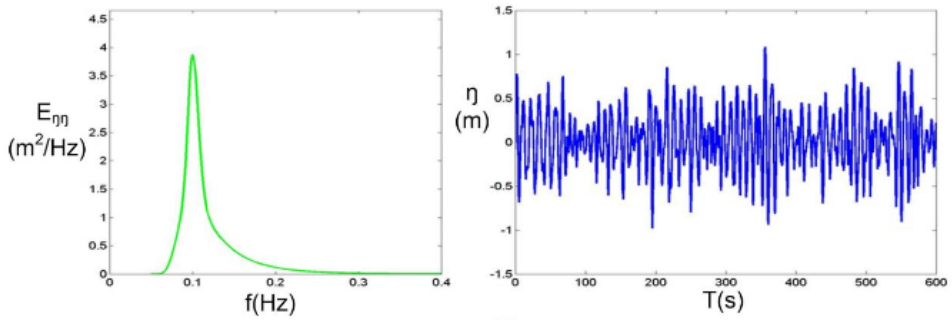

Figure G.2: A wave spectrum (left) with the corresponding surface elevation time series (right) (Bosboom and Stive, 2015)

Based on m_0, the spectral significant wave height is obtained by means of $H_{m0} = 4\sqrt{m0}$. Similarly, the peak wave period can be determined from the spectral moments as well: $T_p = \sqrt{m_0/m_2}/0.7$.

It is important to note that average wave parameters can also be determined by means of a wave-by-wave analysis. H_{rms} is often used when it comes to calculations regarding the energy content of irregular wave fields. H_{m0} and H_{rms} are related by means of $H_{rms} = 0.7H_{m0}$.